Numerical Investigation of the Unsteady Aerodynamics of '*Passer Domesticus*'Inspired Biomimetic Wing

A Thesis Submitted in Partial Fulfillment of the Requirements for the Degree of

DOCTOR OF PHILOSOPHY

by

Masuruddin Shaik

(166103007)

DEPARTMENT OF MECHANICAL ENGINEERING

INDIAN INSTITUTE OF TECHNOLOGY GUWAHATI

GUWAHATI-781039, INDIA

OCTOBER, 2022

भारतीय प्रौद्योगिकी संस्थान गुवाहाटी
Indian Institute of Technology Guwahati

Numerical Investigation of the Unsteady Aerodynamics of '*Passer Domesticus*'Inspired Biomimetic Wing

A Thesis Submitted in Partial Fulfillment of the Requirements for the Degree of

DOCTOR OF PHILOSOPHY

by

Masruddin Shaik

(166103007)

Under the Supervision of

Prof. Shyamanta Moni Hazarika

DEPARTMENT OF MECHANICAL ENGINEERING

INDIAN INSTITUTE OF TECHNOLOGY GUWAHATI

GUWAHATI-781039, INDIA

OCTOBER, 2022

भारतीय प्रौद्योगिकी संस्थान गुवाहाटी
Indian Institute of Technology Guwahati

DEPARTMENT OF MECHANICAL ENGINEERING
INDIAN INSTITUTE OF TECHNOLOGY GUWAHATI
GUWAHATI-781039

CERTIFICATE

This is to certify that the work contained in the thesis entitled "**Numerical Investigation of the Unsteady Aerodynamics of '*Passer Domesticus*'Inspired Biomimetic Wing**", by *Masuruddin Shaik* (166103007), in the Department of Mechanical Engineering, Indian Institute of Technology Guwahati, India, for the award of degree of Doctor of Philosophy has been carried out under our supervision and this work has not been submitted elsewhere for the award of any other degree or diploma.

Prof. Shyamanta Moni Hazarika
Professor
Department of Mechanical Engineering
Indian Institute of Technology Guwahati
Guwahati, Assam-781039

भारतीय प्रौद्योगिकी संस्थान गुवाहाटी
Indian Institute of Technology Guwahati

Dedicated to

My beloved parents

भारतीय प्रौद्योगिकी संस्थान गुवाहाटी
Indian Institute of Technology Guwahati

ABSTRACT

The flapping flight, which is governed by the unsteady aerodynamics, deals with inherent complexities especially at low Reynolds number (Re). Understanding the flow physics behind these intricacies may lead to a great chance of enhancing the aerodynamic performance of Flapping Wing Micro Air Vehicles (FW-MAVs). Nature provides a variety of small flying birds and insects to achieve this goal via biomimicry. However, direct copying of concepts available in nature may not lead to feasible solutions. The balance between engineering implementation and exploitation of concepts from nature may lead to successful designs. The work presented in this dissertation attempts at bringing this vision a little closer to realization.

In the first part of the work, a biomimetic wing is modelled by considering the Passer Domesticus wing as a reference. Initial investigations are carried out to analyse the aerodynamic characteristics of the biomimetic wing and its performance is compared with commercially available rectangular and elliptical wing planforms under fixed condition. From the present findings, it is observed that the elliptical planform offers less drag than that of other wing planforms. This indicates that the elliptical wing planform might be suitable for studies where the drag reduction is primary objective. It is also observed that the presence of the sharp edges in the rectangular wing planform encourages the flow separation and affects the overall aerodynamic performance of the wing. In the case of biomimetic wing, the change in wing profile allows to have a variable angle of attack along the span which delays the flow separation and improves the wing's aerodynamic performance. Due to this, a 57.9% increase in lift coefficient is observed for the biomimetic wing than that of elliptical wing. A 22.4% increase in lift to drag ratio of the biomimetic wing is observed than that of rectangular wing under same conditions. In the next part of the work, the kinematics of flapping flight of birds are discretised into three different motions, namely: pitching, plunging and flapping motion (combination of rotation about wing chord and span). The unsteady flow characteristics of the biomimetic wing subjected to these motions are numerically analysed.

When the wing is subjected to the pitching motion, it is observed that, the unsteady vortex shedding over the pressure side of the wing creates the negative suction at lower pitch amplitudes. This opposes the positive suction created over the suction side and affects the wing's performance. However the adverse effects of the oppositely signed circulation diminish with increase in the frequency due to substantial reduction in the growth of the vortex over the pressure side of the wing. This improves the instantaneous values of lift and thrust force coefficients at higher frequencies in combination with lower pitch amplitudes. At higher mean angles of attack, a substantial diminution in the instantaneous force coefficients is observed due to large flow separation which makes it hard for the separated flow to reattach. From the flow investigations, it is also observed that the shifting of pitching axis away from the leading edge encourages the retardation of vortex coherence which has adverse impact on the thrust force generation of the wing.

The observations from the flow field investigations reveal a superior convection of the leading edge vortex along the axial core at smaller plunge amplitudes when the wing is subjected to the plunging motion. The presence of local peaks in the amplitude spectrum of instantaneous force coefficients confirms that there exist an adverse interaction between leading and trailing edge vortices at higher plunge amplitudes. With increase in the frequency, a more prominent vortex formation is observed near the leading edge and also closer to the wing's surface. As the cycle continues, this vortex roll-up and interacts with the trailing edge vortex which was formed closer to the wing's trailing edge. These vortices shed in the wake in the form of the alternating vortices. From the flow investigations, it is observed that the additional advantage of increasing the frequency is that, it remarkably increases the strength of these vortices which eventually roll-up over the suction side of the wing. Due to this, the instantaneous force coefficients of the wing rises towards higher values at higher frequencies.

The investigations are further carried out to analyse the unsteady flow characteristics of the biomimetic wing subjected to flapping motion. Asymmetric variation of instan-

taneous force coefficients despite of having symmetrical flapping kinematics reveals that the optimal aerodynamic performance of the biomimetic wing demands proper selection of operating conditions. It is observed that, at lower flapping amplitudes, the formation of Leading edge vortex (LEV) over the suction side happens farther away from the surface and roll up away from the wing at the beginning of the flapping cycle. As the cycle continues, this LEV convects farther downstream and affects the suction created due to the positive vortex circulation. Increasing the flapping amplitude increases the wing's influence over its surrounding fluid and vortex formation happens closer to the wing's surface. This enhances the positive suction and remarkably influences the thrust force generation of wing. The observations from the flow field Investigations reveals that the formation and the convection of the LEV not only influences the drag-thrust transition but also the wake pattern. The increase in the mean angle of attack has a significant impact on the wake pattern. Different types of transitional forms of wake are observed at different mean angles of attack due to shedding of multiple votices per cycle. Especially at 16^0, the alternating vortices exhibit irregular patterns in the wake region and form clusters due to adverse interference between the vortices shed between the previous cycle and next cycle. This impinges the wing's performance with increase in the mean angle of attack. From the flow investigations, it is also noticed that, increasing the flapping frequency not only increases the vortex strength but also ensures that the flow is attached during major portion of the flapping cycle.

In overall, it is observed that the proposed form of the biomimetic wing has shown a remarkable aerodynamic performance when subjected to different unsteady conditions at low Re. We hope the findings reported in this dissertation might be helpful in practical wing design applications.

ACKNOWLEDGEMENT

I wish to express my sincere gratitude to a number of people who have supported me in a variety of ways throughout the course of this thesis.

First and Foremost, I would like to sincerely thank Prof. Shyamanta Moni Hazarika for his invaluable guidance. I am deeply obliged to him for giving me the freedom to work in the field of aerodynamics that I wanted. His critical comments and suggestions have been instrumental in completing this dissertation and I am extremely gratified with his endeavor in molding me into a disciplined research student. I would love to cherish my whole life in the memory of his association with me as a student.

I would like to extend my sincere gratitude to my first supervisor Late Dr. Annem Narayana Reddy who left us in such a young age. He meant a lot more than a supervisor to me. Always helping out with everything he could and very supportive. I have very fond memories of him. His lucid teaching skills and knowledge always inspire me. The work reported in this dissertation have its origin from numerous discussion and guidance he extended.

Special thanks to all my doctoral committee members: Prof. Vinayak Narayan Kulkarni, Prof. Atanu Banerjee, Prof. Arbind Kumar Singh for their continuous guidance and suggestion during my research work. They are equally responsible to build confidence inside me by their constructive comments and advice.

I would like to extend my sincere thanks to past and present departmental heads Prof. Santosha. K. Dwivedy and Prof. K. S. R. Krishna Murthy for their kind permission for enrolment, lab facilities and fellowship support in the department of mechanical engineering, IIT Guwahati.

I have been blessed with very good seniors and friends in my lab. I would never forget the contribution of Kamal, Sibananda, Mirzaul Karim and Firdausa to the completion of this research work. They are like my elder brothers and sister who taught me to use various research-related tools. I am fortunate to be a friend of Rasool, Dhanunjay, Ajay and Shailendra. I can write endlessly about the days we all have spent together on the campus but some things are better left unsaid. It's my pleasure to acknowledge help provided by my juniors, Pritesh, Anand, Gopi, Kanak, Santhosh, Shahrukh and Bipul and really had very good memories. In this campus, luckily I have surrounded by some very good friends, Abhijit, Subhash, Hirak, Nilav, Supriya, Prarthana and Montoo da.

In this precious moment of my life, I would like to express my deep sense of gratitude to my parents, Ammi and Abbu for their love, blessings and constant encouragement throughout my life. Without their support, it would be impossible to complete my PhD journey. I would like to thank my brothers for their love, support and best wishes. I am blessed to have them. I am deeply in debt to my family for the sacrifices they have borne to ensure the fulfilment of my dreams. You have always been inspiring, supporting and teaching me to understand the true value of human life

Lastly, I thank Almighty for blessing me with precious life.

Masuruddin Shaik
IIT Guwahati
October, 2022

भारतीय प्रौद्योगिकी संस्थान गुवाहाटी
Indian Institute of Technology Guwahati

Contents

भारतीय प्रौद्योगिकी संस्थान गुवाहाटी
Indian Institute of Technology Guwahati

List of Figures

List of Tables

Nomenclature

θ_m	mean angle of attack (^{0})
α_f	flapping amplitude (^{0})
k_f	non-dimensional flapping frequency or reduced frequency
ρ	density of incoming fluid (kg/m^3)
h_a	non-dimensional plunge amplitude
Re	Reynolds number
C	wing chord length (m)
μ	dynamic viscosity of incoming fluid (kg/m-s)
ν	dynamic viscosity of incoming fluid (m^2/s)
f	frequency of oscillation
St	Strouhal number
U_∞	velocity of the incoming fluid (m/s)
ω_z	Z-vorticity (1/s)
ω_s	Spanwise vorticity (ω_zC/U_∞)
$k_f h_a$	non-dimensional plunge velocity
α_p	pitching amplitude (^{0})
ϕ_d	phase difference (^{0})
C_l	instantaneous lift coefficient
C_d	instantaneous drag coefficient
C_{pc}	mean power coefficient
C_t	mean thrust coefficient
C_t^*	instantaneous thrust coefficient
C_p	mean pressure coefficient
η_p	mean propulsion efficiency
η_p^*	instantaneous propulsion efficiency
t^*	time step (s)

भारतीय प्रौद्योगिकी संस्थान गुवाहाटी
Indian Institute of Technology Guwahati

Chapter 1

Introduction

1.1 Overview

Flying birds caught the attention of researchers from many centuries. Leonardo da Vinci, a great researcher in many areas had a vision of people flying through the sky like birds. With time, the research on flying took several turns; resulted in new inventions like parachutes, Unmanned Aerial Vehicles (UAVs). Further, the extensive research in the aviation field had shown a great deal of interest in the design of small uninhabited and highly manoeuvrable aerial vehicles particularly in applications such as: surveillance, search rescue operations and reconnaissance. One such category of these aerial vehicles is Micro Air Vehicle (MAV). The MAV is a class of unmanned aerial vehicle having overall dimensions less than 6 inch [8]. Usually MAVs fly in the low Reynolds number (Re) regime ($2 \times 10^4 \leq Re \leq 2 \times 10^5$) where the inertial forces are dominated by the viscous forces [1]. In addition to that, one of the major challenges of MAV design is wing design, where the wings have low aspect ratio (LAR) with LAR ≤ 2. The flow around the wing at low Re is mostly viscous in nature and associated with non-linear vortex shedding which further increase these complications [9, 10]. This motivates us to model a biomimetic wing inspired from the wing planform of natural flyer and investigate its unsteady flow characteristics subjected to different unsteady conditions at low Re.

1.2 Objectives

In the light of an extensive literature survey, the broad aim of the present work has been divided into the following objectives:

1. **Study of biomimetic wing**

   In the present work, a biomimetic wing is modelled and its aerodynamic perfor-

mance is analysed. The modelling of the biomimetic wing is done by considering the wing planform of natural flyer (Passer Domesticus) as a reference. The cross sectional shape of the biomimetic wing is modelled by introducing a thin and highly cambered airfoil at different sections of the wing planform. Preliminary investigations are carried out to explore the aerodynamic characteristics of the biomimetic wing at fixed condition. The current objective is sub-divided as follows:

(a) Wing modelling

(b) Analysis of the aerodynamic performance of biomimetic wing

2. **Performance comparison of biomimetic wing with conventional wings**
The conventionally opted rectangular and elliptical wing planforms are modelled with similar cross section and dimensions as that of the biomimetic wing for comparison. Both numerical and experimental studies are carried out to investigate and compare the aerodynamic performance of all three wing planforms at fixed condition. Towards this end, an extensive parametric study is conducted to unveil the reasons behind the better aerodynamic characteristics of biomimetic wing compared to that of other wings. The current objective is sub-divided as follows:

   (a) Comparison via numerical simulation method

   (b) Comparison via experimental method

3. **Numerical investigation of the biomimetic wing's aerodynamic performance subjected to different unsteady conditions at low *Re***
Thorough numerical investigations are carried out to analyse the propulsive performance of the biomimetic wing subjected to different unsteady conditions. These unsteady conditions are kinematically discretized from the flapping flight of actual birds. The flow around the wing is also analysed to provide a conceptual overview of how the kinematics affect the wing's performance. The unsteady conditions considered for the present study are as follows:

   (a) Pitching motion

   (b) Plunging motion

   (c) Flapping motion

1.3 Thesis contribution

In this thesis, numerical study is carried out on the Passer Domesticus inspired biomimetic wing at low *Re* regime under different unsteady flow conditions. The contributions of

this research are categorized into two parts:

1.3.1 Modelling of biomimetic wing and performance comparison

A biomimetic wing is modelled by considering a natural flyer (Passer Domesticus) as a reference. To model the wing cross section, Bergey BW-3 airfoil which is a thin and highly cambered airfoil is introduced at different sections of the wing. The aerodynamic characteristics of this biomimetic wing is analysed with respect to different parameters at different conditions. Further, the performance of the biomimetic wing is compared with commercially opted rectangular and elliptical wing planforms. The investigations reveals that the biomimetic wing has shown remarkable aerodynamic characteristics compared to that of other wing planforms. This can encourage the designers to consider the proposed biomimetic wing for innovative wing designs rather than commercially opted wing planforms.

1.3.2 Investigation of the flow characteristics at low *Re*

The numerical work carried out throughout this thesis is accompanied by extensive three dimensional studies. The work aims to contribute towards addressing the unsteady flow characteristics at low *Re* regime by analysing the flow field around the biomimetic wing subjected to different unsteady conditions. These unsteady conditions are obtained by kinematically discretizing the flapping flight of actual birds. This may provide useful insights for practical wing design applications. Through the extensive parametric investigations, the work reported in the thesis contributes towards understanding on how the system parameters can remarkably influence the instantaneous force coefficients and eventually the wing's performance. A conceptual overview of the fluid phenomena is provided to address the valuable insights on three dimensional unsteady flows at low *Re* by exploring the behaviour of high viscous phenomena and its adverse effects on the flow field.

1.4 Thesis organisation

The results of all the investigations are elucidated and summarised in this thesis in the form of chapters. The thesis is divided into eight chapters.

- **Chapter-1: Introduction**
  Chapter-1 describes about the motivation, objectives, contribution and overall out-

line of the thesis.

- **Chapter-2: Literature review**
  Chapter-2 discusses about the physics behind the flow at low Reynolds number (Re). A brief review of the findings reported and existing solution methods to investigate the low Re flows are also presented.

- **Chapter-3: Numerical Simulation Method**
  Chapter-3 presents the governing equations, their numerical formulation and the baseline problem setup employed in this work.

- **Chapter-4: Aerodynamic Investigation of the Stationary Biomimetic Wing Inspired from Passer Domesticus**
  Chapter-4 presents the study of a biomimetic wing which is modelled by considering the wing of a natural flyer (Passer Domesticus) as a reference. To investigate the aerodynamic characteristics of the biomimetic wing, numerical and experimental studies are carried out at low Reynolds number (Re). The performance of the biomimetic wing is compared with rectangular and elliptical wings in terms of instantaneous force coefficients. Further, the flow field around the biomimetic wing is also analysed in order to understand the reasons behind its better performance than that of the other wing planforms.

- **Chapter-5: Low *Re* Flow Investigations of the Biomimetic Wing Undergoing Pitching Motion**
  Chapter-5 deals with the aerodynamic performance of the biomimetic wing undergoing pure pitching motion. The numerical study systematically investigate the influence of pitch amplitude, location of pitching axis and the mean angle of attack on the thrust force generation of the biomimetic wing. Further, the associated flow field is analysed to understand the reasons behind the positive thrust force generation.

- **Chapter-6: Unsteady Flow Characteristics of the Biomimetic Wing Performing Plunging Motion**
  Chapter-6 stages the study of biomimetic wing undergoing pure plunging motion. An extensive numerical study is carried out to investigate the effect of non-dimensional plunge amplitude, reduced frequency and the Reynolds number. The details of the generated vortical patterns and their effects on the flow field are also discussed.

- **Chapter-7: Aerodynamic Investigation of the Biomimetic Wing Subjected to Flapping motion**

  Chapter-7 discusses about the propulsive performance of the biomimetic wing subjected to a flapping motion. The flapping motion in the present study refers to the combination of the rotations about the axis along the wing chord and the wing span with a phase difference of ϕ_f. The influence of the flapping amplitude, mean angle of attack and non-dimensional flapping frequency on the thrust force generation of the biomimetic wing are investigated. The corresponding flow field is also further analysed to systematically understand the reasons behind drag-thrust transition.

- **Chapter-8: Concluding Remarks**

  Chapter-8 draws the major conclusions of the thesis and recommendations for future works.

भारतीय प्रौद्योगिकी संस्थान गुवाहाटी
Indian Institute of Technology Guwahati

Chapter 2

Background and Literature Review

This chapter briefly addresses the physics behind the flow at low Re. A brief review of the findings reported and existing solution methods to investigate the low Re flows are also presented. The literature pertaining to the complex nature of the flow at different unsteady conditions is further addressed in the beginning of each individual chapter.

2.1 Flow physics at low *Re*

The flow field around the wing at low Re is mostly viscous in nature and associated with non-linear vortex shedding. The respective phenomena at low Re regime can be classified as: suction at leading edge, separation at trailing edge, dynamic stall and nature of the wake. These phenomena are briefly addressed in the following sections based on the findings reported in the literature.

2.1.1 Suction at leading edge

For a wing which is fixed at a given angle of attack, the lowest pressure can be noticed wherever the stream line curvature is high, mostly near the leading edge of the wing. This is also valid for a flapping wing where the lift and thrust forces are highly dependent on the amount of suction at the leading edge [11, 12]. Most of the numerical and experimental studies suggest that the vortex shedding due to the flow separation at the leading edge can remarkably influence the aerodynamic performance of the wing [13, 14, 15, 16]. It was also reported that the interaction between the Leading Edge Vortex (LEV) and the wing surface can also influence the wing motion which can be optimised by controlling the flow parameters for better MAV designs [17, 18].

2.1.2 Separation at trailing edge

In general, the sharp trailing edge of the airfoil is a natural point of separation. The analytical and inviscid computational methods are developed by assuming all the vortex shedding into the wake, happens tangential to the trailing edge which is known as Kutta condition. A number of studies were carried out to investigate the application of Kutta condition on the unsteady flows over the sharp trailing edge airfoils.

To investigate the validity of Kutta condition, Katz and Plotkin [19] analytically studied the roll-up of the vorticity of a thin airfoil in the wake region (downstream of the trailing edge). Their findings are compared with the experimental findings reported by Katz and Weihs [20] under same conditions. It was reported that they had observed a very similar shape of wake pattern in both findings which is a result of flow circulation over the airfoil surface. Katz and Plotkin [19] also reported about possible flow separation at higher angles of attack, amplitudes and frequencies near the trailing edge which violates the Kutta condition. However, there was no noticeable effect on the lift and thrust force coefficients of the airfoil. Archibald [21] reported that when $k_f \geq 0.6$, the stream lines do not leave parallel to the trailing edge which violated the Kutta condition but there was no effect on the lift and pressure distributions even at higher values of k_f.

2.1.3 Nature of the wake

The early findings on the flapping flight of insect and bird are based on the assumption of quasi-steady aerodynamics where the angle of attack (θ_i) varies as the wing moves and the force is estimated from the θ_i of a static wing without considering the previous motion. Ellington et al [13] reported that some of the flying animals like bumble bee won't follow the laws of aerodynamics. By considering these studies, Wang [22] reported that the assumption of quasi-steady aerodynamics may yield promising results at high Re ($Re \geq 10^5$) but fails at low Re ($Re \leq 10^5$) due to increase in the unsteady vortex dynamics with respect to decrease in Re (below 10^5).

Katz and Plotkin [19] reported about Kelvin's theorem which was proposed by analysing the combination of translation and rotation of the airfoil in incompressible inviscid flow. Kelvin's theorem states that the total circulation with respect to time must remain constant in the flow field [19]. If there is any change in the bound vorticity (in the wake region of the airfoil), there must be an equivalent circulation of opposite sign. Therefore, the airfoil exhibiting periodic motion is expected to have a periodic vorticity in the wake region [19]. Krasny [23] reported that the strength of the vortex street depends on the induced velocities due to which the wake of the oscillating airfoil may consists of an array of alternating vortices with positive and negative signs. Von Karman

and Burger [24] first modelled such phenomena of alternating vortices by analysing the wake of the bluff body which was named as Karman vortex street. In this configuration, the vortices above the mean line rotate clockwise and the vortices below the mean line rotate counter clockwise, this wake structure is referred as drag-producing wake. The opposite nature of the alternating vortices where the vortices above the mean line rotate counter clock wise and the vortices below the mean line rotate clockwise is named as reverse Karman vortex street which is a thrust-producing wake.

The early theoretical studies [25, 26] and the experimental studies [27, 28, 29] on oscillating airfoil reported about thrust producing reverse Karman vortex street at certain combinations of flapping amplitude and frequency. A lot of pioneering experimental works [28, 29, 30, 31] characterised the wake of the plunging airfoil as drag-producing, neutral and thrust-producing depending on the operating conditions. However, the experimental studies carried by Lai and Plazer [32] on plunging airfoil at Re = 2×10^4 with $0\leq k_f \leq 8$ observed that the wake pattern doesn't have a smooth transition from Karman-Neutral-Reverse Karman. Rather there were a different types of transitional forms of wake where the shedding of multiple vortices per half cycle is witnessed instead of single vortex per half cycle. Lai and Plazer [32] also reported that these transition forms of the wake are highly dependent on the flapping frequency.

2.1.4 Dynamic stall

As the wing performs the prescribed motion, the flow over the wing surface separates and forms a LEV before reattachment. This LEV increases the instantaneous force coefficients noticeably by providing extra suction [13]. The LEV remains attached to the wing surface up to certain chord lengths and finally shed into the downstream of the wing forming a wake region. As the number of cycles increase, this process happens repeatedly and forms chaotic vortical pattern downstream of the wing due to which the instantaneous force coefficients suddenly drop [33]. This stalls the aerodynamic performance of the wing, such phenomenon is named as dynamic stall [34]. This phenomenon can be usually seen when the instantaneous angle of attack (θ_i) of the wing rapidly varies towards higher values [35, 36].

2.2 Modelling of low *Re* flows

To analyse the unsteady flow over the wing at low Re regime, different methods and techniques are employed. These methods can be categorised into three types, namely: Analytical, Experimental and the Numerical approach. The available methods are briefly

discussed in the following sections:

2.2.1 Analytical methods

A lot of analytical studies were carried out to model the unsteady flow at low *Re* regime. However, the complex nature of flow has limited the application of analytical methods at low *Re*. The quasi-steady approach is one such analytical method which was developed based on linear classical aerodynamic theories and employed in early days to analyse the unsteady flows at low *Re* regime. In this method, the forces are estimated by varying the instantaneous angle of attack without considering the pervious motion of the wing. Ellington [37, 38] first employed this quasi-steady approach to estimate the forces during flapping flight. After comparing the obtained findings with the experimental findings under same conditions, Ellington [37, 38] reported that this analytical approach yields much lower values of force coefficients than that of the experimental values. Sane and Dickinson [39] improved this quasi-steady approach by considering the effects of added mass and the rotational forces, but still didn't achieve closer values of resultant force coefficients compared to that of experimental results. The quasi-steady approach always underestimates the experimental measurements of force coefficients since the unsteady effects like dynamic stall, LEV formation and convection are not considered [40, 41]. Therefore, the quasi-steady approach is not a sufficient and reliable tool to model the unsteady flow at low *Re*.

The potential flow panel approach is another analytical method which was developed based on the inviscid flow assumption used in many studies to model the flow at low *Re* [19, 42, 43]. In the prediction of the trailing wake, this approach has shown a reasonably good accuracy. However, this approach fails to resolve the effect of LEV near the wing/airfoil surface due to the assumption of inviscid flow [14]. Further, the studies were carried out on some of the analytical methods reported in [25, 44, 35], which were developed based on unsteady aerodynamic thin airfoil theory with linear assumptions. The studies reported that these methods had shown a reasonable accuracy in 2D incompressible fully attached flows and 3D rotating flows [45]. Using these methods Garrack [46, 47] predicted the peak values of lift and thrust coefficients. Theodorsen [25] considered the added mass effect as a non-circulatory term and the shedding in the wake as a circulatory term to estimates the frequency domain solution of pitching and plunging plates. However, the extensive simplifications and omission of high viscous phenomena (which usually occurs at low *Re* regime) made the analytical methods as less reliable approach to model the low *Re* flows at high amplitudes and frequencies.

2.2.2 Experimental methods

Experiments were carried out in order to understand the unsteady flow characteristics of low Re flows [48, 49, 50, 51]. Fuchiwaki et al [50] reported that the vortical patterns of airfoil pitching at low Re are highly influenced by reduced frequency (k_f). It was also reported that the complex behaviour of these unsteady flows cannot be characterised by a single parameter like k_f, but a combination of multiple operating parameters like pitch amplitude (α_p), mean angle of attack (θ_m) and k_f. Koochesfahani [28] carried out a series of experiments at low Re pitching conditions, reported about the influence of k_f and α_p on thrust force generation and wake pattern. However, Koochesfahani [28] has shown less attention on exploring the actual three dimensional flow structures. The Particle Image Velocimetry (PIV) investigations carried out by Shih et al [52] on pitching airfoils reported that, the interaction between the vortices may affect the force coefficients and flow separation which may cause dynamic stall. It is observed that, Shih et al [52] considered only the effect of Re regime and the influence of other governing parameters is ignored. Buchner et al [53, 54] conducted a series of experiments using PIV to analyse the dynamic stall of the flat plate undergoing rapid pitching motion. They have discussed about the evolution of dynamic stall vortex and its interaction with the surface of the pitching plate. Widmann and Tropea [55] investigated the influence of Re on the formation of LEV on flat plate undergoing pitching motion. They have reported that the Re as a parameter which is responsible for the LEV separation from the airfoil surface. Yu and Bernal [56] experimentally analysed the unsteady flow around the pitching flat plates by using 2D PIV measurements at three different locations of the plates. It was reported that they have observed a reasonably good agreement with that of the findings reported using quasi steady potential flow methods. They have also reported that the reduction in the pitch rate and the location of pivot point can influence the formation of LEV. Machowski and Williamson [57] directly measured the thrust and propulsion efficiency of an airfoil performing pitching motion using a pair of force transducers. They have reported that the linear theory over predicts the mean thrust of the foil and concluded that the thrust force generation of the airfoil is largely insensitive to the wake vortex arrangements.

Apart from pitching, the plunging motion is also one of the most common unsteady condition at low Re flows. A lot of studies were reported on plunging/heaving motion of cylinders rather than airfoils/wings [58, 59]. The PIV investigations carried out by Lam et al [60] and Techet et al [61] reported that the formation and convection of vortices around the plunging cylinders vary with respect to the change in k_f and plunge amplitude (h_a). Lau et al [62] investigated the flow around the 2D airfoil performing plunging motion through PIV measurements. It was reported that the wake pattern is

highly influenced by LEVs and Trailing Edge Vortices (TEVs). Heathcote and Gursul [63] observed a deflection in this wake pattern by an angle with respect to the chord length of the airfoil depending up on the plunging amplitude and frequency. It was also reported that the TEVs have more predominant role in determining the aerodynamic performance of two dimensional plunging foils [64]. The PIV studies conducted by Freymuth [30] and Lai and Platzer [32] reported that the flow structure and the wake pattern downstream stream of the airfoil has almost similar variation with respect to plunging frequency as that of in the plunging cylinders. The experimental findings of Triantafyllou et al [65] also demonstrated that the resultant wake pattern could be in the form of drag producing, neutral or thrust producing. The literature also provided enough experimental evidence that the plunging airfoils can also produce thrust by forming reverse Karman street downstream of the airfoil. It was also reported that the wake pattern and the topology of the vortices have major contribution in the enhancement of propulsion efficiency of the plunging airfoil.

The flapping motion which is a combination of rotation about the axis along the wing chord and span, is a most common approach of thrust force generation in low Re applications. The flapping motion indeed has gained a considerable amount of attention. Freymuth [66] demonstrated about the importance of dynamic stall on the thrust force generation of airfoil by conducting experiments on 2D flapping airfoil. The 3D experimental studies carried out by Nagai et al [67] also discussed about the significance of dynamic stall and its influence on the instantaneous force coefficients which can be controlled by varying the flapping kinematics. The 3D flapping experiments conducted by Wang et al [68] reported that the variation in the instantaneous force coefficients are highly influenced by k_f and h_a. Singh and Chopra [69] have also drawn similar conclusions from their experimental observations as well.

The experimental studies have their own reputation and believed to ensure most accurate results of all the available methods. However, the distinct nature of experimental conditions, limitation of number of allowable tests and the availability of infrastructure all together makes it hard to generalise the unsteady nature of low Re flows. Therefore, the numerical approach can be an excellent candidate to govern the unsteady flow at low Re.

2.2.3 Numerical methods

Computational Fluid Dynamics (CFD) is widely used to analyse the complex nature of the flow at low Re. From the literature, most of the reported numerical studies at low Re can be characterised into three unsteady conditions namely: pitching, plunging and

flapping motions, which are elaborately discussed in the following sections.

2.2.3.1 Pitching motion

Most of the 2D and 3D studies where the pitching motion is considered were investigated at Re order of 10^5 or less. The inviscid numerical simulations cannot accurately resolve the high viscous nature of flow at these Re regimes [70, 71]. Therefore, most of the numerical studies use the Navier-Stokes (N-S) equations to represent the actual physics of the problem with desired accuracy. By utilizing the N-S equations, Akbari and Prince [72] simulated the flow field around the pitching airfoil using a vortex method. It was reported that the instantaneous forces and the resultant flow field are highly influenced by pitching frequency but Re has less impact on these force coefficients and the corresponding flow field. Okang and Knight [73] carried out 2D pitching numerical simulations at different Re. It was reported that the increases in Re causes the flow to recirculate on the leeward side of the airfoil and decrease in Re encourages the recirculation to happen near the leading edge. The numerical studies performed by Hamdani and Sun [74] on pitching airfoils, discussed about large unsteady forces and their resultant vortical structures. Visbal and Shang [75] reported that the increase in the reversed flow of the boundary layer increases the LEV formation and TEV shedding which eventually magnifies the unsteady nature of the flow around the airfoil.

2.2.3.2 Plunging motion

Plunging motion is one of the most common unsteady condition which also gained a lot of attention, same as that of pitching motion. Early studies of plunging motion are mainly focussed on cylinders rather than airfoils/wings due to their wide range of applications at high Re [76, 77, 78]. Later on the studies were also carried out on plunging airfoils and wings as well. The numerical studies performed by Andro and Jacquin [79] on plunging airfoil investigated about the significance of LEV, added mass and wake capturing. They have shown that the contribution of the LEV can be described as a quasi-steady analysis at lower frequencies. The added mass can be compared as a rotational force at higher frequencies. They have also reported that the wake capture shown to be greatly dependent on the frequency of oscillation and contributes higher lift force at particular frequencies. The 2D studies on plunging motion are further carried out to investigate the influence of the governing flow parameters like Strouhal number (St), Re regime, thickness ratio on different types of airfoils [80, 81]. It was reported that the viscous unsteady mechanisms also have a remarkable effect on the force coefficients and resultant flow field of plunging airfoils. Lewin and Haj-Hariri [82]

numerically investigated the flow characteristics of plunging airfoil, estimated the trust and power coefficients, also analysed the influence of LEVs and TEVs on the aerodynamic efficiency of the airfoil. It was reported that, the maximum efficiency was observed at a particular St where the LEV separation leads to a decrease in thrust force generation of the airfoil. Young and Lai [83] reported that instantaneous force coefficinets and the wake pattern of the plunging airfoil are highly influenced by k_f and St. They have also shown that the resultant flow field is strongly dependent on the LEV and TEV separation.

2.2.3.3 Flapping motion

The flapping motion is also one of the popular unsteady flow condition at low Re regime. A wide variety of studies are reported in the literature with different kinds of flapping motions. The flapping motion in most of the works is referred as the combination of rotations about the axes along the wing chord and span. The numerical simulations carried out by Lee et al [84] on flapping airfoil analysed about the role of LEVs and TEVs, reported that the LEVs can be more detrimental to the thrust rather than lift. It was also reported that the force generation mechanisms are different at upstroke and down stroke. Mittal et al [85] numerically investigated the flow field around the flapping airfoil and observed a reverse Karman vortex street at certain conditions which yields higher values of thrust force generation. Tang et al [86] investigated about the importance of delayed stall and wake capturing mechanism on a flapping airfoil. Bos et al [87] also found similar variation in the force coefficients of the flapping airfoil. Kaya and Tuncer [88] performs an optimization study on the flapping kinematics in order to estimate the maximum thrust and propulsion efficiency of a 2D airfoil by considering a non-sinusoidal flapping motion. They have reported that the maximum thrust coefficient can be achieved when the angle of attack is maintained almost constant during upstroke and down stroke and the pitching motion occurs at end of each stroke. However, such conditions are satisfied only when a very high acceleration is provided to the airfoil during pitching and plunging motion which may affect its propulsion efficiency. Sun and Tang [89] used N-S equations to examine the delayed, symmetrical and advanced rotations of the three dimensional hovering wing. Young et al [90] carried out a parametric study on three dimensional flapping wing and reported that, both lift and thrust forces are remarkably influenced by flapping frequency. Li and Dong [91] investigated the wake structure of finite aspect ratio wing undergoing a harmonic flapping motion. They have also extended their studies to investigate the effect of Re and St on the force coefficients of finite aspect ratio wing. They have reported that the topology of finite aspect ratio wing is different compared to the infinitely long wing. Ramamurthi and Sandberg [92] used

the three dimensional Finite Element Method (FEM) to simulate the flapping motion. They have investigated about the effect of phase angle between the pitching and plunging motions on the instantaneous force coefficients. They have reported that the advanced rotations may lead to higher thrust force generations than that of symmetrical and delayed rotations. Ramamurthi and Sandberg [93] also studied the three dimensional flapping motion at different conditions such as flexibility of wing and gust loading and compared the lift and thrust coefficients to assess the overall performance.

भारतीय प्रौद्योगिकी संस्थान गुवाहाटी
Indian Institute of Technology Guwahati

Chapter 3

Numerical Simulation Method

This chapter discusses about the governing equations, numerical formulation and the baseline problem setup employed in this work.

3.1 Introduction

Fluid dynamics is a branch of fluid mechanics, deals with the study of fluids in motion and the forces associated with it. The Computational Fluid Dynamics (CFD) is a set of numerical methods used for different purposes such as analysing the real time fluid flow problems. The equations representing the flow of the fluid are the governing equations of CFD. The current study employs the ANSYS FLUENT v 18.1 as a CFD package which uses the Navier-Stokes (N-S) equations to govern the fluid flow as the N-S equations has the potential to define the actual flow physics of real time problems with desired accuracy. The N-S equations can be compared as the application of Newton's second law of motion on the fluids. The N-S equations are defined based on three laws, namely: Conservation of mass, Conservation of momentum and the Conservation of energy [94].

3.2 Governing Equations

The first governing equation which is the law of conservation of mass (defined in Eq. (3.1)), states that the rate of change of mass within the control volume is equal to the net flow rate of the mass into the control volume.

$$\frac{d}{dt}\int_{\Omega}\rho(x,t)\mathrm{d}\Omega = \int_{\Omega} S_m(x,t)\mathrm{d}\Omega \tag{3.1}$$

where, $\rho(x,t)$ is the density of the fluid in the control volume Ω and $S_m(x,t)$ is the net mass flow rate per unit volume at given time t and position x. By considering $S_m(x,t)$

$= 0$, the Eq. (3.1) can be re-written as:

$$\frac{\partial \rho}{\partial t} + \nabla \cdot \rho U = 0 \tag{3.2}$$

where U is the velocity vector. For the current study, the incompressible flow is considered for which the density is constant. Therefore, Eq. (3.2) can be transformed as Eq. (3.3) which is also known as the continuity equation.

$$\nabla \cdot U = 0 \tag{3.3}$$

The second governing equation which is the law of conservation of momentum states that the rate of change of momentum within the control volume is equals to the summation of all the forces exerted on the control volume. Generally two types of forces act on the control volume, namely: body force and surface force.

$$\int_{\Omega} \rho \frac{DU_i}{Dt} \mathrm{d}\Omega = \int_{\Omega} \rho F_i \mathrm{d}\Omega + \int_{s} \rho R_i \mathrm{d}s \tag{3.4}$$

The surface integral in Eq. (3.4) must be converted into volume integral which can be done by defining stress tensor T_{ij} which is given by Eq. (3.5).

$$T_{ij} = -p\delta_{ij} + \tau_{ij} \tag{3.5}$$

Then the Eq. (3.4) can be transformed as follows:

$$\rho \frac{DU_i}{Dt} = \rho F_i + \frac{\partial T_{ij}}{\partial x_j} \tag{3.6}$$

The relation between the viscous stress and strain from Newtonian fluid is given as:

$$\tau_{ij} = \mu\left(\frac{\partial u_i}{\partial x_j} + \frac{\partial u_j}{\partial x_i} - \frac{2}{3}\frac{\partial u_r}{\partial x_r}\delta_{ij}\right) \tag{3.7}$$

By using Eq. (3.7), the final form of law of conservation of momentum of Navier-Stokes equation is presented in Eq. (3.8).

$$\frac{\partial U}{\partial t} + (U \cdot \nabla)U = -\nabla P + \left(\frac{1}{Re}\right)\nabla^2 U \tag{3.8}$$

The non-dimensional form of Eq. (3.8) is presented in Eq. (3.9) and Eq. (3.10).

$$(St)\frac{\partial \overline{U}}{\partial \tau} + (\overline{U} \cdot \nabla)\overline{U} = -\nabla \overline{P} + \left(\frac{1}{Re}\right)\nabla^2 \overline{U} \tag{3.9}$$

$$(k_f/\pi)\frac{\partial \overline{U}}{\partial \tau} + (\overline{U} \cdot \nabla)\overline{U} = -\nabla \overline{P} + \left(\frac{1}{Re}\right)\nabla^2 \overline{U} \tag{3.10}$$

where k_f and St are non-dimensional flapping frequency and Strouhal number defined in Eq. 3.14 and Eq. 3.15 respectively, $\overline{U} = (u/U_\infty,\ v/U_\infty,\ w/U_\infty)$, here u, v, w are components of the velocity vector U in X, Y and Z directions respectively, U_∞ is the free-stream velocity, $\overline{P} = P/\rho U_\infty^2$ and $\tau = \mathrm{t/T}$ (where T is flapping period). The resultant equations are the partial differential equations for which the exact analytical solution doesn't exist [94]. Therefore, the N-S equations are solved through numerical approach such as Finite Difference Method (FDM), Finite Element Method (FEM), Finite Volume Method (FVM) and spectral methods [94].

3.3 Turbulent flow

In general, the fluid flow is turbulent in nature which can be characterised as nonlinear, chaotic, irregular, time dependent. The flow of water released from a dam, the flow around a moving body such as cars or aeroplanes, smoke released from a cigar or chimney, stirring of coffee in a cup, etc., are the examples of real life turbulent flows. The Reynolds number (Re) is defined as the ratio between the inertia forces to the viscous forces, given from Eq. (3.11) to Eq. (3.13), generally used to define the nature of the flow i.e., laminar or transitional (laminar to turbulent) or turbulent [95].

$$Re = \frac{Inertia force}{Viscous force} \tag{3.11}$$

$$= \frac{\rho U_\infty C}{\mu} \tag{3.12}$$

$$= \frac{U_\infty C}{\nu} \tag{3.13}$$

The flow characteristics of the present study are also defined by two additional non-dimensional numbers, namely the reduced frequency or non-dimensional flapping frequency (k_f) and Strouhal number (St) given in Eq. 3.14 and Eq. 3.15 respectively,

$$k_f = \frac{2\pi f C}{U_\infty} \tag{3.14}$$

$$St = \frac{f \epsilon_w}{U_\infty} \tag{3.15}$$

where, U_∞, μ and ν are the velocity, dynamic viscosity and kinematic viscosity of the incoming fluid, C is the characteristic length (which is the chord length of the wing for present study), f is the frequency of oscillation and ϵ_w is the wake width which is twice

the plunge amplitude when only plunging motion is considered. The Direct Numerical Simulation (DNS) is one of the commercially available numerical techniques used to simulate the turbulent flows. The DNS solves the N-S equations for all scales of motions without considering approximations and averaging. This makes the DNS computationally expensive. The literature reported that the number of grid points required for DNS is of order of $Re^{9/4}$ which is extremely expensive for the flows with $Re \geq 10^3$ [96]. The Large Eddy Simulation (LES) is another numerical technique used to simulate the turbulent flow. The LES resolves the eddies greater than the grid size and model the eddies smaller than the grid size. As per the literature, the number of the grid points require for LES is of order of $Re^{1.8}$ which is also quite expensive [97]. Therefore, the present study uses the two equation model k-ω Shear Stress Transport (SST) which is computationally less expensive compared to DNS and LES to achieve the desired accuracy. The further details of k-ω SST model are discussed in details in the following sections.

3.3.1 k-ω SST model

Literature suggest that the ω equation (in standard k-ω model) offers different types of advantages over the ϵ equation (in k-ϵ model) [98, 99]. One of the most prominent advantage is that the ω equation can be integrated through the viscous sublayer without additional terms. This gives a relative straight forward formulation of robust y^+ Enhanced Wall Treatment (EWT). Further, it was also reported that the standard k-ω model is efficient in boundary layer flow and separation where adverse pressure gradients are involved. In ANSYS FLUENT, the standard k-ω model is incorporated based on the Wilcox's k-ω model which considers low Re effects, compressibility effects and the shear flow spreading [100]. However, the major limitation of the ω equation (in standard k-ω model) is that the ω equation is highly sensitive to the solution and over dependent on the free-stream values of k and ω outside the shear layer [101]. Due to this reason, the standard k-ω model is less popular in ANSYS FLUENT. Studies were carried out to fix the issues with the standard k-ω model and finally come up with the k-ω SST model where SST stands for Shear Stress Transport [98, 99, 101, 102].

The k-ω SST model was designed to overcome the free-stream sensitivity of standard k-ω model by combining elements of both the ω equation of standard k-ω model and the ϵ equation of k-ϵ model. By default, the k-ω SST model uses the enhanced wall treatment. The k-ω SST two equation model is generally in complete form and provides a closed system for modelling of CFD problems. Basically, the k-ω SST is an improvement over the standard k-ω and k-ϵ models. The k-ω SST model uses the definition of standard k-ω model at the inner parts of the boundary layer and the definition of k-ϵ at the outer parts

of the boundary layer. It was reported that the k-ω SST model can accurately estimate the flow separation from the smooth surfaces. With time, the k-ω SST model gained lot of attention and especially for aerodynamic flows, the k-ω SST model is considered as one of the most accurate and widely used models. It was also reported that the accuracy of the SST model is somewhat better than the Spalart-Allmaras model in predicting the characteristics of wall boundary layer.

$$\frac{\partial(\rho k)}{\partial t} + \frac{\partial(\rho k u_i)}{\partial x_i} = \frac{\partial(\Gamma_k \frac{\partial k}{\partial x_j})}{\partial x_j} + G_k - Y_k + S_k \tag{3.16}$$

The transport equations for the k-ω SST model are defined in Eq. (3.16) and Eq. (3.17) which are used to estimate the turbulent kinetic energy (k) and the specific dissipation rate (ω) respectively.

$$\frac{\partial(\rho \omega)}{\partial t} + \frac{\partial(\rho \omega u_j)}{\partial x_j} = \frac{\partial(\Gamma_\omega \frac{\partial \omega}{\partial x_j})}{\partial x_j} + G_\omega - Y_\omega + D_\omega + S_\omega \tag{3.17}$$

where, Γ_k and Γ_ω represents effective diffusivity of k and ω respectively (defined in Eq. (3.30) and Eq. (3.31) respectively). The terms G_k and G_ω are the generation of turbulent kinetic energy (k) and specific dissipation rate (ω) due to the gradients of mean velocity respectively (defined in Eq. (3.18) and Eq. (3.19) respectively). The terms Y_k and Y_ω represents the dissipation of k and ω respectively (defined in Eq. (3.40) and Eq. (3.49) respectively). The term D_ω is the cross diffusion term (defined in Eq. (3.54)). The terms S_k and S_ω are user-defined source terms for k and ω respectively.

$$G_k = -\rho u_i^1 u_j^1 \frac{\partial u_j}{\partial x_i} \tag{3.18}$$

$$G_\omega = \frac{\alpha}{\nu_t} G_k \tag{3.19}$$

where the coefficient α is given as:

$$\alpha = \frac{\alpha_\infty}{\alpha^*} \left(\frac{\alpha_0 + Re_t/R_\omega}{1 + Re_t/R_\omega} \right) \tag{3.20}$$

$$\alpha_\infty = F_1 \alpha_{\infty,1} + (1 - F_1) \alpha_{\infty,2} \tag{3.21}$$

$$\alpha_{\infty,1} = \frac{\beta_{i,1}}{\beta^*_\infty} - \frac{k^2}{\sigma_{\omega,1}\sqrt{\beta^*_\infty}} \tag{3.22}$$

$$\alpha_{\infty,2} = \frac{\beta_{i,2}}{\beta^*_\infty} - \frac{k^2}{\sigma_{\omega,2}\sqrt{\beta^*_\infty}} \tag{3.23}$$

where k =0.41 and the coefficient α^* is defined as:

$$\alpha^* = \alpha^*_\infty(\frac{\alpha^*_0 + Re_t/R_k}{1 + Re_t/R_k}) \tag{3.24}$$

where

$$Re_t = \frac{\rho k}{\mu\omega} \tag{3.25}$$

$$Re_k = 6 \tag{3.26}$$

$$Re_k = 2.95 \tag{3.27}$$

$$\alpha^*_0 = \beta_i/3 \tag{3.28}$$

$$\beta_i = 0.072 \tag{3.29}$$

for high Re, $\alpha = \alpha_\infty = \alpha^* = \alpha^*_\infty \approx 1$. The terms Γ_k and Γ_ω in Eq. (3.16) and Eq. (3.17) are the effective diffusivity of k and ω respectively,

$$\Gamma_k = \mu + \frac{\mu_t}{\sigma_k} \tag{3.30}$$

$$\Gamma_\omega = \mu + \frac{\mu_t}{\sigma_\omega} \tag{3.31}$$

where, σ_k and σ_ω are turbulent prandtl numbers for k and ω respectively. The turbulent viscosity μ_t can be computed by combining k and ω as follows:

$$\mu_t = (\frac{\rho k}{\omega})(\frac{1}{max(\frac{1}{\alpha^*}, \frac{SF_2}{a_1\omega})}) \tag{3.32}$$

where S is the magnitude of the strain rate, and

$$\sigma_k = \frac{1}{F_1/\sigma_{k,1} + (1-F_1)/\sigma_{k,2}} \tag{3.33}$$

$$\sigma_\omega = \frac{1}{F_1/\sigma_{\omega,1} + (1-F_1)/\sigma_{\omega,2}} \tag{3.34}$$

$$F_1 = \tanh(\Phi_1^4) \tag{3.35}$$

$$\Phi_1 = min[max(\frac{\sqrt{k}}{0.09\omega y}, \frac{500\mu}{\rho y^2 \omega}), \frac{4\rho k}{\sigma_{\omega,2} D_\omega^+ y^2}] \tag{3.36}$$

$$D_\omega^+ = max(2\rho \frac{1}{\sigma_{\omega,2}} \frac{1}{\omega} \frac{\partial k}{\partial x_j} \frac{\partial \omega}{\partial x_j}, 10^{-10}) \tag{3.37}$$

$$F_2 = \tanh(\Phi_2^2) \tag{3.38}$$

$$\Phi_2 = max(\frac{2\sqrt{k}}{0.09\omega y}, \frac{500\mu}{\rho y^2 \omega}) \tag{3.39}$$

where y is the distance to next surface. The terms Y_k and Y_ω in Eq. (3.16) and Eq. (3.17) are the dissipation of k and ω due to turbulence defined in Eq. (3.40) and Eq. (3.49) respectively.

$$Y_k = \rho \beta^* f_\beta^* k \omega \tag{3.40}$$

where, the piece wise function $f_\beta^* = 1$ for k-ω SST model.

$$\beta^* = \beta_i^* (1 + \xi^* F(M_t)) \tag{3.41}$$

$$\beta_i^* = \beta_\infty^* (\frac{4/15 + (Re_t/Re_\beta)^4}{1 + (Re_t/Re_\beta)^4}) \tag{3.42}$$

$$\xi^* = 1.5 \tag{3.43}$$

$$Re_\beta = 8 \tag{3.44}$$

$$\beta_\infty^* = 0.09 \tag{3.45}$$

here $F(M_t)$ is the compressibility function which is given as: $F(M_t) = 0$ when $M_t \leq M_{t_0}$ otherwise $F(M_t) = M_t^2$-$M_{t_0}^2$. where,

$$M_t^2 = \frac{2k}{a^2} \tag{3.46}$$

$$M_{t_0}^2 = 0.25 \tag{3.47}$$

$$a = \sqrt{\gamma RT} \tag{3.48}$$

the dissipation of ω is defined as:

$$Y_\omega = \rho\beta f_\beta \omega^2 \tag{3.49}$$

where f_β =1 for k-ω SST model and β_i is evaluated using Eq. (3.52)

$$\beta = \beta_i(1 - \frac{\beta_i^*}{\beta_i}\xi^* F(M_t)) \tag{3.50}$$

$$\beta_i = F_1\beta_{i,1} + (1 - F_1)\beta_{i,2} \tag{3.51}$$

$$\Omega_{ij} = \frac{1}{2}(\frac{\partial u_i}{\partial x_j} - \frac{\partial u_j}{\partial x_i}) \tag{3.52}$$

$$S_{ij} = \frac{1}{2}(\frac{\partial u_j}{\partial x_i} + \frac{\partial u_i}{\partial x_j}) \tag{3.53}$$

To blend both the standard k-ϵ and k-ω in order to define the k-ω SST model, the cross-diffusion term D_ω is introduced in Eq. (3.17) which is given in Eq. (3.54). The model constants $\sigma_{k,1} = 1.176$, $\sigma_{\omega,1} = 2.0$, $\sigma_{k,2} = 1.0$, $\sigma_{\omega,2} = 1.168$, $a_1 = 0.31$, $\beta_{i,1} = 0.075$, $\beta_{i,2} = 0.0828$. All the additional model constants has the same values as that of the standard k-ω model.

$$D_\omega = 2(1 - F_1)\rho\frac{1}{\omega\sigma_{\omega,2}}\frac{\partial k}{\partial x_j}\frac{\partial \omega}{\partial x_j} \tag{3.54}$$

3.3.2 Near wall region

The velocity profile for the turbulent flow can be divided into two regions namely: the viscous sub layer and the inertial layer. The outer line position of the inertial layer depends on Re. The increase in *Re* influences the extension of the inertial layer. In general, the higher grid resolution fully resolves the boundary layer near the walls. Therefore, the first cell height from the wall in the present study is computed using Eq. (3.55) by maintaining $y^+ = 1$ [99].

$$y^+ = \frac{u^* y_d}{\nu} \tag{3.55}$$

where u^* is the friction velocity, y_d is the nearest distance from the wall and ν is the kinematic viscosity of the fluid. The analytical expression in the viscous sub-layer is known for the k-ω model and the wall functions are approximated only for the logarithmic layer [103]. However, for the k-ϵ model, there is no analytical representation for the viscous

sub-layer. This indicate that the wall functions need to be approximated throughout the boundary layer and a lot of wall functions assume that the first grid point is within the fully turbulent low-law region. This assumption has a considerable amount of impact on the obtained results. Due to these reasons, the k-ω model can ensure more accurate solutions than that of the other models for the wall bounded flows [99, 101, 103].

3.4 Discretization

The computers do not directly solve the governing equations in the differential form rather consider in a discretized form. The process of discretization can also be referred as grid generation or meshing, which consists of dividing the fluid domain into discrete points (nodes or vertex) and volumes (cells or elements). There are two types of meshes, namely: Structured mesh and Unstructured mesh. The structured mesh usually consists of hexahedral elements and each grid point inside the mesh will be uniquely defined by the indices i, j and k. The advantage of using structured mesh is that it is easy to locate the cell and its neighbouring cells. This allows the solvers to quickly and easily calculate the data of any given cell by adding or subtracting the indices. However, the main drawback is that the process of achieving structured mesh becomes complicated with respect to the geometry. In some cases, advanced level skills required to the user to achieve structured mesh for complex geometries. The unstructured mesh can consists of all types of elements like tetrahedral, hexahedral, prism, wedge and pyramids. Depending on the choice of elements the unstructured mesh can also be referred as mixed or hybrid mesh. The grid points in the unstructured mesh do not have a particular order. Due to this, the unstructured mesh demands a more complex data structure to keep the track of each cell and its neighbouring cells which leads to high memory requirements than that of structured mesh. However, the biggest advantage of using unstructured mesh is that any complex geometry can be easily discretized and doesn't require much skills. Another advantage is that the user can provide the refinement and coarsening of the mesh as per the requirements.

3.4.1 Spatial discretization

Once, the fluid domain is discretized to form a mesh, the equations needs to be discretized. The three main methods most commonly used for the discretization are: Finite Difference Method (FDM), Finite Element Method (FEM) and Finite Volume Method (FVM) [104]. The ANSYS FLUENT utilises the FVM where the domain is discretized into control volumes and the surface integrals are calculated. The accuracy of the dis-

cretization highly influenced by the schemes employed to define the control volume. Most commonly used schemes are cell-centred scheme and cell-vertex scheme. The ANSYS FLUENT uses the cell-centred scheme to define the shape and position of the control volume ($\Omega_{I,J}$) [105].

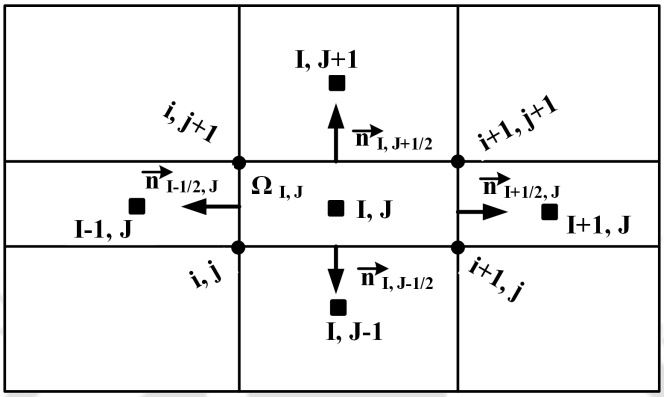

Figure 3.1: Schematic representation of cell-centered scheme

The control volumes in the cell-centred scheme are identical to the grid cells and the flow variables are stored at the centre of each cell as shown in Fig. 3.1. The variables will be obtained by utilizing the average of the fluxes which are computed from the values of the cells to the left and to the right. The cell-centred scheme strongly depends on the smoothness of the mesh. If the mesh is sufficiently smooth then the cell-centred scheme can reach second or higher order accuracy. For unstructured mesh, the control volumes formed by using cell-centred scheme are approximately 3-6 times greater than that of cell-vertex scheme. Due to this, the cell-centred scheme is considered more accurate (in the case of unstructured mesh) however it requires twice the memory as this scheme saves more data of the field variables than that of the cell vertex scheme. For structured meshes, both the schemes have almost equivalent control volumes and the computational advantage is almost same.

3.4.2 Temporal discretization

In order to perform transient simulations, the equations of motion must be discretized in both space and time. The spatial discretization of time-dependent equations is equivalent to the steady-state case. The temporal discretization of the equations in the differential form consists of integration of each term over a time step (t^*). The ANSYS FLUENT by default uses the implicit time integration when pressure-based solver is selected [105, 104]. The explicit time integration is only available with density-based solver. The major advantage of using implicit time integration is that the scheme is unconditionally stable with respect to the size of the time step. Therefore the time-step is not limited by the

Courant-Friedrichs-Lewy (CFL) condition [104]. The velocity components are presented in both continuity and momentum equations and the convective terms are non-linear. Therefore, these problems are addressed by considering iterative solution methods and setting up the solver as follows:

- For pressure-velocity coupling, coupled scheme is opted.
- The evaluation of the gradients is performed using least squares cell based method.
- The pressure interpolation is carried out using second order scheme.
- The Bounded central differencing scheme is used for the convective term of momentum.
- For turbulent kinetic energy and specific dissipation rate, the second order upwind scheme is used.
- An implicit second order accurate scheme is employed for time integration.

3.5 Boundary conditions

The present study investigates about the flow field around the wing performing different motions. Therefore the solution of the respective governing equations require the flow properties like velocity and pressure to be specified on the computational domain. The boundary condition on each surface of the domain are described as follows:

- On the inflow surface, the velocity is specified (Dirichlet condition) based on corresponding Re and zero gradient condition of pressure (Neumann condition) is maintained.
- On the outflow surface, the free stream value of pressure is maintained (Dirichlet condition) and the velocity is kept at zero gradient condition (Neumann condition).
- The symmetry boundary condition is given to the surface which is in contact with the wing to ensure all the fluxes are zero.
- All the other surfaces including the wing and the wing tip are provided with no-slip wall boundary condition to ensure a fixed velocity and zero pressure gradients.

3.6 Mesh motion

The conservation equation for the any moving body (for the present study the moving body is the wing subjected to the prescribed motion) in the integral form is defined in Eq. (3.56).

$$\frac{\partial}{\partial t}\int_{\Omega}\rho\Psi \mathrm{d}\Omega + \oint_{s}\rho\mathbf{n}.(\mathbf{V}_f - \mathbf{V}_m)\Psi \mathrm{d}S - \oint_{s}\rho(\Gamma_\Psi)\mathbf{n}.(\Delta_\Psi)\mathrm{d}S = \int_{\Omega} S_\Psi(\Psi)\mathrm{d}\Omega \tag{3.56}$$

where Ψ refers to the conservative intensive property for which $\Psi = 1$ for conservation of mass and $\Psi = \mathbf{V}_f$ for conservation of momentum. The terms V_f and V_m are the velocities of the fluid and the moving mesh respectively. The term s denotes the surface surrounded by the control volume Ω where $\mathbf{n}$ is the outward unit vector perpendicular to the surfaces. Also, Γ_Ψ refers to the diffusion coefficient of Ψ, Δ_Ψ is the gradient of Ψ and S_Ψ refers to the source of Ψ per unit volume. The solver calculates the time derivative in Eq. (3.56) using first-order backward difference formula as shown Eq. (3.57) to Eq. (3.61) if the first order differencing scheme is selected [104].

$$\frac{\partial}{\partial t}\int_{\Omega}\rho\Psi \mathrm{d}\Omega = \frac{(\rho\Psi\Omega)^{i+1} - (\rho\Psi\Omega)^{i}}{\Delta t} \tag{3.57}$$

where, i and i+1 indicates the respective quantities during current and next time steps respectively. The volume Ω^{i+1} at $i + 1^{th}$ time step can be estimated as:

$$\Omega^{i+1} = \Omega^{i} + \frac{d\Omega}{dt}\Delta t \tag{3.58}$$

where $\frac{d\Omega}{dt}$ is the volume time derivative of the control volume Ω. To ensure the mesh conservation law is satisfied, the volume time derivative of control volume is estimated as follows:

$$\frac{d\Omega}{dt} = \oint_{s}\mathbf{V}_m.\mathrm{d}S \tag{3.59}$$

and finally the solver calculates the volume time derivative of control volume as follows:

$$\frac{d\Omega}{dt} = \sum_{j=1}^{T_f}\mathbf{V}_{m,j}.S_j \tag{3.60}$$

where, T_f is the total number of faces on the control volume Ω and S_j is the face area vector. The dot product $\mathbf{V}_{m,j}.S_j$ can be calculated from Eq. (3.61):

$$\mathbf{V}_{m,j}.S_j = \frac{\delta \mathbf{V}_j}{\Delta t} \tag{3.61}$$

where, $\delta \mathbf{V}_j$ represents the volume swept out by the control volume face j on a given time Δt. Whenever the second order differencing scheme is selected then the solver calculate the time derivative in Eq. (3.56) using second order backward difference formula using Eq. (3.62) [104].

$$\frac{\partial}{\partial t}\int_{\Omega} \rho \Psi \mathrm{d}\Omega = \frac{3(\rho\Psi\Omega)^{i+1} - 4(\rho\Psi\Omega)^{i} + (\rho\Psi\Omega)^{i-1}}{2\Delta t} \tag{3.62}$$

where i-1, i and i+1 represent the respective quantities from successive time steps. In the second order differencing scheme, on each face of the control volume, the dot product $\mathbf{V}_{m,j}.S_j$ is estimated using Eq. (3.64).

$$(\mathbf{V}_{m,j}.S_j)^{i+1} = \frac{3}{2}(\mathbf{V}_{m,j}.S_j)^{i} - \frac{1}{2}(\mathbf{V}_{m,j}.S_j)^{i-1} \tag{3.63}$$

$$= \frac{3}{2}[\frac{\delta \mathbf{V}_j}{\delta t}]^{i} - \frac{1}{2}[\frac{\delta \mathbf{V}_j}{\delta t}]^{i-1} \tag{3.64}$$

भारतीय प्रौद्योगिकी संस्थान गुवाहाटी
Indian Institute of Technology Guwahati

Chapter 4

Aerodynamic Investigation of the Stationary Biomimetic Wing inspired from Passer Domesticus

This chapter presents the study of a biomimetic wing inspired from a natural flyer (Passer Domesticus). Since the birds have thin wings, Bergey BW-3, a thin and highly cambered airfoil, is used to model the wing cross-section. To investigate the aerodynamic characteristics of the biomimetic wing, numerical and experimental studies are carried out at low Reynolds number (Re). It is observed that the numerical findings has similar trend as that of the experimental observations. The performance of the biomimetic wing is compared with rectangular and elliptical wings in terms of instantaneous force coefficients. Further, the flow field around the biomimetic wing is also analysed in order to understand the reasons behind its better performance than that of other wing planforms.

4.1 Introduction

Most of the studies reported in the literature have investigated the aerodynamic characteristics of commercially available wing planforms. Selig et al [106] performed a series of experiments on different airfoils at Reynolds number ranging from 6×10^4 to 3×10^5 but paid very less attention towards wings with small aspect ratio. Gabriel and Mueller [107] carried out wind tunnel experiments on four distinct wing planforms namely rectangular, elliptical, Zimmerman and inverse Zimmerman with aspect ratios varying from 0.5 to 2 at $7\times10^4 \leq Re \leq 2 \times 10^5$. They reported the aspect ratio as the primary, wing planform as secondary and Re regime as the ternary influencing parameter on the

aerodynamic performance of low aspect ratio wings at low Re. Laitone [108] carried out wind tunnel experiments on rectangular planform at 2.07×10^4 and concluded that sharp leading edge has better aerodynamic lift than that of sharp trailing edge at low Re. Kalpan et al [109] carried out water tunnel experiments at 8×10^3 and 24×10^3 on semi elliptical, delta and rectangular wing planforms. Kalpan et al [109] had shown that the wake structures of the above mentioned wing planforms were different but the slope of lift-curve was almost same at those conditions. Okamoto and Azuma [110] conducted wind tunnel tests on elliptical, rectangular and triangular wing planforms at low $Re = 1\times10^4$. They have reported a non-linear variation in lift and drag coefficients at different aspect ratios over a wide range of angle of attack. Pelletier and Mueller [1] performed wind tunnel experiments on flat and cambered plates by varying the Reynolds number from 6×10^4 to 2×10^5. They have reported that the turbulence intensity and trailing edge effects do not have a major impact on the lift and drag coefficients at low Re.

Most of the aforementioned studies had investigated the aerodynamic characteristics of commercially available wing planforms. The present work aims to establish a novel wing planform in a simplified manner by considering the wing planform of Passer Domesticus (House sparrow) as a reference. Passer Domesticus uses its wings to generate almost all of the aerodynamic forces required for flight. Even though the tail and the body also contribute to flight control and lift enhancement, in fixed wing MAVs such features can be taken care by introducing either jets or propellers. The current chapter mainly focuses on modelling of the biomimetic wing with the dimensions corresponding to that of a MAV and make efforts towards gaining a preliminary understanding of its aerodynamic characteristics. While modelling the wing cross section, Bergey BW-3 airfoil is introduced at different sections of the wing planform. After modelling of biomimetic wing, its aerodynamic characteristics are investigated numerically and experimentally at $2.5\times10^4 \leq Re \leq 1\times10^5$. Thereafter, the aerodynamic performance of the biomimetic wing is compared by modelling rectangular and elliptical wing planforms using the same dimensions and cross section. Additionally, the flow field around the biomimetic wing is also explored at $Re = 5\times10^4$. The details of geometry, the associated numerical and experimental analysis are presented in the following sections.

4.2 Method

4.2.1 Wing geometry

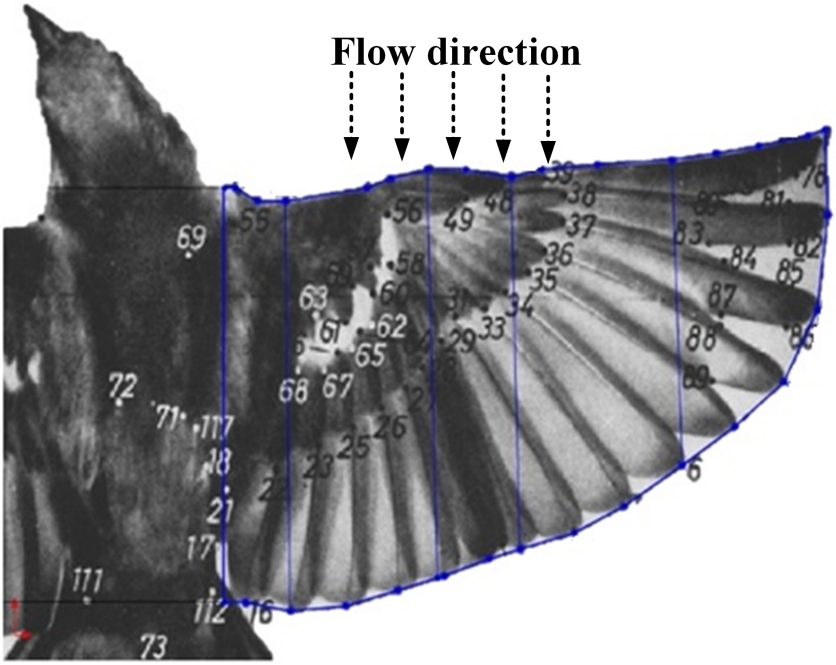

(a) B-spline interpolation

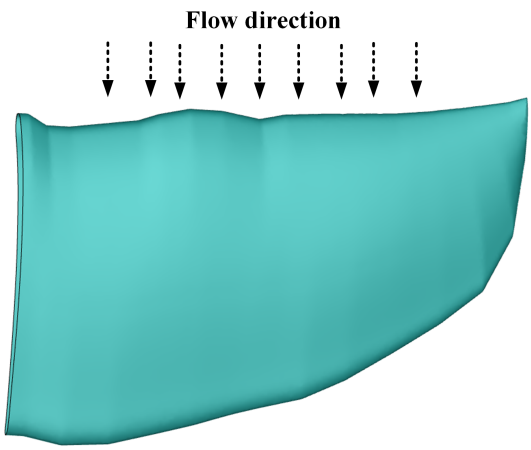

(b) CAD model of the wing

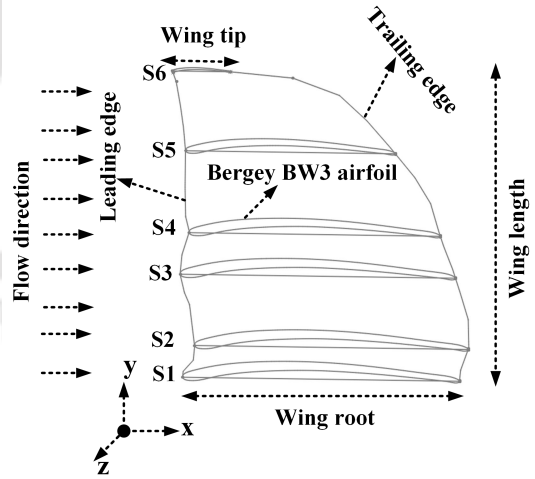

(c) Inside the wing

Figure 4.1: 3D modelling of Passer Domesticus wing planform

A biomimetic wing is modelled by considering the wing planform of Passer Domesticus bird as a reference. The schematic representation of 3D modelling of the biomimetic wing is presented in Fig. 4.1.

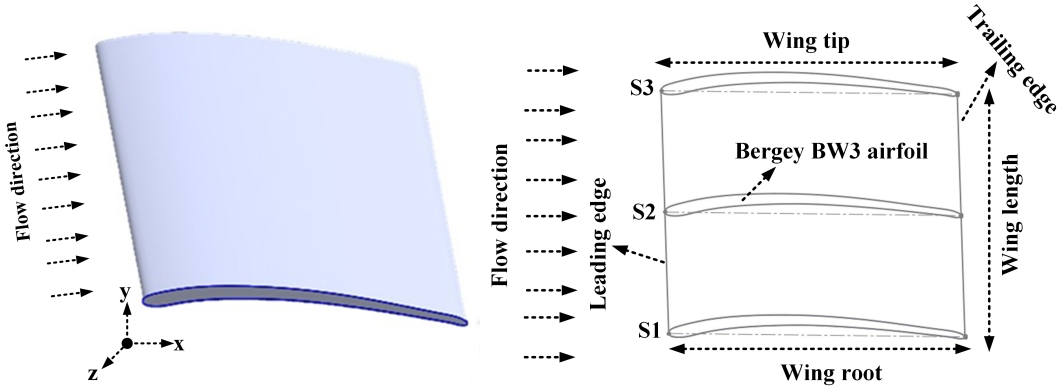

(a) CAD model of the wing (b) Inside the wing

Figure 4.2: 3D modelling of rectangular wing planform

As for the cross sectional shape of the Passer Domesticus wing, a thorough review of the literature was carried out. It is observed that most of the pioneering works reported about the changes in the wing structure of Passer Domesticus at different flight conditions and had shown very little attention on cross sectional shape of the Passer Domesticus wing [111, 112, 113]. Therefore, the cross section of the wing is modelled by introducing an ad hoc airfoil into the wing planform. Since the birds have thin wings with thickness to chord length $(t/C) \leq 6\%$ [1], the cross section of the wing is modelled by introducing a thin and highly cambered airfoil. In the present study, Bergey BW-3 airfoil is considered because of its unique design of having a pultruded section which yields to a relative thickness of 5% and helps in designing and manufacturing wings with close dimensional cross sections.

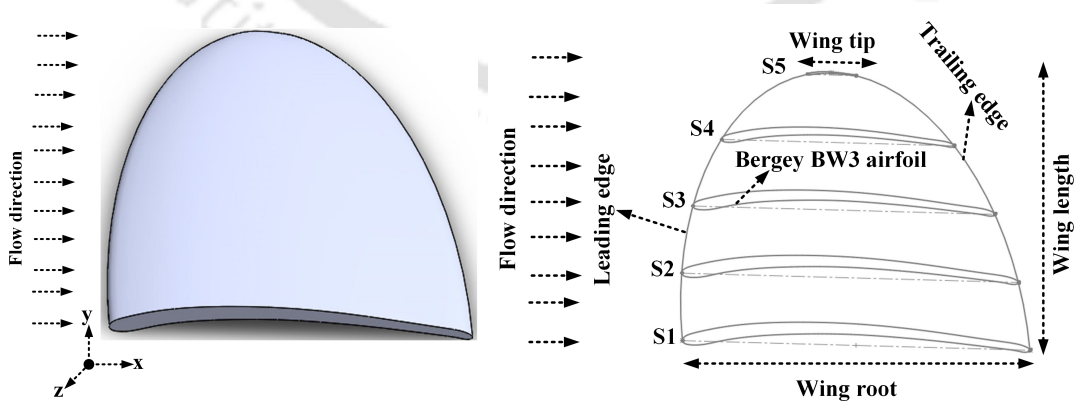

(a) CAD model of the wing (b) Inside the wing

Figure 4.3: 3D modelling of elliptical wing planform

Further, it was reported that the Bergey BW-3 airfoil doesn't experience the for-

mation of large separation bubble in the low Re regime ranging from 6×10^4 to 10×10^4 which makes this airfoil as a more suitable candidate for the current study [106]. As the wing planform varies with respect to span, the Bergey BW-3 airfoil is introduced at different sections (S1 to S6) of the wing while designing the wing cross section as shown in Fig. 4.1(c). The wing has a chord length of 75 mm at the wing root with a wing area of 82.84 cm^2 and the semi-span aspect ratio of the wing is 1.2. The wing has a maximum thickness of approximately 3.75 mm at a distance of 5.5 mm from the leading edge. For the upcoming discussions of the present study, the combination of wing planform of the Passer Domesticus and the Bergey BW-3 wing cross section is referred as a biomimetic wing. The conventionally adopted rectangular and elliptical wing planforms are considered for comparative assessment on the aerodynamic performance of the biomimetic wing. Both the wings are modelled using same dimensions and cross section as shown in Fig. 4.2 and Fig. 4.3.

4.2.2 Numerical procedure

The mass and momentum conservation equations in the dimensionless form which governs the incompressible flow over the wing are already defined in Eq. (3.3) and Eq. (3.8) of Section 3.2 in Chapter 3. The mean lift and drag coefficients of the wing are calculated using Eq. (4.1) and Eq. (4.2):

$$C_L = \frac{\frac{1}{T}\int_0^T f_l(t)\mathrm{d}t}{\frac{1}{2}\rho A U_\infty^2} \tag{4.1}$$

$$C_D = \frac{\frac{1}{T}\int_0^T f_d(t)\mathrm{d}t}{\frac{1}{2}\rho A U_\infty^2} \tag{4.2}$$

where $f_l(t)$ and $f_d(t)$ are the instantaneous lift and drag forces respectively, T is the time period of the cycle. The flow around the wing is simulated by solving the aforementioned three dimensional Navier-Stokes equations using a commercial Computational Fluid Dynamics (CFD) package ANSYS FLUENT v18.1 based on finite volume approach assuming the flow is incompressible. The modelling of turbulent flow around the wing, details regarding the near wall region, spatial and temporal discretization, solver settings and boundary conditions are elucidated from Section 3.3 to 3.5 in Chapter 3. In order to achieve a converged solution, the residuals are set to fall below 10^{-15}. An initial time refinement study was carried out with time step (t^*) = 5×10^{-3} s, 1×10^{-3} s, 5×10^{-4} s and 1×10^{-4} s. It is observed that there is no variation in instantaneous force coefficients at $t^* = 5\times10^{-4}$ s and 1×10^{-4} s. Therefore, the time step is fixed at $t^* = 5\times10^{-4}$ s with

a total number of time steps of 1×10^5. There are 35 iterations in each time step. The higher number of iterations is not considered since there is no improvement in the convergence during each time step. The stopping criteria for each simulation are set in such a way that, the simulation will stop either all the residuals fall below the specified value (10^{-15}) or the total number of time steps is reached (1×10^5). Also the same simulation will be continued by increasing either the residual value or the number of time steps if considerable variation between the instantaneous lift and drag coefficients between 10 consecutive time steps is observed. The efficiency and the accuracy of the solver are thoroughly verified and well documented in the literature [114, 115].

4.2.2.1 Computational domain

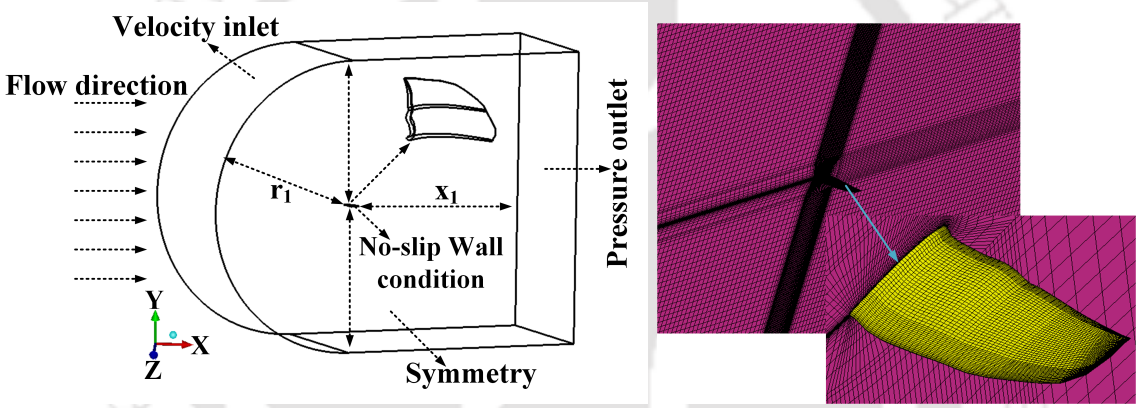

(a) Computational domain (b) Structured mesh

Figure 4.4: Details of computational domain and the mesh around the wing

A semi-spherical fluid domain is modelled for the present numerical study as shown in Fig. 4.4(a). The blocking strategy is used in combination with O-grids to achieve structured mesh to the whole domain and to the wing with hexahedral elements in Integrated Computer-aided Engineering and Manufacturing - Computational Fluid Dynamics (ICEM-CFD) as shown in Fig. 4.4(b). In order to effectively capture the development of the flow, the first cell height of 2.85×10^{-5} is maintained and the corresponding y^+ value is 1. The inner O-grid of the domain is provided with a cell growth rate of 1.03 and the rest of the domain has a growth rate of 1.5. This ensures a denser mesh around the wing. An initial domain dependence test was carried out at mean angle of attack $(\theta_m) = 4^\circ$ with $Re = 5\times10^4$ to assess the sensitivity of the results with respect to domain size. The dimensions of the different domains and the corresponding mean lift coefficient (C_L) are presented in Table 4.1. The error percentage is calculated based on the C_L values of two consecutive domains. It is observed that the overall error is less than 1%.

Table 4.1: Comparison of mean lift coefficients of biomimetic wing using different sizes of domain at $\theta_m = 4°$ and $Re = 5 \times 10^4$ (where C refers to the chord length at the wing root)

Domain	radius (r_1)	distance (x_1)	C_L	Error(%)
Type 1	15C	25C	0.5275	–
Type 2	30C	50C	0.5289	0.26
Type 3	45C	75C	0.5283	0.11

The only drawback in the dimensions of the Type 1 domain is that the inlet and outlet surfaces are not far enough from the wing leading edge and trailing edge respectively. Due to this, reversed flow occurs in the domain at every time step of the simulation for higher angles of attack when $\theta_m \geq 10°$. Therefore in order to minimise the outer boundary effects, the inlet surface is kept at a distance of $30C$ from the leading edge of the wing root. The outlet surface is maintained at a distance of $50C$ from the trailing edge of the wingtip. The velocity inlet and pressure outlet conditions are applied at inlet and outlet surfaces. The symmetry condition is specified to the surface which is attached to the wing. The no-slip wall boundary condition is applied on the wing and also to the rest of the surfaces. The no-slip boundary condition of current study ensures zero velocity ($\frac{\partial u}{\partial y} = 0$, v = 0, w = 0) at the wall with a temperature of 288.15 K. The dimensions and boundary conditions of the computational domain are presented in Fig. 4.4.

4.2.2.2 Mesh sensitivity analysis

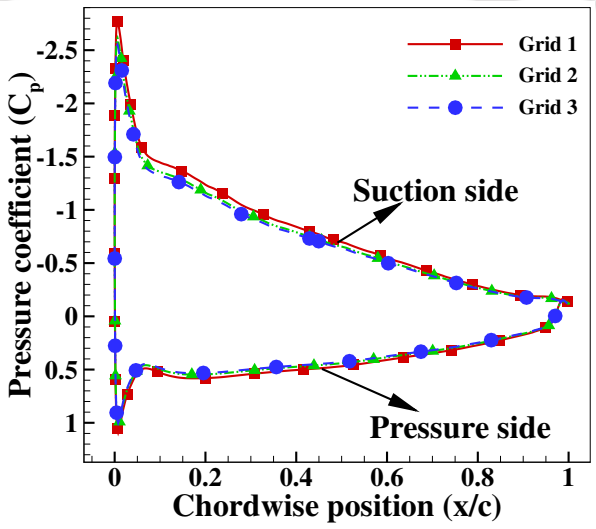

Figure 4.5: Variation in the pressure coefficient of the biomimetic wing at $\theta_m = 12°$ and $Re = 5{\times}10^4$ with three different grids

To inspect the accuracy of the results with respect to grid size and grid quality, the grid independence test is carried out on the biomimetic wing by calculating pressure coefficient at $\theta_m = 12^\circ$ and $Re = 5{\times}10^4$. The obtained findings are presented in Fig. 4.5. The mean lift and drag coefficients of the biomimetic wing at $\theta_m = 12^\circ$ and $Re = 5{\times}10^4$ are also calculated using three different grids, presented in Table 4.2 along with the size and quality of each grid. From Fig. 4.5 and Table 4.2, it is observed that the highest error of 6.47% is observed between the findings of Grid 1 and Grid 2. Also, a maximum error of 2.46% is noticed between the findings of Grid 2 and Grid 3. The findings obtained using Grid 2 and Grid 3 do not show much variation than that of Grid 1, further evaluation is carried out to validate the accuracy of each grid by considering the findings reported by Pelletier and Mueller [1] as a reference using the same grids. Pelletier and Mueller [1] carried out experimental investigations on cambered plates with 4% camber and semi span aspect ratio of 1.5 at $Re = 6 \times 10^4$ over a wide range of angle of attack.

Table 4.2: Comparison of mean lift and drag coefficients of biomimetic wing at $\theta_m = 12^\circ$ and $Re = 5{\times}10^4$ using different grids (Min OQ refers to Minimum orthogonal quality)

Mesh type	No. of elements	Min. OQ	C_L	Error(%)	C_D	Error(%)
Grid 1	$4.5{\times}10^5$	$1.12{\times}10^{-1}$	1.0602	–	0.1382	–
Grid 2	$8.1{\times}10^5$	$2.23{\times}10^{-1}$	1.0315	2.78	0.1298	6.47
Grid 3	$15.4{\times}10^5$	$2.96{\times}10^{-1}$	1.0114	1.95	0.1266	2.46

A numerical study is carried out using the three grids having same specifications as that of presented in Table 4.2 at $\theta_m = 4^\circ$ by considering the above conditions as a reference and the obtained mean lift and drag coefficients with respect to the grid size and quality is presented in Table 4.3. The mean lift and drag coefficients of cambered plates at $\theta_m = 4^\circ$ reported by Pelletier and Mueller [1] is used to calculate the error percentage. It is observed that the Grid 1 predicts slightly higher values than that of the other grids with respect to the findings reported by Pelletier and Mueller [1]. But the findings obtained using both Grid 2 and Grid 3 have encouraging agreement with the findings reported by Pelletier and Mueller [1]. However, a computationally less expensive grid i.e., Grid 2 in the present study is opted for further numerical analysis.

Table 4.3: Comparison of mean lift and drag coefficients of cambered plate (4% camber) using different grids at $\theta_m = 4^\circ$ and $Re = 6 \times 10^4$

Mesh type	Avg lift coefficient(C_L)	Error(%)	Avg drag coefficient(C_D)	Error(%)
Grid 1	0.5621	12.42	0.0679	19.12
Grid 2	0.5179	3.58	0.0593	4.03
Grid 3	0.5177	3.54	0.0591	3.68

4.2.3 Experimental procedure

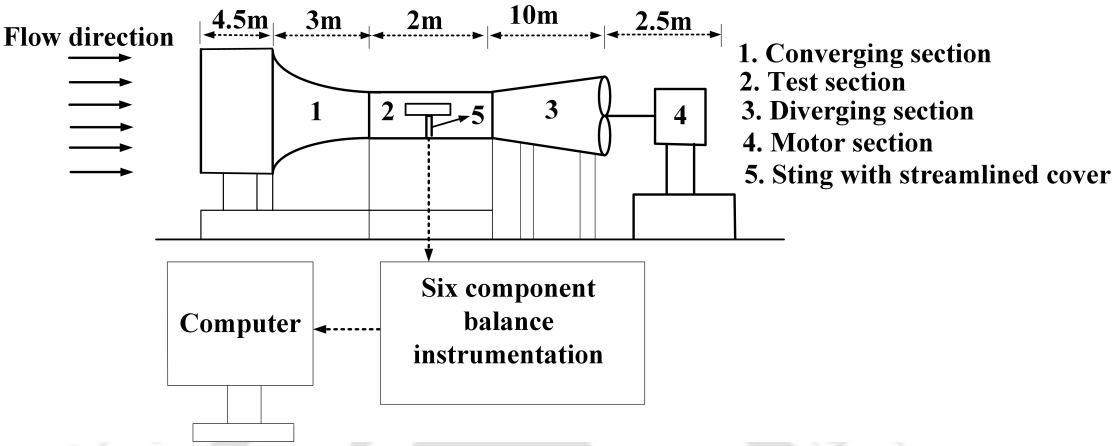

Figure 4.6: Schematic view of wind tunnel

The experiments were carried out using a low turbulence, open-circuit wind tunnel with closed type test-section located at the Indian Institute of Technology Guwahati. The wind tunnel consists of three sections namely, converging section, interchangeable test-section and diverging section. The entrance and test section has square cross section. The dimensions of the test section are 60 cm×60 cm×200 cm. An impeller is mounted at the end of the diverging section which is driven by high speed electric motor. The experiments in the wind tunnel can be performed up to a maximum speed of approximately 50 m/s by varying the motor speed. The schematic view of the wind tunnel is presented in Fig. 4.6.

Figure 4.7: Wind tunnel front view

In the current study, all the wind tunnel experiments are performed at the chord Reynolds number range of $2.5 \times 10^4 \leq Re \leq 1 \times 10^5$ and the corresponding range of

velocities are easily maintained. The aerodynamic loads are measured using specially designed six component force balancing instrument (WBAL-00106). The functional components of the balancing instrument consists of balance mechanism, strain gauge based instrumentation amplifiers and the micro-controller based measuring system. From the outer side, the balancing instrument is designed to look like a vertical sting like section with a length of 355mm which can be protruded into the test section as shown in Fig. 4.7. The wing models can be hinged to the top of the vertical sting through a metric plate where the mounting mechanism is provided. The sting was covered by a streamlined cover to minimise the sting's interference on the drag coefficient of the wing. As per the manufacturer, $\pm 0.5\%$ variation in the aerodynamic drag can be observed due to tare effects and sting interference. The metric plate which is fixed to the top of the vertical sting transfers all the loads generated on the wing model to six straining components through a linkage system. These straining components are arranged in the form of a cantilever linkage system in order to sense or respond with respect to the loads generated on the wing models. The strain gauges are attached to the root of the cantilever system such that the whole arrangement forms a full-bridge circuit and the output of the full-bridge circuit is directly proportional to the load which acts on the cantilever linkage system. In overall, the balancing instrument is equipped with six straining components with six full-bridge circuit arrangements capable of measuring forces and moments in X, Y and Z directions which in total are the six components of forces. Additionally, the signal-conditioning amplifiers with low drift and high stability are used to amplify the output from the strain gauges which were fixed on the straining elements to obtain a large gain of up to 3100. A micro-controller based measuring system is used to measure the output from these signal-conditioning amplifiers. Finally, the measured signals of voltages or loads are transferred to the computer through an external cable (RS-232) for further post-processing. From the literature, a lot of the experimental analyses are carried out to investigate the aerodynamic characteristics of three dimensional wings without using end plates and achieved good accuracy [116, 117]. Therefore, the end plates are not used in the present study as the end plates are usually installed to mitigate the three dimensional effects. The 3D printed wing models were with appropriate angle of attack before closing the test section (as shown in Fig. 4.7), by following the procedure similar to that of Roy et al [116]. The force balance is designed in such a way that the maximum angle of attack can be set from -15° to 15°. Therefore, all the experimental measurements were carried out up to 14° angle of attack, starting with -8° in steps of 2°. Thereafter, the angle of attack was reduced to 0° from 14° to check the presence of hysteresis. In all of the measurements, no hysteresis was found.

4.2.4 Uncertainty and Validation

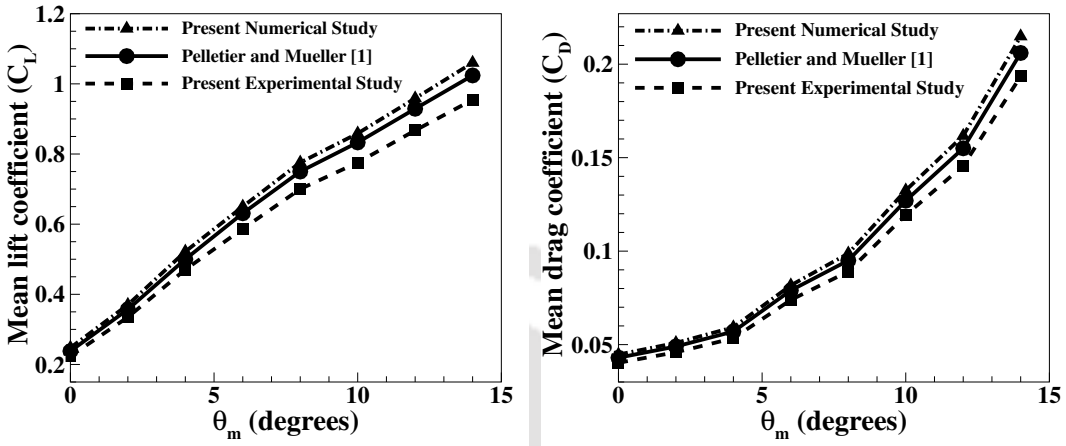

(a) Lift coefficient (b) Drag coefficient

Figure 4.8: Experimental and numerical comparison of aerodynamic performance of cambered plate (4% camber) with respect to angle of attack at $Re = 6{\times}10^4$ along with the experimental findings of Pelletier and Mueller [1]

The least count of the balancing instrument is approximately 1 gram. For the purpose of calibration, the calibration plate along with its arm is bolted to the balancing instrument, this ensures to apply the loads (in steps) in the primary load directions. The calibration of the balancing instrument is achieved by applying the calibrated weights (in steps) in each of the primary load direction. The reading are taken before and after loading the weights. It is observed that the response of the balancing instrument is effectively linear over the full range. The uncertainties in the experimental measurements are carried out by adopting the prescribed methods [118]. The uncertainties related to independent parameters of the present experimental analysis are as follows: the angle of attack settings over the load cell is ±1.25%. The uncertainty during velocity adjustments are ±0.7%. The uncertainties in load calibrations of the six-component force balance has ±0.25% in x-direction and ±0.8% in y-direction. The effect of blockage on the force coefficients is estimated by using empirical relations, methods and charts provided by Pankhrust and Holder [119] and Rae and Pope [120]. As per the literature, the experimental findings of lift and drag coefficients are mainly affected by three types of blockages, namely: solid blockage (ϵ_{sb}), wake blockage (ϵ_{wb}) and the streamlined curvature (ϵ_{sc}). The estimated values of these correction factors are: $\epsilon_{sb} = 0.0044$, $\epsilon_{wb} = 0.0024$ $\epsilon_{sc} = 0.0007$. The dynamic pressure is corrected by a factor q_c/q, which is given

by Eq. (4.3) [121]:

$$q_c/q = (1 - \epsilon_m)^2 \tag{4.3}$$

where, ϵ_m is the maximum blockage ($\epsilon_m = \epsilon_{sb} + \epsilon_{wb} + \epsilon_{sc}$) estimated from the wind tunnel. The corrected values of force coefficients are given by Eq. (4.4) and Eq. (4.5) [122]

$$C_{l_{exp}} = C_l^1(q_c/q) \tag{4.4}$$

$$C_{d_{exp}} = C_d^1(q_c/q) \tag{4.5}$$

where, C_l^1 and C_d^1 are the measured values of lift and drag coefficients respectively from the wind tunnel, $C_{l_{exp}}$ and $C_{d_{exp}}$ are the corrected values of lift and drag coefficients respectively by considering total blockage from the wind tunnel. It is observed that the variation between the measured values and the corrected values of lift and drag coefficients is around 1.8%. Since the thickness and volume of the wings are small, a very limited effect of blockage is observed. In order to estimate the overall deviation in the mean lift and mean drag calculations, an initial experimental analysis is carried out on a 4% cambered plate at $Re = 6 \times 10^4$. The obtained readings were compared with the findings reported by Pelletier and Mueller [1] along with the numerical findings obtained using ANSYS FLUENT (v 18.1) under the same conditions. The mean lift and drag coefficients which are calculated numerically (using Ansys Fluent) and experimentally at different angles of attack (0° to 14° in steps of 2°) are presented in Fig. 4.8 along with the findings reported by Pelletier and Mueller [1]. From the experimental findings, it is observed that the overall error in mean lift and drag coefficients is about 6% at lower angles of attack ($\theta_m \leq 8°$) and 9.15% at the higher angle of attack ($8° \leq \theta_m \leq 14°$) when compared with the findings reported by Pelletier and Mueller[1]. But an overall error of about 9.75% is observed between the present numerical and experimental findings in almost all of the angles of attack.

4.3 Results

4.3.1 Aerodynamic characteristics of biomimetic wing

To investigate the aerodynamic characteristics of the biomimetic wing, the numerical study is carried out by varying the angles of attack from -8° to 48° with an increment of 4°. The variation in mean lift and drag coefficients of biomimetic wing with respect to the angle of attack at different Reynolds numbers ranging from 2.5×10^4 to 1×10^5 are

presented in Fig. 4.9.

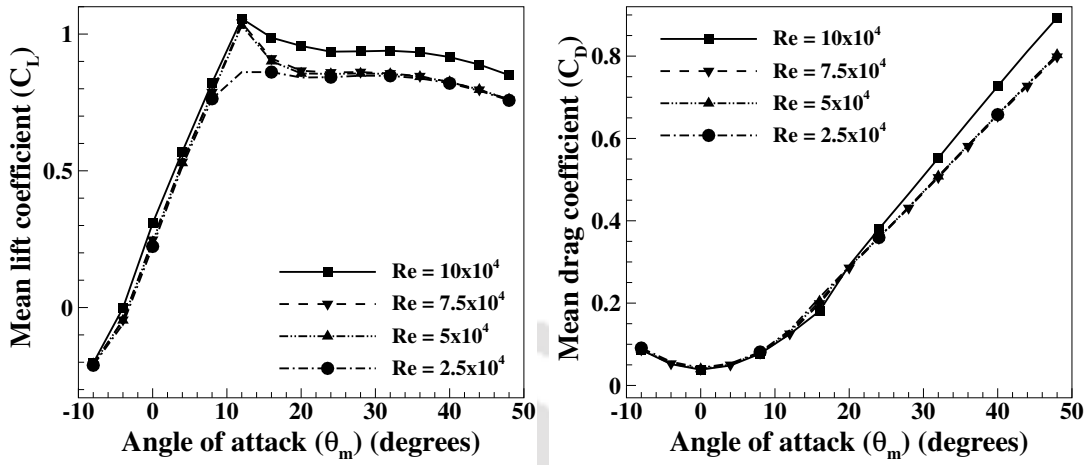

(a) Lift coefficient (b) Drag coefficient

Figure 4.9: Numerical findings of variation in lift and drag coefficients of biomimetic wing with respect to angle of attack at different Re (2.5×10^4 to 10×10^4)

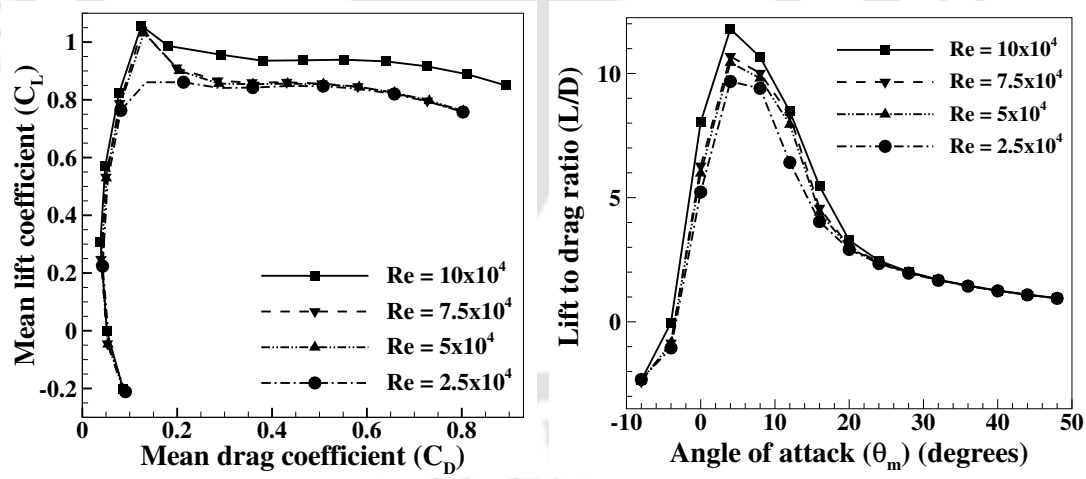

(a) Drag polars (b) Lift to drag ratio

Figure 4.10: Numerical findings of variation in drag polars and lift to drag ratio of biomimetic wing with respect to angle of attack at different Re (2.5×10^4 to 10×10^4)

A slight variation in the lift curve slope is observed with the increase in Reynolds number which indicates that the biomimetic wing is almost independent of the Re regime (from 2.5×10^4 to 1×10^5). Since the flow is fully attached from $\theta_m = 0°$ to $12°$ (can be seen from Fig. 4.17(b)), a sharp rise in the lift curve at $0° \leq \theta_m \leq 12°$ is observed in Fig. 4.9(a). From Fig. 4.9(b), it seems the drag coefficient is less affected with the increase in

Re since C_d slightly decreases with an increase in Re. From Fig. 4.10(a), it is observed that the drag polars of the wing are relatively constant (especially at $Re = 2\times10^4$) along the span at $2.5 \times 10^4 \leq Re \leq 10 \times 10^4$ indicates the existence of two-dimensional flow. Except at $Re = 2 \times 10^4$, a sudden drop in the lift coefficient is observed with a slight increase in drag when θ_m exceeds the stall angle.

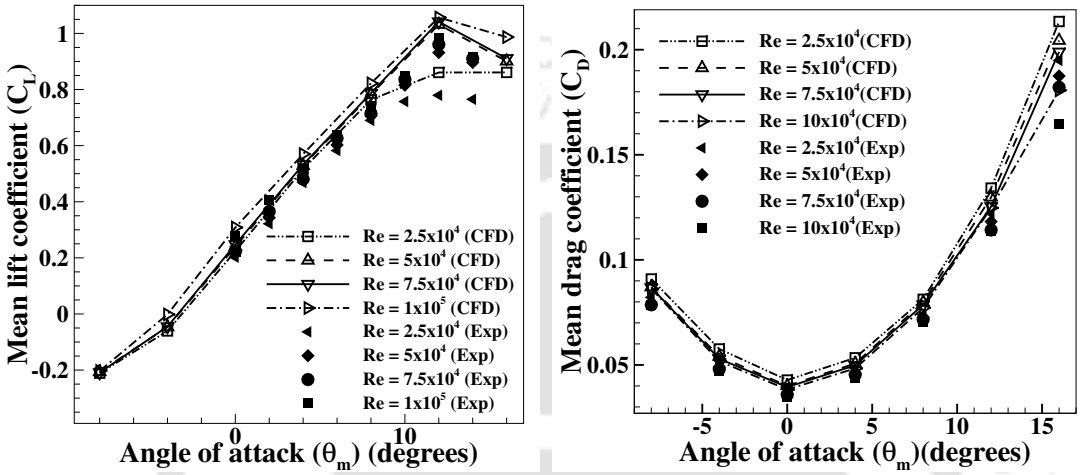

(a) Lift coefficient (b) Drag coefficient

Figure 4.11: Comparison lift and drag coefficients of biomimetic wing with respect to angle of attack at different Re (2.5×10^4 to 10×10^4)

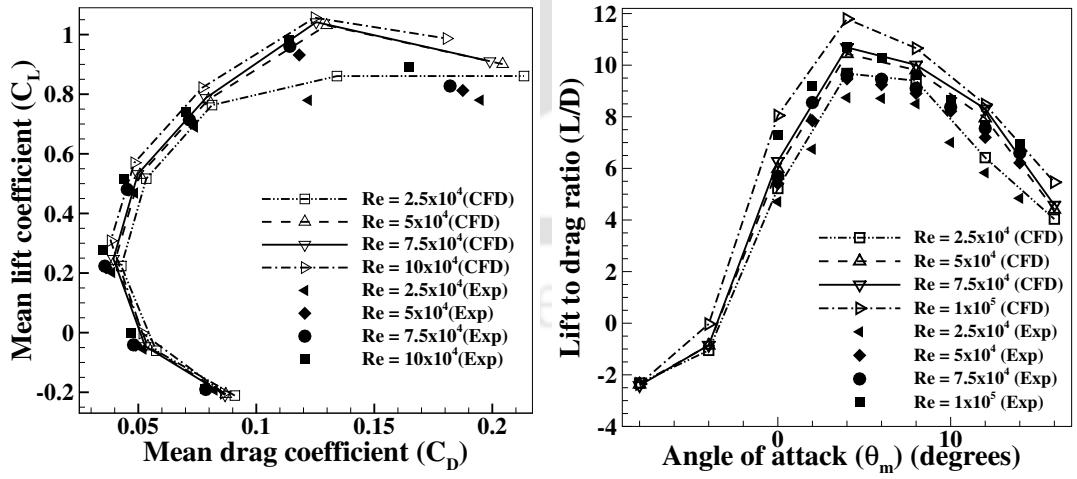

(a) Drag polars (b) Lift to drag ratio

Figure 4.12: Comparison of drag polars and lift to drag ratio of biomimetic wing with respect to angle of attack at different Re (2.5×10^4 to 10×10^4)

From the flow field investigations, it was found that the lift coefficient is affected by the formation of the separation bubble over the wing surface (as shown in Fig.4.20(a) and

4.20(b)) at $5 \times 10^4 \leq Re \leq 10 \times 10^4$ when the angle of attack increases beyond the stall angle. This drop in the lift coefficient is also noticed in the quantitative analysis of the experimental investigations as shown in Fig.4.11(a) and 4.12(a) which further confirms that the formation of separation bubble over the wing surface has adverse effects on the lift generation of the wing when the mean angle of attack exceeds stall angle, with an exception in the regime where $Re = 2 \times 10^4$.

It seems that the separation bubble which was formed over the wing surface beyond 12° at $Re = 2 \times 10^4$ is not large enough to influence the lift coefficient as that of at $5 \times 10^4 \leq Re \leq 10 \times 10^4$. Still, a dramatic increase in the drag coefficient is observed when $\theta_m \geq 18°$ possibly due to flow separation. Bastedo and Mueller [123] reported that the decrease in the slope of the lift curve is usually associated with longer separation bubbles which further strengthens the current findings. From Fig. 4.10(b) it is observed that, the lift to drag ratio (L/D) also followed the same trend as that of lift coefficient. But the maximum L/D ratio was found at $\theta_m = 4°$ (see Fig. 4.10(b) and Fig. 4.12(b)) and decreased with further increase in the angle of attack due to the drastic increase in the viscous drag than that of lift. From this quantitative analysis of the current study, the stall is observed around $\theta_m = 12°$ for the biomimetic wing in the chord Re regime of 2.5×10^4 to 1×10^5. It is quite natural to have lower stall angles for the wings of low aspect ratios (AS $\leq$ 2). As per the findings reported by Gabriel et al [107], higher stall angles can be achieved at high aspect ratio wings. To further verify the numerical findings, the wind tunnel experiments are performed from 0° to 14° in steps of 2^0 at different Re; the obtained results are presented in Fig. 4.11 and Fig. 4.12. A good agreement between both numerical and experimental findings is observed. At lower angles of attack, a deviation (6% - 9.5%) between the numerical and experimental values of the drag coefficient is observed since the values are close to zero. At higher angles of attack, the error is less than 6% since the lift and drag coefficient values are higher due to the involvement of large aerodynamic forces. With the increase in the Re, a decrease in the deviation between the numerical and experimental findings is also observed. From the experiments, the stall is found to be around 12° for all Re which also supports the numerical findings and the maximum lift coefficient is observed at this point.

4.3.2 Performance comparison

For the comparative assessment of presently modelled biomimetic wing, conventionally opted rectangular and elliptical wing planforms were chosen and modelled using the same Bergey BW-3 airfoil. Thereafter, the numerical investigation is carried out on all three wings at $Re = 5 \times 10^4$ and the obtained findings are presented in Fig. 4.13 and Fig.

4.14.

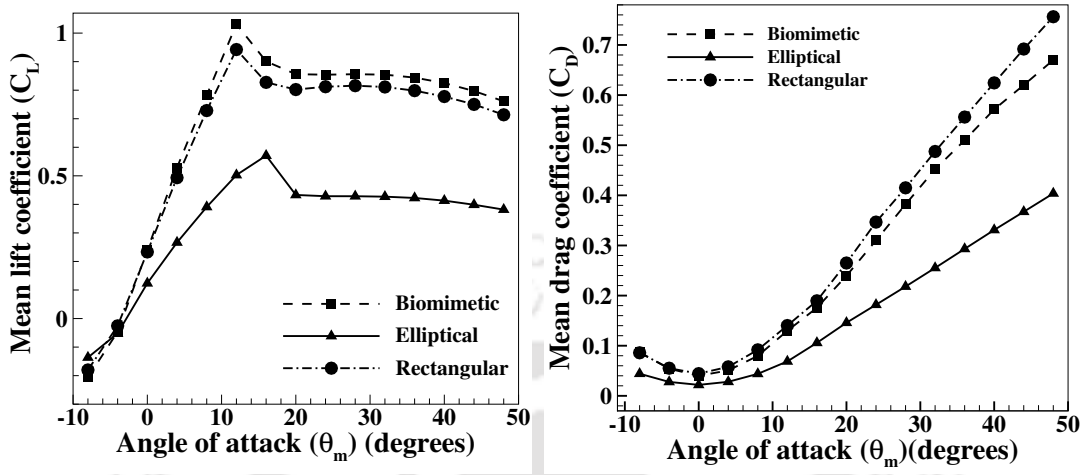

(a) Lift coefficient (b) Drag coefficient

Figure 4.13: Numerical findings of lift and drag coefficients of different wings with respect to angle of attack at $Re = 5 \times 10^4$

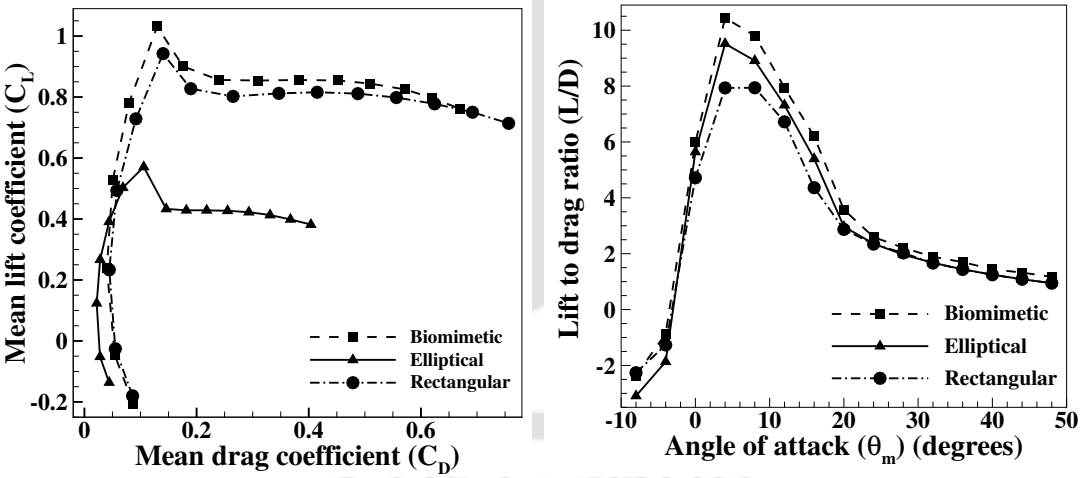

(a) Drag polars (b) Lift to drag ratio

Figure 4.14: Numerical investigation of performance comparison of different wings with respect to angle of attack at $Re = 5 \times 10^4$

A positive lift coefficient is observed even at 0° due to the presence of highly cambered airfoil at different sections of the wings. It is observed that the highest lift coefficient at $\theta_m = 12°$ (from Fig. 4.13(a)) as well as the maximum L/D ratio at $\theta_m = 4°$ (From Fig. 4.14(b)) are found in biomimetic wing than that of other wings under same conditions. This is due to the change in the shape of the wing along the span which has a high impact on its effective angle of attack with respect to the incoming flow.

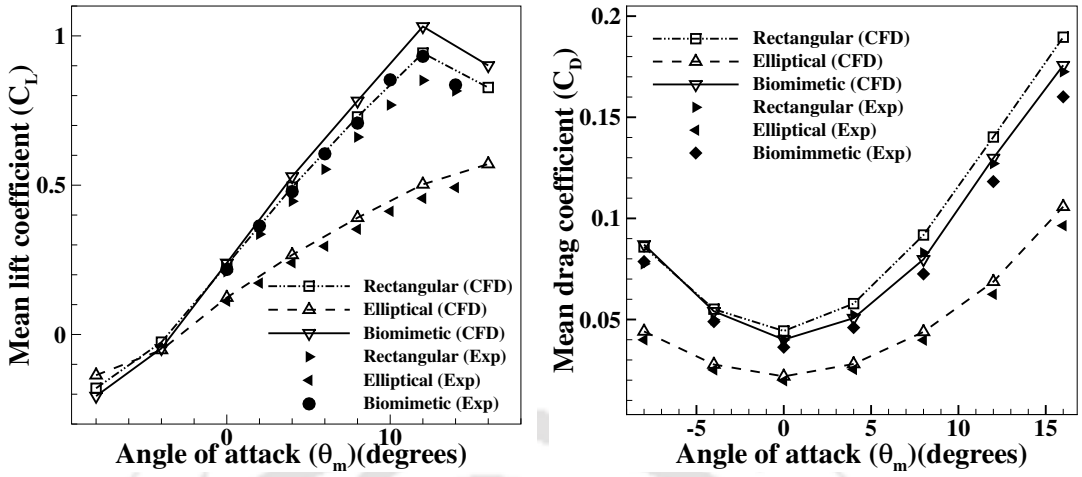

(a) Lift coefficient (b) Drag coefficient

Figure 4.15: Comparison of lift and drag coefficients of different wings with respect to angle of attack at $Re = 5 \times 10^4$

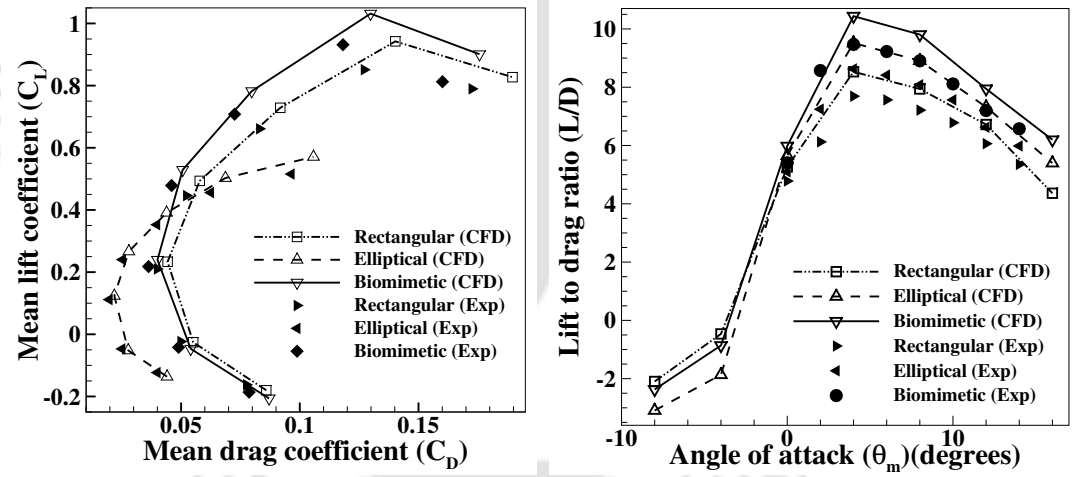

(a) Drag polars (b) Lift to drag ratio

Figure 4.16: Comparison of drag polars and lift to drag ratio of different wings with respect to angle of attack at $Re = 5 \times 10^4$

For rectangular and biomimetic wings, lift increases till 12°, and then stall is noticed. For the elliptical wing, the stall occurs at 16°. The lift coefficient decreases (beyond stall angle) with further increase in the angle of attack due to the presence of viscous drag. From Fig. 4.13(a), it is observed that the elliptical wing offers the lowest lift coefficient than that of the other wings. It seems the interaction between the separation bubble which was formed over the surface of the elliptical wing and the tip vortex has adverse effects on the lift force generation of the wing. It is also observed that the L/D

ratio of the elliptical wing is greater than that of the rectangular wing (see Fig. 4.14(b) and Fig. 4.16(b)) despite of low lift coefficient which indicates that the elliptical wing induces less drag than that of rectangular wing as shown in Fig. 4.13(b). From the present findings, it is observed that the elliptical planform is highly suitable for studies where the drag reduction is primary objective with considerable lift coefficient. From Fig. 4.13(a) and Fig. 4.14(a), it is observed that the drop in the lift coefficient is higher in the case of the rectangular wing. Possibly the presence of the sharp edges in the wing planform influences the flow separation over the wing and affects the overall aerodynamic performance of the wing. On the other hand, the drop in the lift coefficient of the biomimetic wing is less than that of rectangular and elliptical wings since the wing profile varies along the span. This allows to have a variable angle of attack along the span and delays the flow separation process which improves the aerodynamic performance of the wing. Due to this, a 57.9% increase in lift coefficient is observed for the biomimetic wing than that of elliptical wing under same conditions. A 22.4% increase in lift to drag ratio of the biomimetic wing is observed than that of rectangular wing.

The numerical findings of the current study are compared with the experimental findings by performing wind tunnel experiments from 0° to 14° angle of attack with 2° increment at $Re = 5{\times}10^4$. The obtained results are presented in Fig. 4.15 and Fig. 4.16. A good agreement in the overall trend of both numerical and experimental findings is observed. From Fig. 4.15 it is observed that, the lift curve is non-linear which is due to low aspect ratio (AS ≤ 2) of wings. A linear variation in the lift curve can be observed in wings at higher aspect ratios. The experimental work carried out by Gabriel et al [107] has also reported non-linear variation in lift curve at aspect ratio of 0.5 on rectangular and Zimmerman wing planforms at $Re = 1 \times 10^4$. Gabriel et al [107] also reported about point of inflection at aspect ratio of 0.5 for rectangular wing where a slight decrement in lift curve is seen before a sharp rise. There was no point of inflection for other wing planforms. At certain conditions, the boundary layer may separate from the wing surface causing the recirculation of the flow over the suction side of the wing at given angle of attack (θ_m) other than the stall angle (θ_s). Due to this the lift curve at that θ_m slightly drops before reaching θ_s. The α at which the lift curve drops other than θ_s is termed as point of inflection. In such cases, it is hard to locate θ_s, requires the investigation to be carried out over a very wide range of θ_m. In the current findings, there is no point of inflection (indicating that there is no intermediate boundary layer separation up until stall angle) and has a similar trend with the findings reported by Gabriel et al [107].

4.3.3 Flow field analysis

4.3.3.1 Pre-stall events

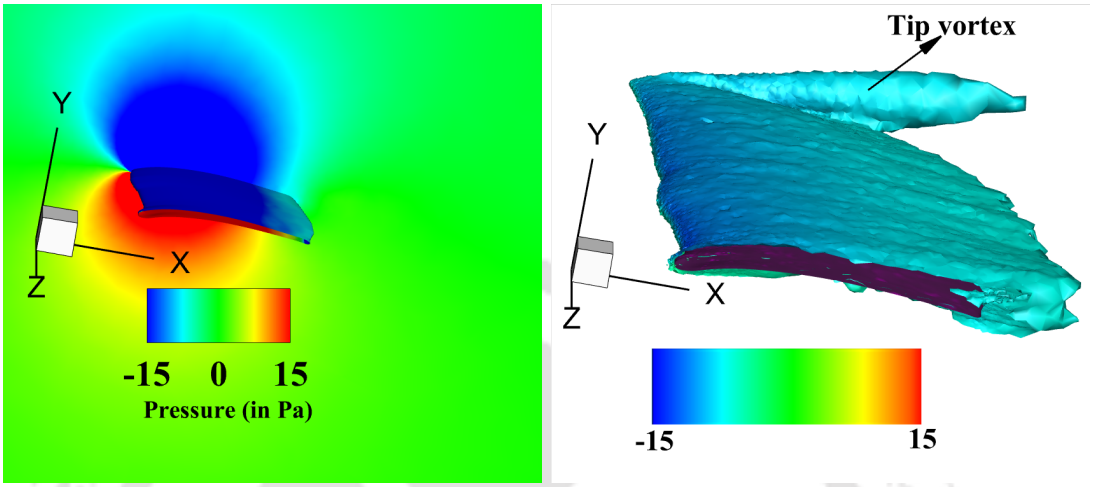

(a) Pressure contour (b) Iso-surface of the Q-criterion at Q = 100

Figure 4.17: Flow over the biomimetic wing at $\theta_m = 12°$ and $Re = 5 \times 10^4$

To further understand the reasons behind the variation in aerodynamic characteristics of the biomimetic wing, a qualitative analysis is carried out by analysing the flow around the wing at $Re = 5{\times}10^4$. The overall flow field investigations are sub divided into two categories: one is pre-stall event and the other is post stall event. The development of the flow structure over the biomimetic wing when $\theta_m \leq 12°$ is presented in Fig. 4.17 to Fig. 4.18. From pressure contour of Fig. 4.17(a), a clear difference in the pressure distribution over the suction side and the pressure side of the wing is observed. The flow over the wing is analysed by calculating the iso-surface of vorticity magnitude at a value of 100 and flooded with pressure with a range of -15 Pa to 15 Pa, presented in Fig. 4.17(b). It is observed that the flow structure is non-uniform along the span; most of the wing surface is covered with the turbulent boundary layer. The flow over the wing surface is fully attached and there is no involvement of vortical structures during the development of the flow up to stall angle ($\theta_m = 12°$). The shedding of tip vortices in the wake region is observed as the flow past the wing surface. The pressure coefficient of the biomimetic wing is calculated at a spanwise position (y/s) of 0.3 and presented in Fig. 4.18. From Fig. 4.18(a) and 4.18(b), a non-linear variation in the pressure coefficient is observed over the wing surface. At a given spanwise location, the suction over the suction side of the wing increases along the chord with respect to increase in the angle of attack up to stall angle ($\theta_m = 12°$). The suction is seen to be more at the root of the wing in comparison with the wingtip (from Fig. 4.17(b)) which is why a non-linear

variation in the lift is observed over the wing surface (as shown in Fig. 4.9(a)). From the structural point of view, it can be seen that more load is acting at the wing root (fixed end) than that at the wingtip (free end) which provides more stability during flight.

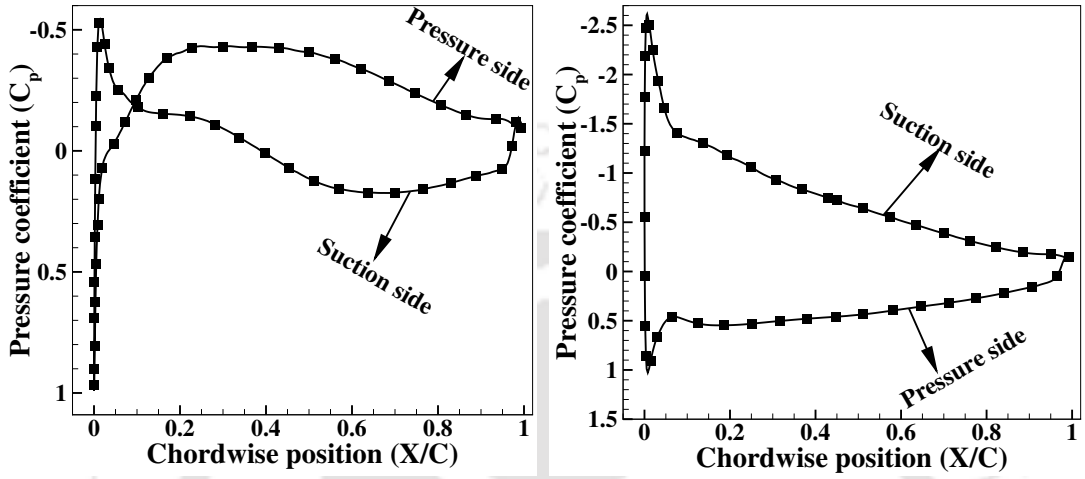

(a) Pressure coefficient at $\theta_m = 0°$ (b) Pressure coefficient at $\theta_m = 12°$

Figure 4.18: Variation of pressure coefficient of biomimetic wing at $Re = 5 \times 10^4$

At lower angles of attack ($\theta_m \leq 4°$), the pressure decreases over the pressure side of the wing along the chord and eventually forms negative pressure (as shown in Fig. 4.18(a)). This negative pressure over the pressure side creates negative suction which opposes the suction created over the suction side. Due to this, the lower values of instantaneous lift coefficient is observed at lower angles of attack.

4.3.3.2 Post stall events

The behaviour of the flow over the biomimetic wing when the mean angle of attack exceeds stall angle is presented from Fig. 4.19 to 4.21. From Fig. 4.19(a) and 4.19(b), only a slight variation is observed in the suction of the suction side of the wing along the chord. At $\theta_m = 48°$, there is almost no variation between the suction at the wing root and the suction at the wing tip. This indicates the formation of a thick separation bubble which covers the major portion of the wing surface and convects over the suction side of the wing. As the angle of attack increases beyond stall angle, the flow over the suction side of the wing separates at the leading edge and forms large separation bubbles as shown in Fig. 4.20(a) and 4.20(b). From Fig 4.20(a), it is observed that the flow separation for $\theta_m = 18°$ occurs approximately at quarter chord region. However, at $\theta_m = 48°$ as seen from Fig. 4.20(b), the flow separation happens at the leading edge with no sign of reattachment. Therefore the separation point moves towards the leading edge

as the angle of attack exceeds 12°. It is observed that the separated flow forms multiple stall vortices over the suction side of the wing due to which the drop in instantaneous values of lift coefficient is observed in Fig 4.9(a) as $\theta_m \geq 12°$.

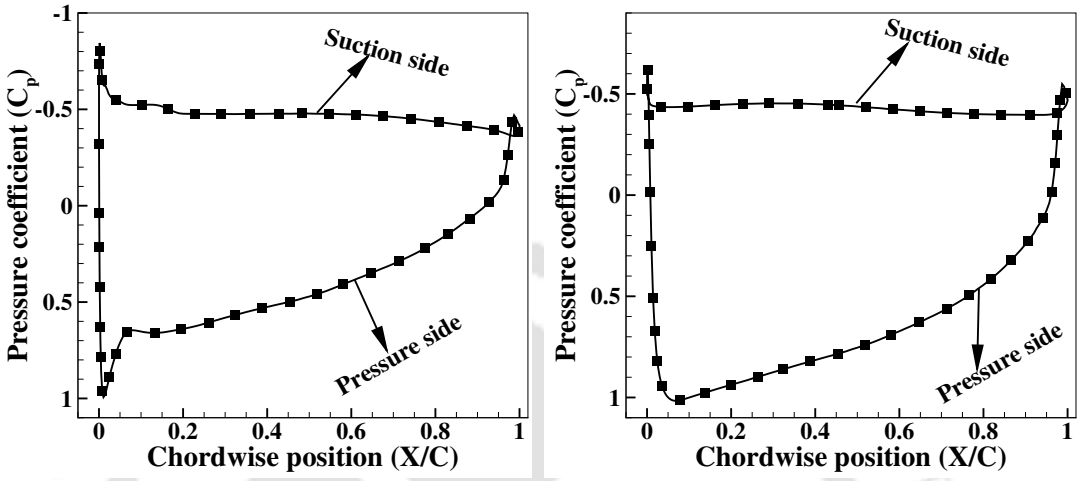

(a) Pressure coefficient at $\theta_m = 24°$ (b) Pressure coefficient at $\theta_m = 48°$

Figure 4.19: Variation of pressure coefficient of biomimetic wing at $Re = 5 \times 10^4$ with respect to the angle of attack

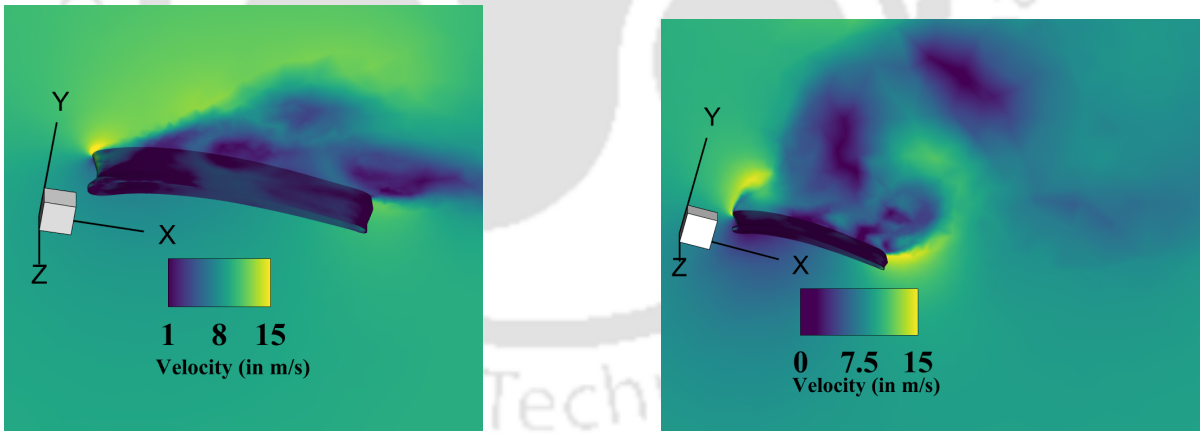

(a) Velocity contour at $\theta_m = 18°$ (b) Velocity contour at $\theta_m = 48°$

Figure 4.20: Contours of velocity magnitude of biomimetic wing at $Re = 5 \times 10^4$ with respect to the angle of attack

From Fig. 4.20(a) and 4.20(b), small scale vortices are observed within the large stall vortex due to the recirculation of the flow over suction side of the wing surface. This indicates strong suction in the core of the stall vortex and the strength of this vortex increases with increase in angle of attack which has adverse effects on the aerodynamic performance of the wing when $\theta_m \geq 12°$. As the flow past the wing, these vortices sheds

into the wake as alternating vortices as shown in the Fig. 4.21(b). The behaviour of the flow over the wing surface beyond the stall angles can also be observed from vorticity contours of Fig. 4.21(a). The spanwise and chordwise variation of the flow is non uniform and the flow is developed in the form of vortical structures due to recirculation over the suction side of the wing. From the flow field investigations, it is observed that some part of the flow is partially attached to the wing surface upto quarter chord in the region $12° \leq \theta_m \leq 18°$ which is why a gradual increase in the mean drag coefficient is observed in Fig. 4.9(b) As $\theta_m \geq 24°$, the flow separation over the wing surface dramatically increases the mean drag coefficient which can also be observed in Fig 4.13(b).

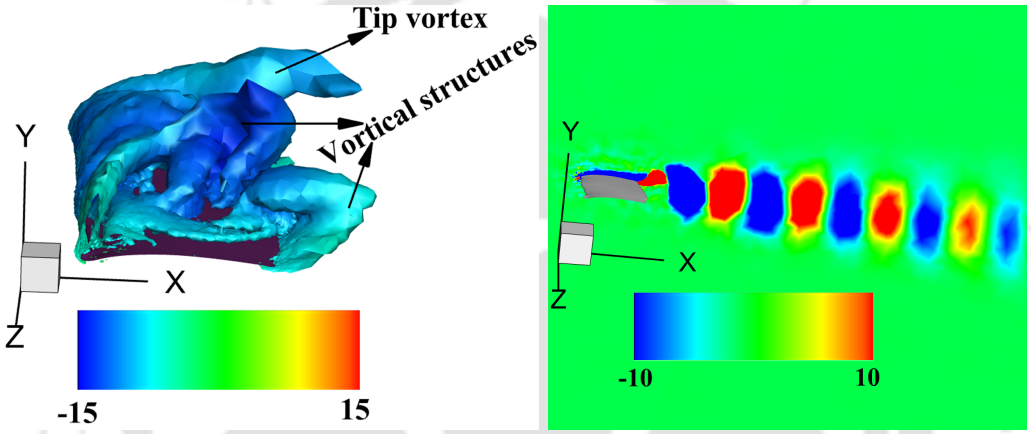

(a) Iso-surface of the Q-criterion at Q = 100 (b) Wake region

Figure 4.21: Flow over the biomimetic wing at $\theta_m = 48°$ and $Re = 5 \times 10^4$

4.4 Summary and conclusions

A biomimetic wing, inspired from Passer Domesticus, is successfully designed using a thin and highly cambered Bergey BW-3 airfoil as a wing cross section. The numerical and experimental studies are carried out to investigate the aerodynamic characteristics of the biomimetic wing at low Reynolds numbers ranging from 2.5 $\times 10^4$ to 1 $\times 10^5$. A good agreement between numerical and experimental findings is observed. Since the wing's aspect ratio is small (AS $\leq$ 2), stall is observed at 12°. Note that higher stall angles can be achieved at high aspect ratios [1]. A slight drop in lift coefficient is observed in the regime 5 $\times 10^4 \leq Re \leq 1 \times 10^5$ due to the adverse effects of the separation bubble which was formed over the surface of the wing when the mean angle of attack exceeds the stall angle. However, at $Re = 2.5 \times 10^4$, the slope of the lift curve is almost constant which indicates that the separation bubble is not strong enough to influence the lift coefficient in this regime but a dramatic increase in the drag coefficient is observed when $\theta_m \geq 18°$.

In order to compare the aerodynamic performance of the biomimetic wing, commercially opted wing planforms namely rectangular and elliptical wings are designed using the same dimensions and cross section and the investigations were carried out at $Re = 5\times10^4$. It is observed that the rectangular wing offers the highest drag compared to that of other wings due to the presence of sharp edges in the wing planform which affects the overall lift to drag ratio (L/D) of the wing. But the elliptical wing offers the lowest drag coefficient and the lowest lift coefficient compared to that of the other wings due to the interaction between the separation bubble and the tip vortex which can be highly suitable for the studies where the drag reduction is the primary objective. On the other hand, the highest lift coefficient is observed in the biomimetic wing with a considerable amount of drag. In overall, a highest of 57.9% increase in lift coefficient is observed in the biomimetic wing compared to that of the elliptical wing at stall angle with $Re = 5 \times10^4$. Also, 22.4% increase in lift to drag ratio of the biomimetic wing is observed compared to that of the rectangular wing. The better performance of the biomimetic wing is due to the change in the shape of the wing along the span which has a strong influence over its effective angle of attack with respect to the incoming flow.

The overall flow structure of the biomimetic wing is categorised into two main phases: one is pre stall event where the flow is fully attached and no vortical structure is formed over the wing surface. The other one is the post stall event where the flow is no longer attached and creates multiple stall vortices over the wing surface due to the recirculation of the flow. In the pre stall event, it is observed that the flow is fully attached up to 12° angle of attack and a non-linear variation of suction is observed along the span. It is also observed that the suction is more at the wing root (fixed end) than that of the wingtip (free end) which allows a good stability during flight. In the post-stall event, it is observed that the flow is partially attached to the wing surface up to the mid chord in the region where $12^\circ \leq \theta_m \leq 18^\circ$ due to which a gradual increase in the drag coefficient is observed. It is also observed that the flow separation point moves towards the leading edge as the angle of attack increases beyond 12°. As $\theta_m \geq 24^\circ$, the flow is fully separated and a rapid rise in the mean drag coefficient is observed with respect to increase in the angle of attack. In overall, the present study recommends this biomimetic wing inspired from Passer Domesticus for better aerodynamic performance at low Re in combination with low aspect ratios while designing wings for aerial vehicles by maintaining $\theta_m \leq 24^\circ$.

भारतीय प्रौद्योगिकी संस्थान गुवाहाटी
Indian Institute of Technology Guwahati

Chapter 5

Low Re Flow Investigation of the Biomimetic Wing Undergoing Pitching Motion

In this chapter, the aerodynamic characteristics of the biomimetic wing subjected to pitching motion are investigated using FVM based three dimensional time dependent incompressible Navier-Stokes (N-S) equations at low *Re* regime. The influence of parameters like amplitude of oscillation, location of pitching axis and mean angle of attack on instantaneous force coefficients are analysed. Further, the flow field around the wing is also explored. The study reveals that the investigated parameters has a remarkable influence on the thrust force generation and the propulsion efficiency of the wing. Therefore, the optimal aerodynamic performance of the biomimetic wing demands proper selection of operating conditions which can be achieved by analysing aforementioned parameters.

5.1 Introduction

The process of unsteady flow separation was first identified on the rotor blades of helicopters when rotating at high speeds. This phenomenon of flow separation is named as dynamic stall. Due to this, the conventional aerodynamics unable to estimate the overall performance of the high speed helicopters. To address this, extensive amount of research was carried out on the blades of helicopters, turbines, compressors and also on aircrafts which have high manoeuvrability.

To model and characterise the formation of dynamic stall vortex, numerous computational and experimental studies are carried out on different types of airfoils undergoing harmonic oscillations at different conditions. Jones et al [31] investigated the Knoller-

Betz effect by simulating the flow over the NACA 0012 airfoil with Reynolds number (Re) ranging from 5×10^2 to 5×10^4 operated at a frequency range of 5-60 Hz. Their observations suggest that, the airfoil is able to generate thrust when Strouhal Number (St) is greater than 1. Koochesfahani [28] experimentally investigated the wake behind the trailing edge of NACA 0012 airfoil operated at $Re = 12 \times 10^3$ and 0.5-6 Hz. According to Koochesfahani [28], the thrust is observed at reduced frequency (k_f) of 1 and also reported that the flow separation over an airfoil surface and the wake behind the trailing edge have high influence on thrust generation of oscillating airfoils. Ramamurthi and Sandberg [3] numerically studied the flow past NACA 0012 airfoil between 1-8 Hz and observed positive thrust when $k_f \geq 4$. The NACA 0012 airfoil has been shown to develop positive thrust at different conditions. Freymuth [30] experimentally investigated the aerodynamic performance of NACA 0015 airfoil subjected to pitching and plunging separately. It was reported that, a thrust generating vortex street is observed at $Re = 5.2 \times 10^3$ with $k_f = 2.7$ having non-dimensional plunge amplitude of 0.2 and positioned at 5° angle of attack during plunging. It was also reported that NACA 0015 airfoil produces positive thrust at $Re = 12 \times 10^3$, $k_f = 2.9$ at 20° pitching amplitude and positioned at 5° angle of attack while oscillating at quarter chord length. Picard et al [124] investigated the energy extraction of oscillating NACA 0020 airfoil at $Re = 5 \times 10^5$ with large plunge amplitudes and observed that a propulsive efficiency of 44% can be achieved at large plunge amplitudes, approximately 15 times the chord length. The numerical investigations performed by Taira and Colonius [125] on low aspect ratio plates in translation reveals that the tip vortices stabilize the separated flow. It was also reported that the stability of the wake region can be characterised over a wide range of aspect ratio and the angle of attack. The findings of Granlund et al [126] and Jantzen et al [127] on high aspect ratio plates performing pitching motion, reveals that the tip effects have high influence on the formation and the evolution of leading edge vortex. As evident from above discussion, depending on the design constraints, the operating conditions can be varied and best possible performance can be investigated.

Most of the aerial vehicles perform either the pitch up or pitch down motion to improve the aerodynamic performance of the aircraft in gusty conditions. In order to analyse such performance, most of the studies used two dimensional wing cross sections and a very little attention is devoted towards actual three dimensional wings. Out of which, most of the studies used commercial wing planforms like rectangular or elliptical shapes to estimate the development of flow during pitching motion. The findings reported in this chapter attempts to address aforementioned shortcomings from the literature. This chapter presents the numerical investigation on the aerodynamic characteristics of the biomimetic wing subjected to pitching motion with respect to the incoming viscous

flow. The modelling of the biomimetic wing is already presented in section 4.2.1 of Chapter-4. The findings presented in this chapter aims to understand the influence of parameters like amplitude of oscillation, location of pitching axis and mean angle of attack on the instantaneous force coefficients and the flow around the wing.

5.2 Method

5.2.1 Problem definition

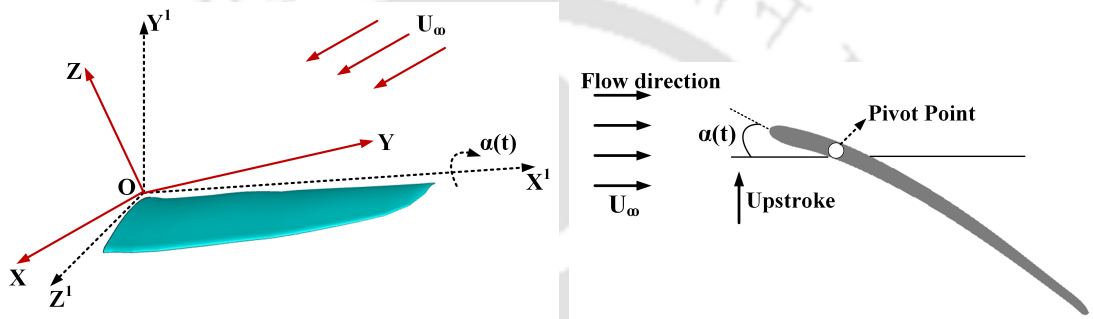

(a) Pitching wing (b) Left side view

Figure 5.1: Schematic view of biomimetic wing subjected to pitching motion

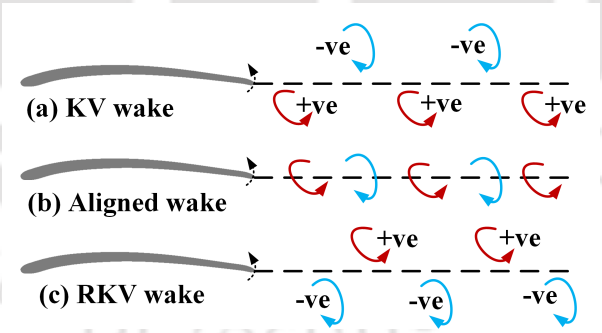

Figure 5.2: Schematic view of wake patterns observed in the wake region of the wing

The modelling of the biomimetic wing is already discussed in section 4.2.1 of Chapter-4. In the current numerical investigations, the biomimetic wing will be subjected to a pitching motion ($\alpha(t)$) with respect incoming incompressible viscous flow having free stream velocity U_∞ as shown in Fig. 5.1. In order to describe the three dimensional pitching motion of the biomimetic wing, two coordinate systems with same origin (fixed at the leading edge of the wing root) are considered. The inertial coordinate system OXYZ is fixed on the ground, in which the OXY plane is parallel to the horizontal plane and the OX axis is directed towards the wing's trailing edge. The OY axis is opposite

to the direction of the gravity and the direction of the OZ axis can be visualize using right hand thumb rule. The coordinate system $OX^1Y^1Z^1$ is located on the wing. The OX^1 and the OZ^1 axes are along the spanwise and the chordwise directions of the wing respectively. The direction of the OY^1 axis can be imagined using right hand thumb rule. The pitching axis is fixed at the quarter chord location from the leading edge (see Fig. 5.1(b)). A schematic representation of different types of wake structures encountered during the course of this study are presented in Fig. 5.2. The KV wake and RKV wake in Fig. 5.2 stands for the Karman Vortex wake and the Reverse Karman Vortex wake.

The pitching motion of the wing is defined in Eq. 5.1.

$$\alpha(t) = \theta_m + \alpha_p Sin(2\pi f t) \tag{5.1}$$

where θ_m is the mean angle of attack, α_p is the amplitude of oscillation and f is the frequency of oscillation.

5.2.2 Propulsion Model

The propulsive performance of the oscillating wing is characterised by two non- dimensional parameters, namely the time averaged thrust coefficient (C_t) and the propulsion efficiency (η_p). The time averaged thrust coefficient (C_t) is defined as follows:

$$C_t = \frac{\frac{1}{T}\int_0^T P_x(t)\mathrm{d}t}{\frac{1}{2}\rho A U_\infty^2} \tag{5.2}$$

The propulsion efficiency (η_p) is the ratio of time averaged thrust coefficient (C_t) and time averaged power coefficient (C_p). For the computation of C_{pc}, the power (P_i) is defined by Eq. 5.3:

$$P_i = \frac{1}{T}\int_0^T [P_y(t)\frac{\mathrm{dy(t)}}{\mathrm{dt}} + \mathrm{P_x(t)}\frac{\mathrm{dx(t)}}{\mathrm{dt}} + \mathrm{M(t)}\frac{\mathrm{d}\alpha\mathrm{(t)}}{\mathrm{dt}}]\mathrm{d}t \tag{5.3}$$

and the time averaged power coefficient (C_{pc}) is given by Eq. 5.4:

$$C_{pc} = \frac{P_i}{\frac{1}{2}\rho A U_\infty^3} \tag{5.4}$$

Finally, the propulsion efficiency (η_p) is given by Eq. 5.5.

$$\eta_p = \frac{C_t}{C_{pc}} \tag{5.5}$$

where $P_x(t)$ is the instantaneous force in the x direction, $P_y(t)$ is the instantaneous force in y direction, ρ is the density of air, x(t) is the motion in x-direction, y(t) is the motion

in y-direction and M(t) is the pitching moment.

5.2.3 Computational details

5.2.3.1 Domain independence test

The details of wing modelling, meshing of computational domain and the association of boundary conditions are already discussed in the sections 4.2.1 and 4.2.2.1 of Chapter-4 respectively. To oscillate the wing with respect to the incoming flow, an User Defined Function (UDF) is developed using Eq. 5.1. The smoothing and re-meshing methods are also activated with 10 re-mesh intervals to update the mesh after completion of every time step. In order to fix the time step (t^*) for each simulation, an initial time refinement study (ranging from 1×10^{-4} s $\leq t^* \leq 1\times10^{-3}$ s) was carried out.

Table 5.1: Comparison of average drag coefficients (C_D) of biomimetic wing with different domain dimensions pitching at $Re = 5 \times 10^4$, $k_f = 2$, $\theta_m = 0°$ and $\alpha_p = 30°$

Domain	Radius(r_1)	Distance (x_1)	Avg. C_d	Error(%)
Domain 1	25C	50C	-0.0815	–
Domain 2	50C	100C	-0.0813	0.246
Domain 3	75C	150C	-0.0812	0.123

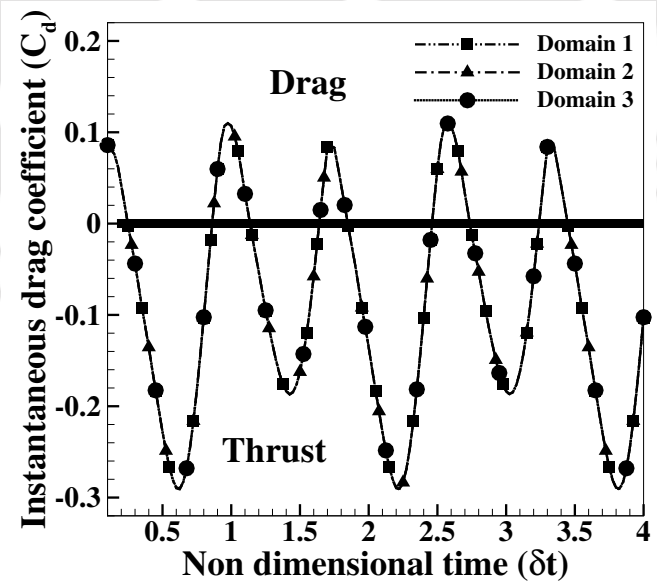

Figure 5.3: Comparison of instantaneous drag coefficients of biomimetic wing pitching at $Re = 5 \times 10^4$, $\theta_m = 0°$, $\alpha_p = 30°$ and $k_f = 2$ with different domain dimensions

It is observed that, when 1×10^{-4} s $\leq t^* \leq 5\times10^{-4}$ s the variation between the instantaneous force coefficients is almost negligible. Therefore, $t^* = 5\times10^{-4}$ s is considered

with 35 iterations in each time step for all the simulations of current chapter. Further, the domain independence test was carried out to verify the variation of the results with respect to the dimensions of the fluid domain when the wing is subjected to pitching motion. The findings obtained with respect to the dimensions of each domain are presented in Table 5.1. The error percentage of Table 5.1 is calculated from the findings of two consecutive domains. Also, the variation in the instantaneous drag coefficient (C_d) of the wing pitching at $\theta_m = 0°$, $\alpha_p = 30°$ and $k_f = 2$ with respect to the domain dimensions are presented in Fig. 5.3. It is observed that the findings are almost invariant with respect to the dimensions of the domain. However, when $k_f \geq 3$, reversed flow is observed at pressure outlet for certain number of time steps for Domain 1 since the outlet boundary is not far enough from the wing's trailing edge. Therefore, in order to minimize the influence of outer boundaries on the flow field around the wing, the dimensions of the Domain 2 are opted for all the simulations where the inlet boundary is at a distance of 50C from the leading edge and the outlet boundary is maintained at 100C from the trailing edge of the wing. No sign of reversed flow is observed at pressure outlet during the course of each simulation.

5.2.3.2 Grid independence

Table 5.2: Comparison of average lift and drag coefficients of biomimetic wing pitching at $Re = 5 \times 10^4$, $\theta_m = 0°$, $\alpha_p = 20°$ and $k_f = 1$ with respect to different grids (Min. OQ refers to minimum orthogonal quality)

Mesh type	Size	Min. OQ	Avg. C_l	Error(%)	Avg. C_d	Error(%)
Grid 1	18.7x10^5	0.182	1.2977	—	0.0305	—
Grid 2	41.3x10^5	0.237	1.2625	2.78	0.0286	6.64
Grid 3	87.4x10^5	0.323	1.2444	1.43	0.0281	1.75

Further, the grid independence test was carried out to examine the sensitivity of results with respect to the size and quality of grid. Towards that end, three grids with different sizes and qualities (shown in Table 5.2) were generated. The numerical simulations are carried out on the biomimetic wing pitching at $\theta_m = 0°$, $\alpha_p = 20°$, $k_f = 1$ and $Re = 5{\times}10^4$. The obtained values of mean lift and drag coefficients with respect to grid size and quality are presented in Table 5.2. The error percentage is calculated using the corresponding values of each grid. The variation of instantaneous lift and drag coefficient with respect to aforementioned grids is presented in Fig.5.4. From Table 5.2 and Fig.5.4, it is observed that the findings obtained using Grid 1 are slightly higher than that of Grid 2 and Grid 3. It is also noticed that the findings of Grid 2 and Grid 3 are almost invariant.

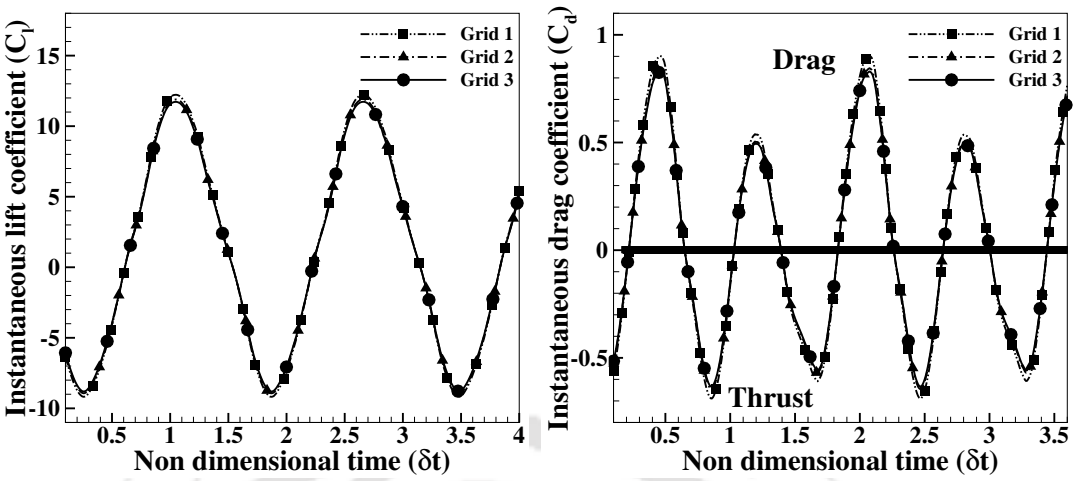

(a) Lift coefficient (b) Drag coefficient

Figure 5.4: Comparison of instantaneous lift and drag coefficients of biomimetic wing pitching at $Re = 5 \times 10^4$, $\theta_m = 0°$, $\alpha_p = 20°$ and $k_f = 1$ with respect to different grids

Table 5.3: Comparison of average thrust force coefficient (Avg. C_t) of NACA 0012 airfoil with different grids pitching at $Re = 1.2 \times 10^4$, $\theta_m = 0°$, $k_f = 10$ and $\alpha_p = 2°$

Mesh type	Size	Min. OQ	Avg. C_t	Error(%)
Grid 1	2.3x10^4	0.293	0.0068	13.33
Grid 2	3.5x10^4	0.446	0.0065	8.34
Grid 3	6.2x10^4	0.495	0.0064	6.67

To further verify the accuracy of the above mentioned grids, the findings reported by Ramamurti and Sandberg [3] are considered as a reference. The results of a typical grid independence test through simulations for 2^0 amplitude of oscillation at $k_f = 10$ for NACA 0012 airfoil at $Re = 1.2 \times 10^4$ are shown in Table 5.3. The error percentage for each grid was computed based on the average thrust coefficient (C_t) obtained and the average C_t reported by Ramamurthi and Sandberg [3] at same conditions. It is observed that the findings of Grid 1 slightly deviates than that of Grid 2 and Grid 3 with respect to the findings reported by Ramamurthi and Sandberg [3]. It is also noticed that the variation between the findings of Grid 2 and Grid 3 are almost negligible. In conclusion to the grid independence, Grid 2 which is computationally less expensive with not much deviation from the findings of Grid 3 is opted for further simulations.

5.2.3.3 Validation

To validate the current numerical approach, different validation studies are carried out. The procedure for mesh generation and the association of boundary conditions are similar

to that of presented in the section 4.2.2.1. For the first validation study, the findings reported by Kurtulus [2] on pitching NACA 0012 airfoil at $\theta_m = 0°$, $\alpha_p = 1°$ and $k_f = 4.3$ are considered.

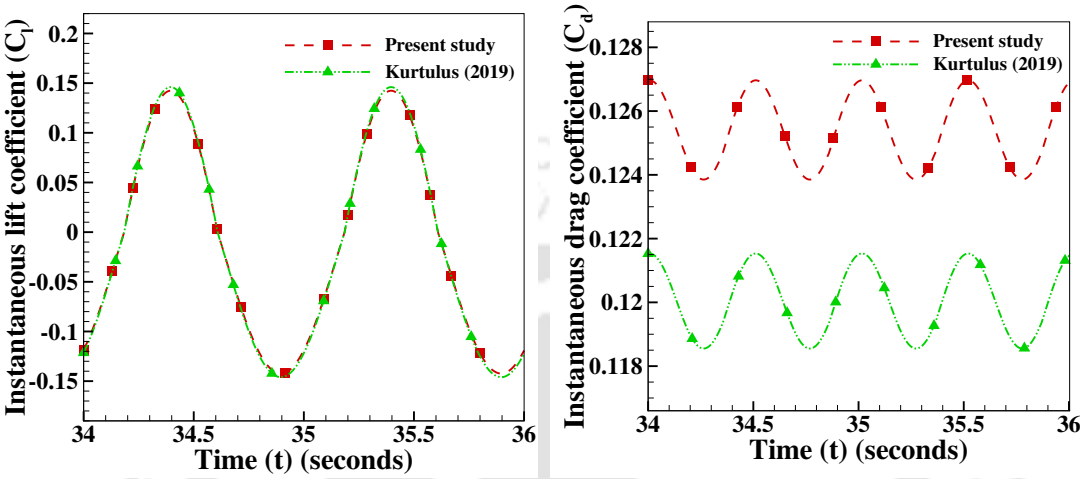

(a) Lift coefficient (b) Drag coefficient

Figure 5.5: Comparison between the findings obtained using current numerical approach and findings reported by Kurtulus [2]

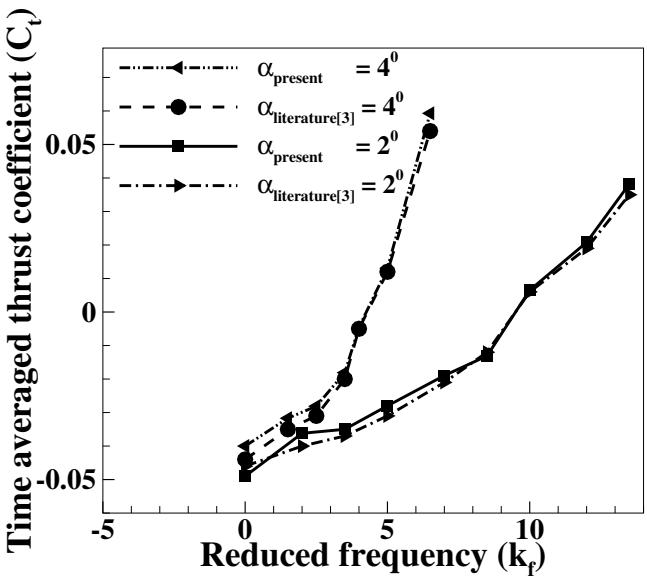

Figure 5.6: Comparison between the findings obtained using current numerical approach and findings reported by Ramamurthi and Sandberg [3]

The instantaneous values of lift coefficient (C_l) and drag coefficients (C_d) are calculated at aforementioned conditions and the obtained findings are presented in Fig. 5.5. It is observed that the findings obtained using current numerical approach has similar trend

as that of the findings reported by Kurtulus [2]. A maximum error of 2.55% is observed in the lift coefficient and a maximum error of 4.47% is observed in the drag coefficient with respect to the findings reported by Kurtulus [2]. For the second validation study, the findings reported by Ramamurthi and Sandberg [3] on pitching NACA 0012 airfoil at $\alpha_p = 2°$ and $\alpha_p = 4°$ over a range of reduced frequencies varying from 0 to 13.5 are considered. The time averaged thrust coefficients (C_t) of NACA 0012 airfoil at different reduced frequencies (k_f) are obtained using present numerical approach and compared with the findings reported by Ramamurthi and Sandberg [3] at the same conditions as shown in Fig.5.6.

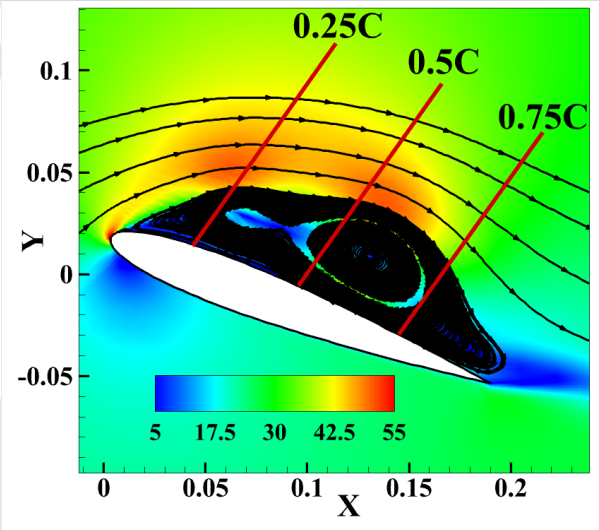

Figure 5.7: Contours of velocity magnitude (V_m) in m/s along with stream lines at 22° upstroke period

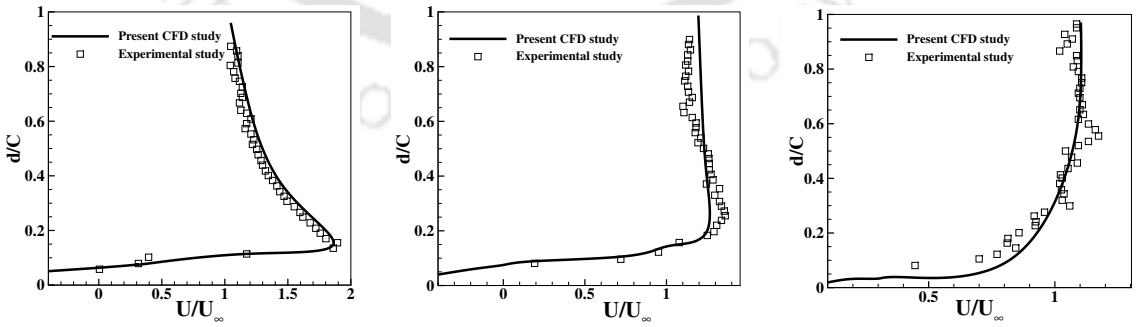

(a) x/C = 0.25 (b) x/C = 0.5 (c) x/C = 0.75

Figure 5.8: Comparison between experimental data and CFD results at 22° upstroke

It is observed that the findings obtained from present numerical approach has encouraging agreement with the findings reported by Ramamurthi and Sandberg [3]. A

maximum error of 9.76% is observed during the calculations of mean thrust coefficient (C_t). The experimental investigations carried out by Wernert et al [128] on pitching NACA 0012 provided the information regarding the near-wall velocity magnitude profiles over the suction side of the airfoil which are used as a benchmark by many researchers to validate their numerical simulations [129, 130, 131]. Therefore, to further validate the current numerical simulations, the experimental investigations carried out by Wernert et al [128] are considered. The Kinematic and operating parameters are: $\alpha_p = 10°$, f = 6.67 Hz and $\theta_m = 15°$, C = 0.2 m, U_∞ = 28m/s with pivot point being located at 0.25C. The obtained velocity field along with the stream lines is presented in Fig. 5.7. It is observed that the flow is no longer attached due to the formation of the vortical structures over the suction side of the airfoil.

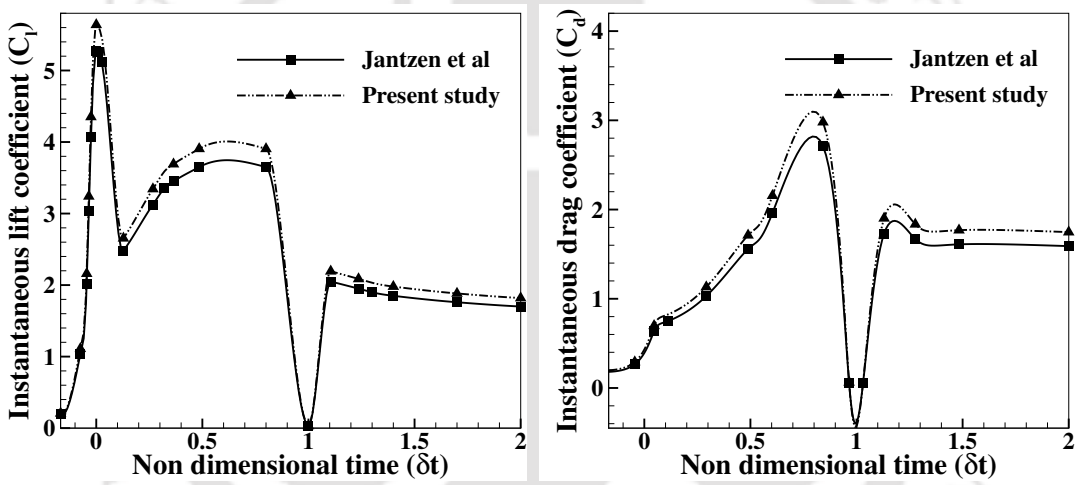

(a) Lift coefficient (b) Drag coefficient

Figure 5.9: Comparison between the findings obtained using current numerical approach and findings reported by Jantzen et al [4]

The velocity profiles during upstroke (with 22^0 angle of attack) of the airfoil at x/C = 0.25, 0.5 and 0.75 are presented in Fig. 5.8 along with the findings reported by Wernert et al [128]. The slight deviation between the present CFD study and the experimental data is due to the complex nature of the flow at 22^0 upstroke angle (as shown in Fig. 5.7). It is observed that overall variation between the findings of current numerical investigation is in good agreement with respect to that of the Wernert et al [128]. Another validation study is carried out by considering the findings reported by Jantzen et al [4] on pitching flat plate of aspect ratio 2 and $k_f = \pi/8$ as a reference. The instantaneous values of lift and drag coefficients of pitching flat plate are obtained and presented in Fig. 5.9 along with the findings reported by Jantzen et at [4]. It is observed that a maximum error of 6.99% is observed in instantaneous lift coefficient and a maximum error of 9.87% is

observed in drag coefficient with respect to the findings of Jantzen et al [4].

From these validation studies, it is noticed that the current numerical approach is efficient to explore the unsteady aerodynamics of the wing subjected to pitching motion.

5.3 Results

From the findings of Chapter-4 we have observed that the biomimetic wing has shown remarkable performance in terms of lift coefficient and lift to drag ratio. When the wing is subjected to motion, the average lift coefficient (C_l) curve is almost symmetric with slight deviation in its sinusoidal nature. Further, the values of C_l increases with respect to increase in the system parameters. Since the wing is performing exceptionally well in terms of lift force coefficient, a dedicated analysis is not presented. We focused on analysing the thrust force coefficient, propulsion efficiency and the parameters affecting the flow around the wing in the subsequent chapters.

5.3.1 Effect of pitch amplitude

To investigate the effect of pitching amplitude (α_p) on the performance of the biomimetic wing subjected to pitching motion, the numerical study is carried out by varying α_p from 10° to 30° in steps of 10°. In this case, the wing is maintained at $\theta_m = 0°$ with the pitching axis being at leading edge.

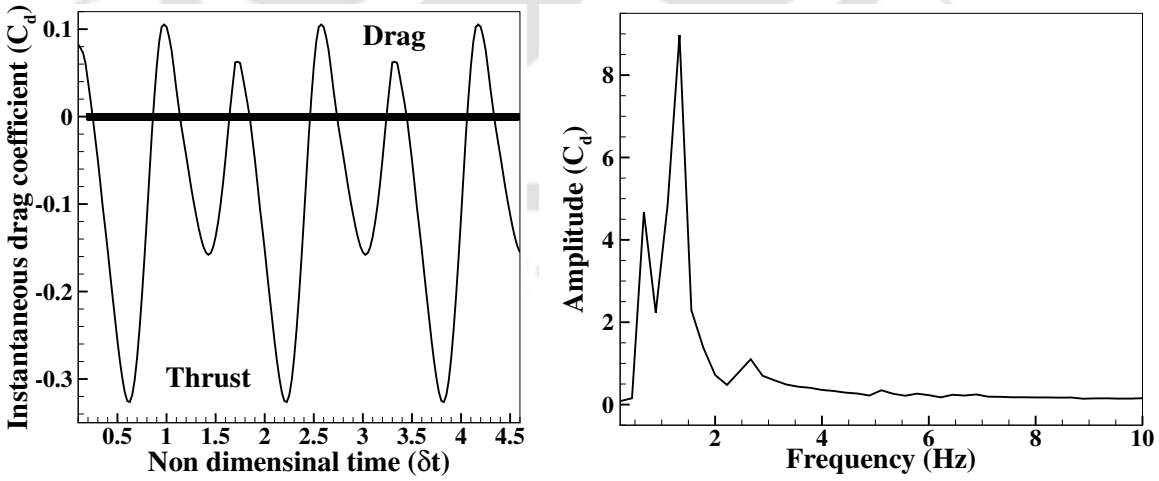

(a) Time domain

(b) Frequency domain

Figure 5.10: Variation of instantaneous drag coefficient of pitching biomimetic wing at $\alpha_p = 30°$, $\theta_m = 0°$

From the preliminary investigations, it is observed that, at lower frequencies (when

$k_f \leq 0.25$), the re circulation of the flow over the wing's surface is so high. Due to this, the wing is unable to overcome the viscous drag offered by the fluid. Therefore the minimum value of reduced frequency (k_f) is considered as 0.5 with an increment of 0.5 up to a maximum value of 3 for almost all of the cases.

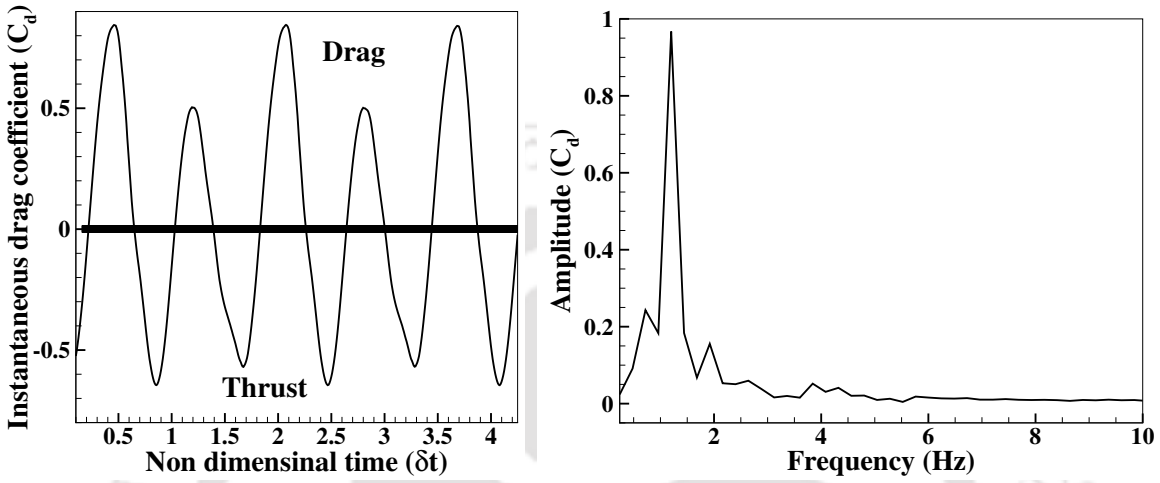

(a) Time domain (b) Frequency domain

Figure 5.11: Variation of instantaneous drag coefficient of pitching biomimetic wing at $\alpha_p = 20°$, $\theta_m = 0°$

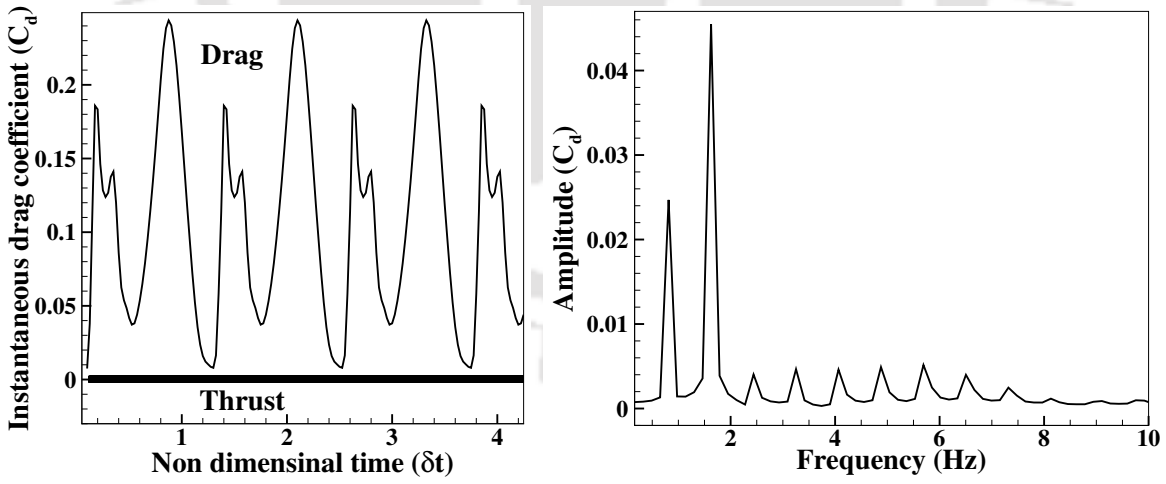

(a) Time domain (b) Frequency domain

Figure 5.12: Variation of instantaneous drag coefficient of pitching biomimetic wing at $\alpha_p = 10°$, $\theta_m = 0°$

The instantaneous values of the drag coefficient (C_d) of biomimetic wing pitching at different α_p are presented from Fig. 5.10 to 5.12. It is observed that the variation in C_d is periodic and has a sinusoidal pattern. A deviation in the sinusoidal pattern of C_d

is observed with decrease in α_p. It is also noticed that, as α_p decreases, the C_d curve rises towards the positive values which indicates an increase in the drag offered by the surrounding fluid. The negative values of C_d curve indicates the thrust force generation of the wing. To further analyse the variation in C_d at different α_p, the amplitude spectrum of C_d is calculated using the Fourier transform algorithm, presented in Fig. 5.10(b), 5.11(b) and 5.12(b).

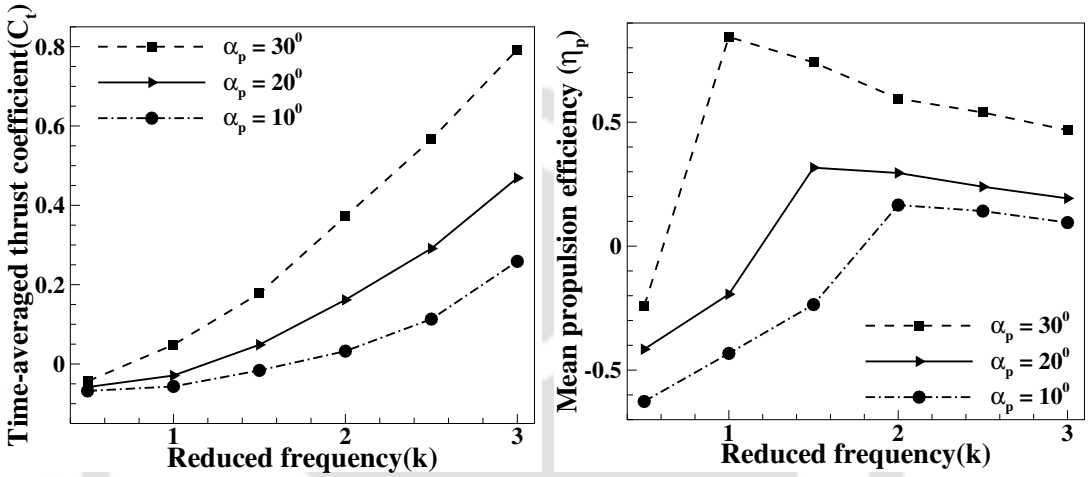

(a) Variation of thrust coefficient (b) Variation of propulsion efficiency

Figure 5.13: Aerodynamic performance of the pitching wing with respect to reduced frequency at different amplitudes of oscillations with $\theta_m = 0°$

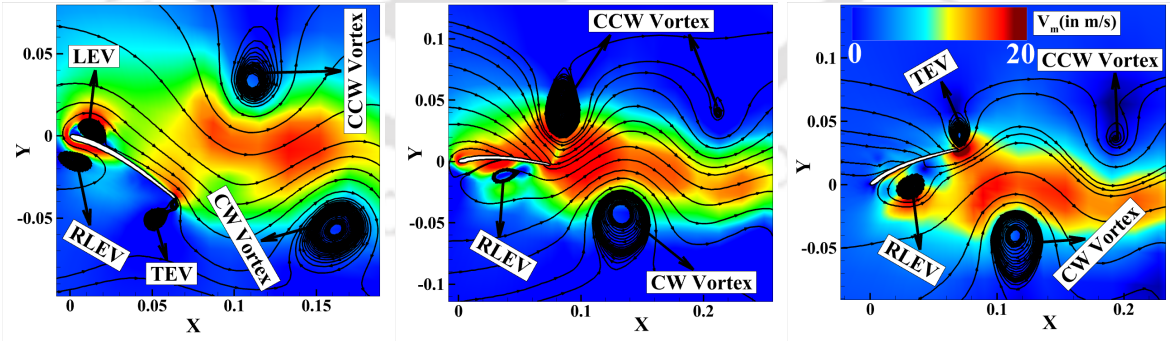

(a) Upstroke (b) Mean position (c) Down stroke

Figure 5.14: Contours of velocity magnitude (V_m) and streamline flow of the wing pitching at $\alpha_p = 30°$, $\theta_m = 0°$ and $k_f = 1$

Multiple peaks with different amplitudes are observed at different α_p. From the flow field investigations, it is observed that these peaks are due to the formation and convection of the vortices over the suction side and pressure side of the wing as shown

from Fig. 5.14 to 5.18. It is also noticed that, the variation in the amplitude of these peaks with respect to α_p indicates the variation in the strength of the corresponding vortex street. This signifies that a denser and higher amplitude spectrum at 30° pitch amplitude indicates higher thrust force generation than that of at $\alpha_p = 20°$ and $\alpha_p = 10°$. To further investigate the influence of α_p on the aerodynamic performance of the biomimetic wing subjected to pitching motion, the variation in mean thrust coefficient (C_t) and propulsion efficiency (η_p) are estimated using Eq. 5.2 to Eq. 5.5. The obtained findings of C_t and η_p at different α_p with respect to the reduced frequency (k_f) are presented in Fig. 5.13. It is observed that, for $\alpha_p = 30°$, the C_t and η_p rises towards the positive values when $k_f \geq 1$. To understand the reasons behind the positive thrust generation at $\alpha_p = 30°$ in combination with $k_f = 1$, the flow field around the wing is investigated and presented in Fig. 5.14.

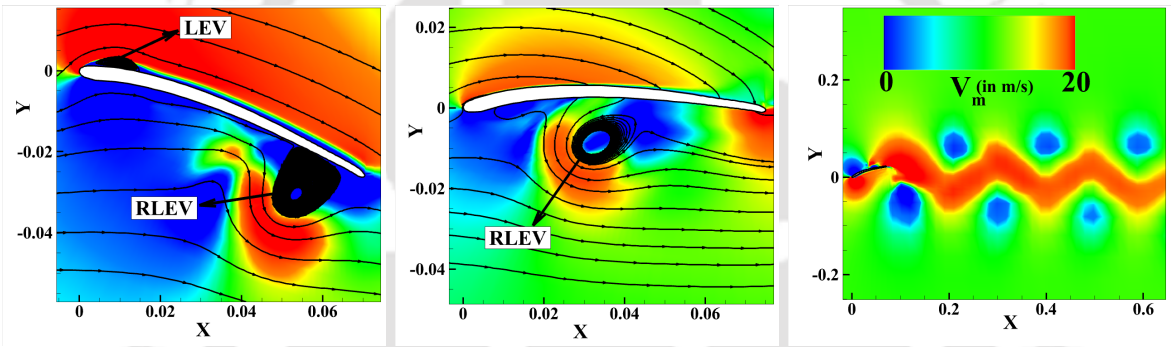

(a) Upstroke (b) Mean position (c) Wake pattern

Figure 5.15: The streamline flow along with the contours of velocity magnitude (V_m) of the wing pitching at $\alpha_p = 20°$, $\theta_m = 0°$, $k_f = 1$

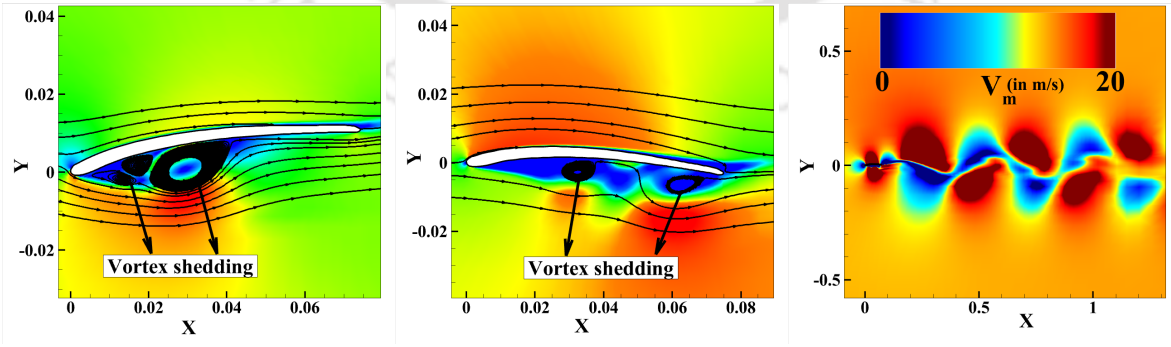

(a) Downstroke (b) Mean position (c) Wake pattern

Figure 5.16: Velocity magnitude (V_m) plots along with stream line flow field of the wing pitching at $\alpha_p = 10°$, $\theta_m = 0°$ and $k_f = 1$

It is observed that, during upstroke, the flow is separated at the leading edge, forming

a leading edge vortex (LEV) on the suction side of the wing. It is also observed that, the flow reattaches to the surface before leaving the trailing edge satisfying the Kutta condition. The flow past the trailing edge forms trailing edge vortex (TEV) on both suction side and pressure side of the wing. As the cycle continues, the TEV from suction side sheds in the wing's wake as a rotating counter clockwise (CCW) vortex above the mean line. At the same time, the TEV which was formed over the pressure side of the wing sheds into the wake as a clockwise rotating (CW) vortex below the mean line as shown in Fig. 5.14. These two vortices form a thrust producing Reverse Karman Vortex (RKV) street as shown in Fig. 5.18(a). Due to this, the wing generates positive thrust at at $\alpha_p = 30°$ in combination with $k_f = 1$. However, at $\alpha_p = 20°$, in combination with $0.5 \leq k_f \leq 1$, negative values of C_t and η_p are observed. These negative values are even higher when α_p decreases to 10°. To understand the reasons behind such behavior, the flow field around the wing is analysed at $\alpha_p = 20°$ and 10° with $k_f = 1$ in both the cases, presented in Fig. 5.15 and Fig. 5.16 respectively.

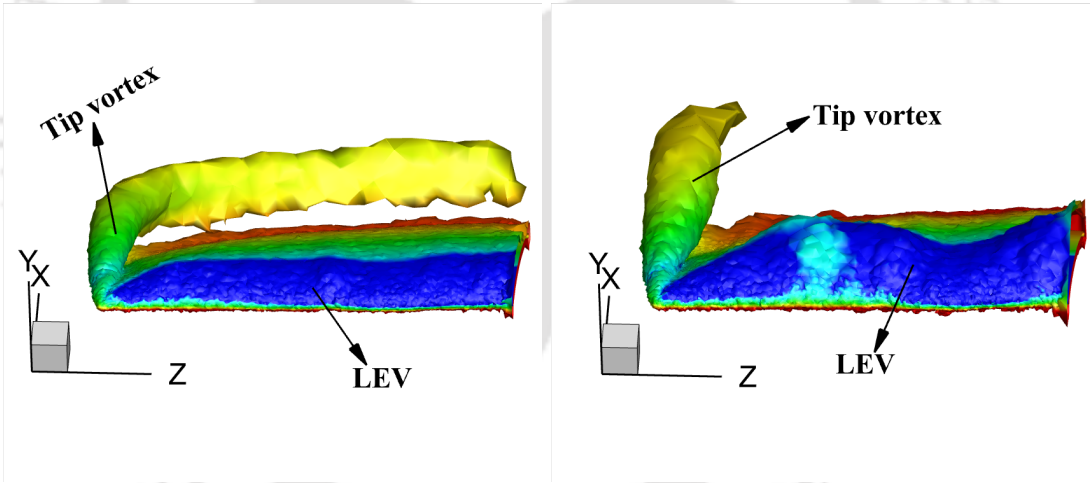

(a) $\alpha_p = 10°$ (b) $\alpha_p = 30°$

Figure 5.17: Iso surface of Q-criterion of flow around the biomimetic wing at Q = 50 with respect to α_p at $\theta_m = 0°$, $k_f = 2$

From Fig. 5.15, it is observed that, at the end of the upstroke, the flow is separated at the leading edge and forms a LEV on the suction side of the wing. At the same time an unsteady LEV which was formed over the pressure side of the wing moves towards the trailing edge of the wing. This unsteady LEV is named as Residual LEV (RLEV) for better explanation purpose. At the mean position of the wing, the flow is fully attached on the suction side of the wing. But the RLEV which was formed due to the flow separation on the pressure side of the wing creates negative suction, opposing the positive suction created on the suction side. This makes hard for the wing to generate

positive thrust. Due to these reasons negative values of C_t and η_p are observed upto k_f = 1 at $\alpha_p = 20°$ (shown in Fig. 5.13). From Fig. 5.16, it is observed that, the further decrease in α_p to 10°, not only increases the unstable nature of the RLEV (which was formed over the pressure side of the wing) but also decrease the wing's influence on the surrounding fluid. Due to these reasons, the negative values of C_t and η_p at $\alpha_p = 10°$ are higher than that of at $\alpha_p = 20°$ and affects the aerodynamic performance of the wing at $0.5 \leq k_f \leq 1.5$.

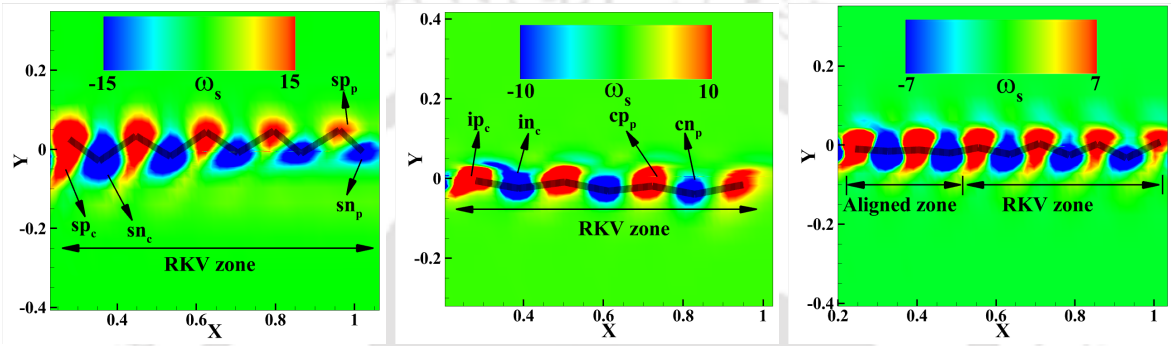

(a) $\alpha_p = 30°$ (b) $\alpha_p = 20°$ (c) $\alpha_p = 10°$

Figure 5.18: Wake pattern of wing pitching at different amplitudes at $k_f = 3$ and $\theta_m = 0°$

The flow around the wing is further analysed by calculating the iso-surfaces of Q-criterion with Q = 50 at different α_p, presented in Fig. 5.17. A more prominent convection of LEV is observed with respect to increase in α_p. As α_p increases from 10° to 30°, the LEV changes its nature from flat to arch (∧) type LEV along the span. As the number of cycles increases, this vortex roll-up and interacts with the tip vortex which was formed closer to the wing's tip as shown in Fig. 5.14. These vortices shed in the wake in the form of the alternating vortices and eventually forms a thrust producing RKV wake as shown in Fig. 5.18(a). From the Fig. 5.13(b) it is also observed that, the η_p decreases after a critical value of k_f at any given α_p. From the flow field analysis it is observed that, the drop in the η_p is due to the change in the nature of wake structure. It is observed that, as k_f increases, the number of vortices shed per cycle increases. This causes an interference between the vortices shed between the previous cycle and the next cycle, leading to the formation of the flat and fixed wake which affects the propulsion efficiency of the wing. Due to this a drop in η_p is observed in Fig. 5.13(b) after a critical value of k_f is reached. However, the C_t rises continuously (as shown in Fig. 5.13(a)) despite of the drop in η_p is due to increase in the overall strength of the vortices with respect to increase in k_f. To qualitatively analyse the influence of pitching amplitude (α_p) on the vortex strength, the spanwise vorticity (ω_s) structure of the wing

pitching at different amplitudes is presented in Fig. 5.18. The increase in α_p increases the growth of the ω_s which can be observed from the ranges of ω_s provided from Fig. 5.18(a) to 5.18(c). At $\alpha_p = 30°$, the alternating vortices shed in the form of a strip shaped positive vortex (sp_c) and negative vortex (sn_c) during each cycle. These vortices form the RKV street along with the positive and negative vortices shed in the previous cycles (sn_p and sn_p respectively). The center to center distance between two adjacent dipoles is approximately same, indicating that the corresponding RKV street is stable. At $\alpha_p = 20°$, the alternating vortices shed in the form of an irregular shaped positive vortex (ip_c) and negative vortex (in_c) during each cycle. These vortices form the RKV street and transform in the form of a circular shaped positive and negative vortices (cp_p and cn_p) as the cycle progresses as shown in Fig. 5.18(b). At $\alpha_p = 10°$, a transformation from aligned wake to the RKV wake is observed. The centers of the alternating vortices almost aligned and forms an aligned wake structure. Thereafter, the alternating vortices exhibit a change in the behavior due to which the RKV street is observed after certain number of cycles as shown in Fig. 5.18(c).

5.3.2 Effect of pitching axis

To analyse the effect of pitching axis, the numerical study is carried out at three different locations. In this case, $\alpha_p = 30°$ and $\theta_m = 0°$ is maintained constant.

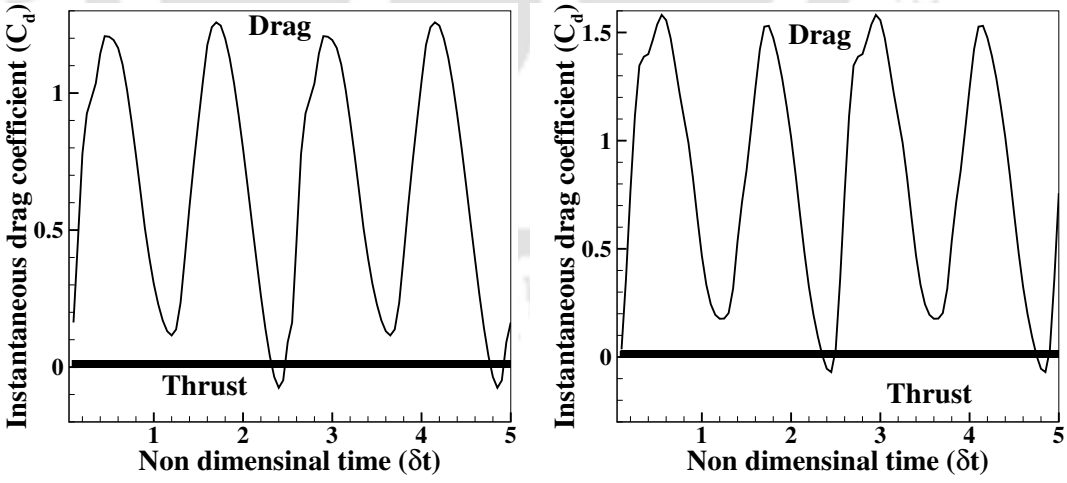

(a) At quarter chord (b) At mid chord

Figure 5.19: Variation in instantaneous drag coefficient of the wing pitching at $k_f = 2$ with different pitching axis locations with $\theta_m = 0°$ and $\alpha_p = 30°$

The variation in instantaneous drag coefficient (C_d) when the pitching axis shifted to quarter chord and mid chord locations is presented in Fig. 5.19. The variation in C_d

when pitching axis is located at leading edge in combination with $\theta_m = 0°$ and $\alpha_p = 30°$ is already presented in Fig. 5.10 and elaborately discussed in section 5.3.1.

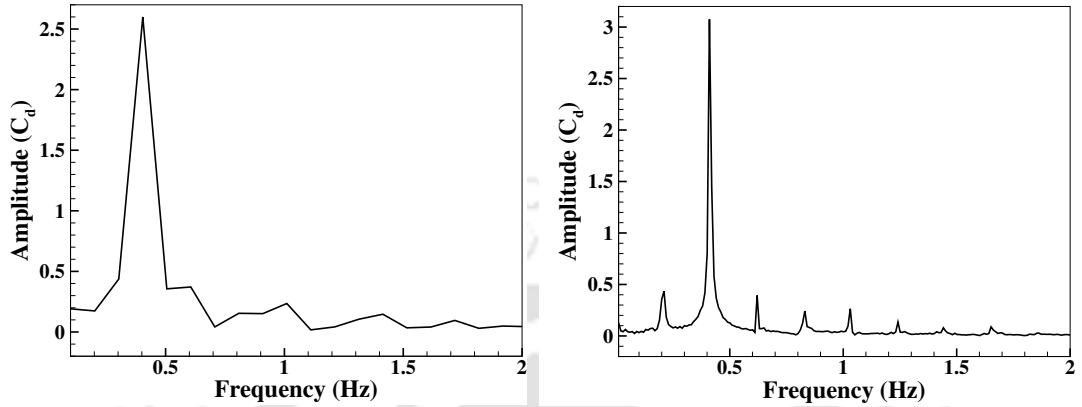

(a) At quarter chord (b) At mid chord

Figure 5.20: Amplitude spectrum of the wing pitching at $k_f = 2$ with different pitching axis locations with $\theta_m = 0°$ and $\alpha_p = 30°$

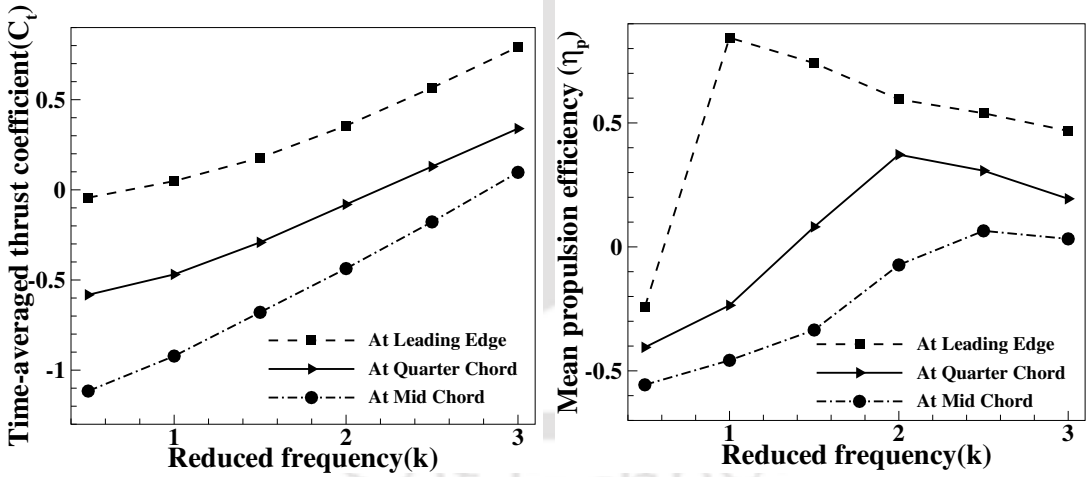

(a) Variation of thrust coefficent (b) Variation of propulsion efficiency

Figure 5.21: Aerodynamic performance of the pitching wing with respect to reduced frequency at different pitching axis locations with $\theta_m = 0°$ and $\alpha_p = 30°$

It is observed that the C_d curve exhibits periodic motion and also has a sinusoidal pattern. However a rise in the C_d curve (towards positive values) with a slight deviation in the sinusoidal pattern is observed when the pitching axis shifts towards the mid chord. This indicates that the wing is unable to overcome the drag offered by the surrounding fluid in order to generate the positive thrust during the major portion of the cycle when the pitching axis is shifted towards trailing edge. As seen in Fig. 5.20, the higher

amplitude spectrum at low frequency indicates that the presence of viscous drag is more when the pitching axis is located at mid chord than that of at quarter chord.

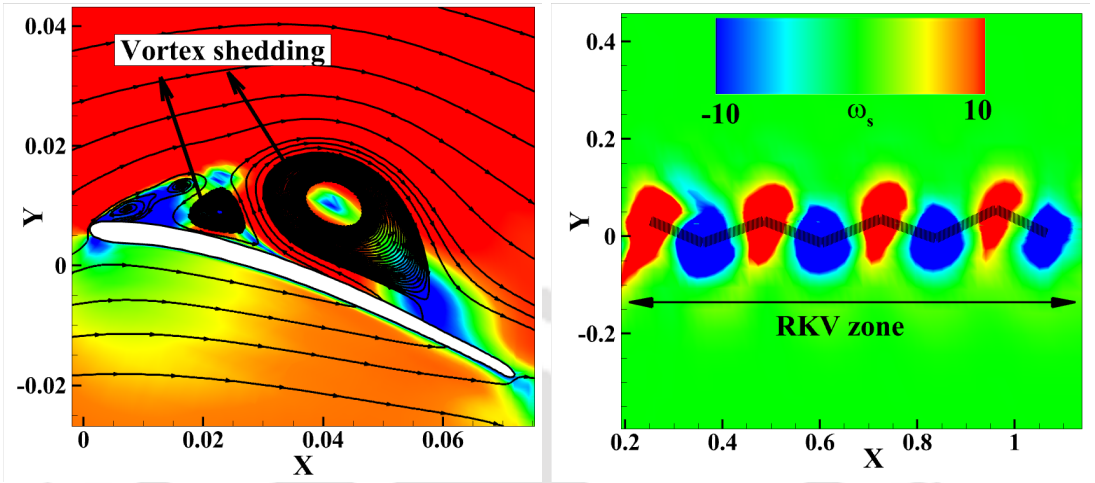

(a) Upstroke (b) Wake pattern

Figure 5.22: Flow around the wing pitching at $\theta_m = 0°$, $\alpha_p = 30°$ and $k_f = 1.5$ with pivot point being at quarter chord point

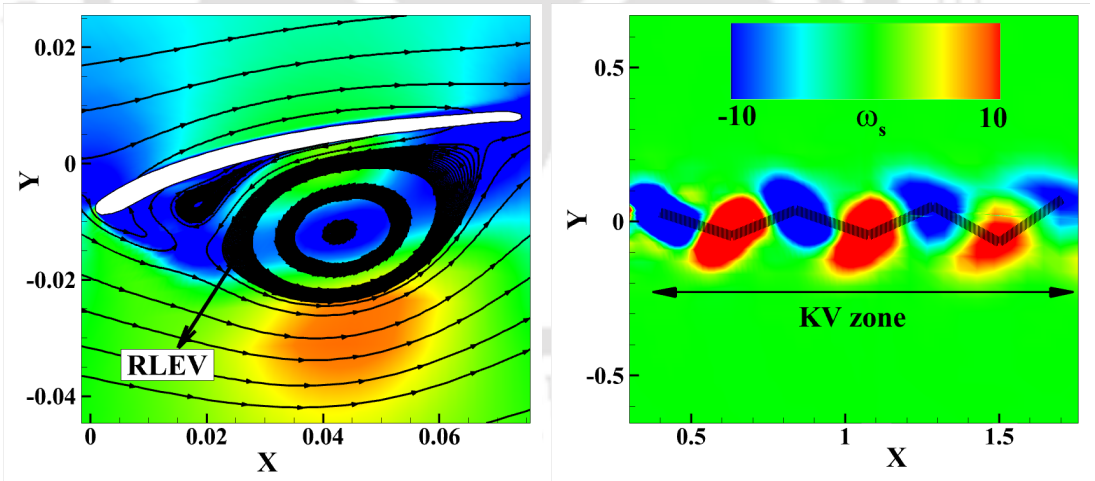

(a) Down stroke (b) Wake pattern

Figure 5.23: Flow field around the wing pitching at $\theta_m = 0°$, $\alpha_p = 30°$, $k_f = 2$ with pivot point being at mid chord point.

The investigations are further carried out by estimating the mean thrust force coefficient (C_t) and propulsion efficiency (η_p) using Eq. 5.2 to Eq. 5.5. The variation in C_t and η_p of wing pitching at different pitching axis locations with respect to the k_f are presented in Fig. 5.21. From Fig. 5.21 it is clearly observed that the performance of

the wing decreases as the pitching axis moves towards the trailing edge, possibly due to the flow separation as shown in Fig. 5.22 and 5.23. It is also observed that the critical frequency (k_c) increases as the pitching axis shifts towards the trailing edge. The wing is able to generate positive thrust only if $k_f \geq 2$ when the pitching axis is located at quarter chord length. Only drag is observed upto $k_f = 2.5$ when the pitching axis is at mid chord length. To understand the reasons behind such performance, the flow field around the wing at quarter chord and mid chord locations is investigated and presented from Fig. 5.22 to Fig. 5.23 respectively. The flow field at $\theta_m = 0°$ with $\alpha_p = 30°$ with pitching axis at leading edge is already discussed in Fig. 5.14 of section 5.3.1. From Fig. 5.22(a), it is observed that the flow separates due to massive vortex shedding over the suction side of the wing. The lift and thrust force coefficients of the wing decreases as long as these vortices are attached to the surface. Due to this, the wing is unable to generate enough thrust at frequencies upto $k_f = 2$ as shown in Fig. 5.21 when the pitching axis of the wing is at quarter chord location. The shedding of alternating vortices form the RKV wake at $k_f = 3$ as shown in Fig. 5.22(b) and the wing generates thrust which can be seen from Fig. 5.21(a) . The flow field at $k_f = 2$, $\theta_m = 0°$, $\alpha_p = 30°$ with the pitching axis location at mid chord is shown in Fig 5.23. It is observed that the flow over the suction side of the wing is fully attached during down stroke and the alternating vortices form the KV wake (Fig. 5.23(b)). Also, the negative suction created due to the opposite re circulation over the pressure side (Fig. 5.23(a)) has adverse effects over the wing's aerodynamic performance. Due to these reasons, only drag is observed when the pitching axis shifts towards mid chord upto $k_f = 2.5$ as shown in Fig. 5.21.

5.3.3 Effect of mean Angle of Attack

The study is further extended to investigate the influence of mean angle of attack (θ_m) on the aerodynamic characteristics of the biomimetic wing subjected to pitching motion. In this case a constant value of $\alpha_p = 30°$ is maintained and the pitching axis is fixed at leading edge. The variation in instantaneous drag coefficient (C_d) with respect to non dimensional time is presented in Fig. 5.24. The variation in C_d is periodic but a large deviation in the sinusoidal pattern is observed in the case of $\theta_m = 8°$. It is also noticed that the wing experiences only drag (since C_d rises towards positive values) during major portion of the cycle. From the flow investigations, presented in Fig. 5.26, it is observed that the increase in θ_m encourages early flow separation and formation of strong vortical structures over the wing surface. This makes it hard for the separated flow to reattach. Due to this, higher positive values of C_d are observed in Fig. 5.24. From Fig. 5.25, it is observed that, the presence of multiple peaks in the amplitude spectrum at low

frequency when $\theta_m = 8°$ is greater than that of at $\theta_m = 4°$. This indicates that the flow separation at $\theta_m = 8°$ is much higher than that of at $\theta_m = 4°$ which can also be seen by comparing Fig 5.28(a) and 5.29(a).

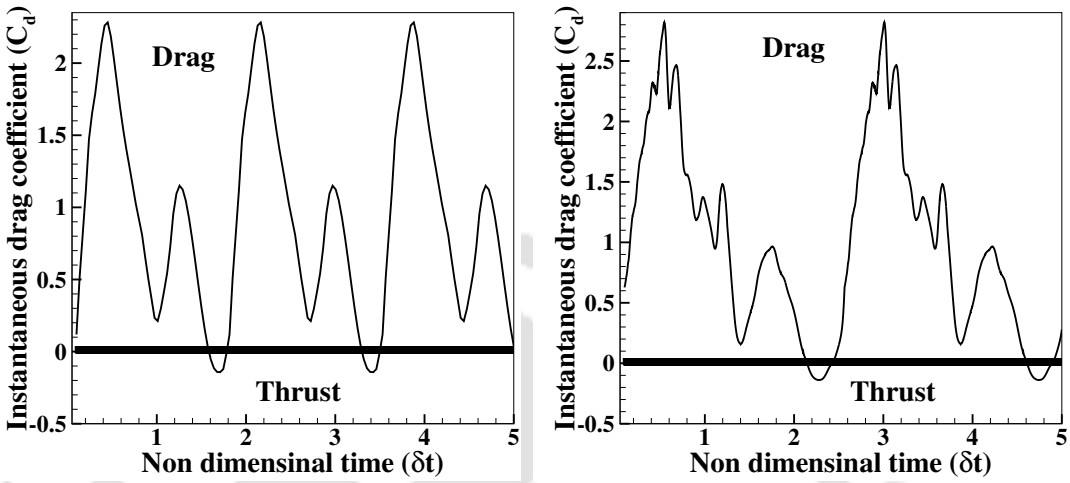

(a) $\theta_m = 4°$ (b) $\theta_m = 8°$

Figure 5.24: Instantaneous drag coefficient (C_d) of biomimetic wing with respect to different θ_m pitching at $\alpha_p = 30°$

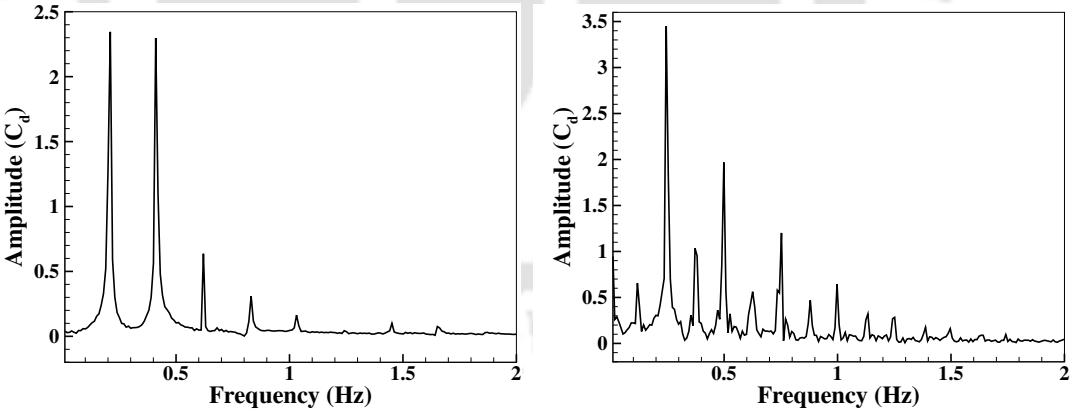

(a) $\theta_m = 4°$ (b) $\theta_m = 8°$

Figure 5.25: Amplitude spectrum of biomimetic wing with respect to different θ_m pitching at $\alpha_p = 30°$

The aerodynamic performance of the biomimetic wing subjected to pitching motion is further analysed by calculating the mean thrust force coefficient (C_t) and propulsion efficiency (η_p) at different θ_m. The variation of C_t and η_p at different θ_m with respect to k_f are presented in Fig. 5.27. It is observed that when $\theta_m \leq 4°$, the thrust force

coefficient (C_t) increases with respect to k_f at a given θ_m. At the same time the C_t decreases with increase in θ_m for a given k_f.

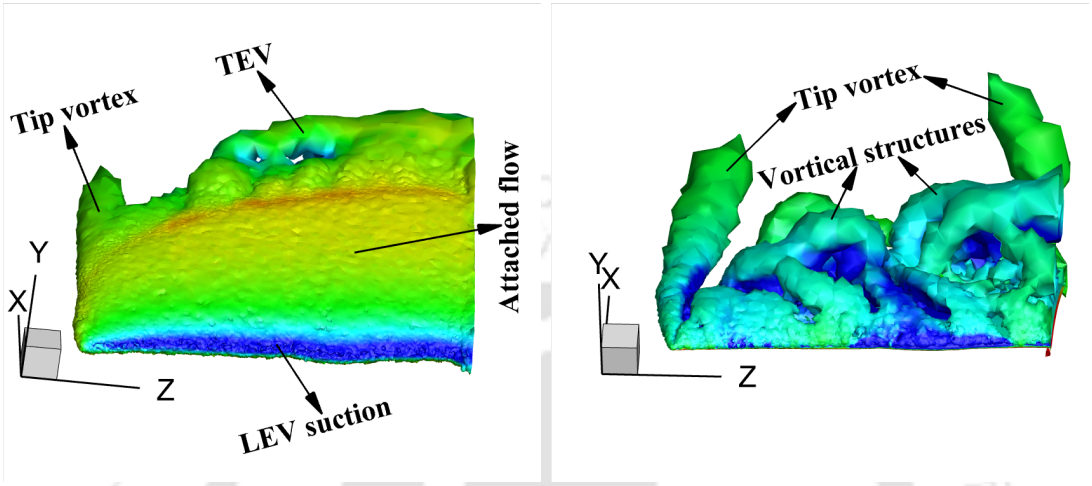

(a) $\theta_m = 0°$ (b) $\theta_m = 8°$

Figure 5.26: Iso surface of Q-criterion of flow around the biomimetic wing at Q = 150 with respect to θ_m at $\alpha_p = 30°$, $k_f = 2$

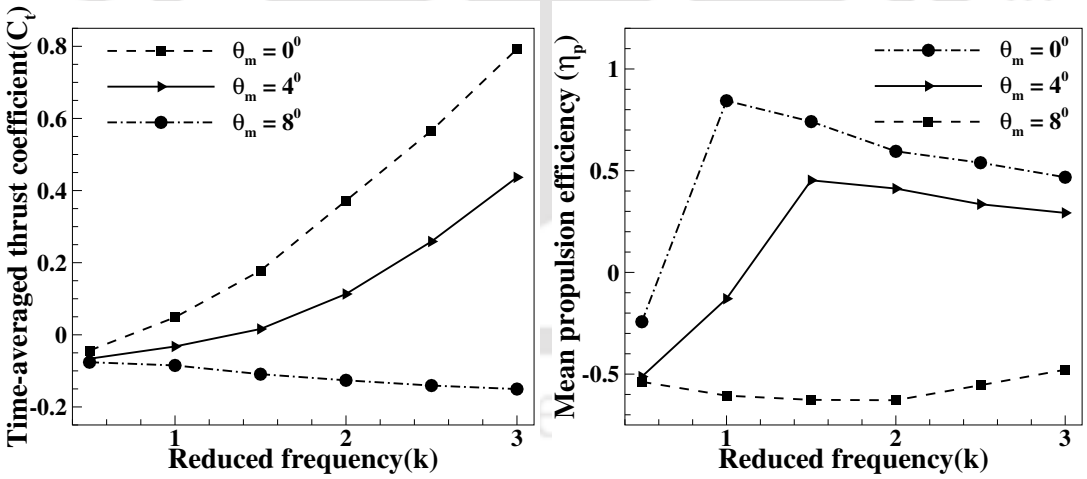

(a) Variation of thrust (b) Variation of propulsion efficiency

Figure 5.27: Aerodynamic performance of the biomimetic wing with respect to k_f at different θ_m with $\alpha_p = 30°$

The propulsion efficiency (η_p) follows the same trend as that of the C_t upto a critical value of k_f and drops with further increase in k_f ($\theta_m \leq 4°$). It is observed that, the wing is able to generate thrust at $\theta_m = 0°$ (when $k_f \geq 1$) and 4° (when $k_f \geq 1.5$). However, at $\theta_m = 8°$ there is only drag. The flow field around the wing at $\theta_m = 4°$ with $\alpha_p = 30°$

and $k_f = 2$ is further investigated, presented in Fig 5.28. It is observed that the flow is fully attached over the suction side of the wing. However, vortex shedding over the pressure side is observed due to flow separation.

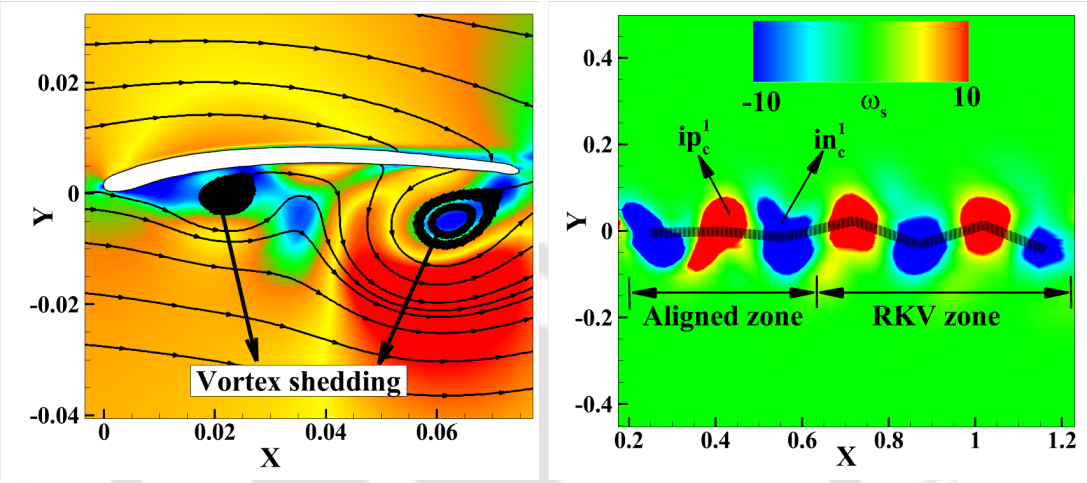

(a) Mean position (b) Wake pattern

Figure 5.28: Flow around the wing pitching at $k_f = 2$, $\theta_m = 4°$, $\alpha_p = 30°$

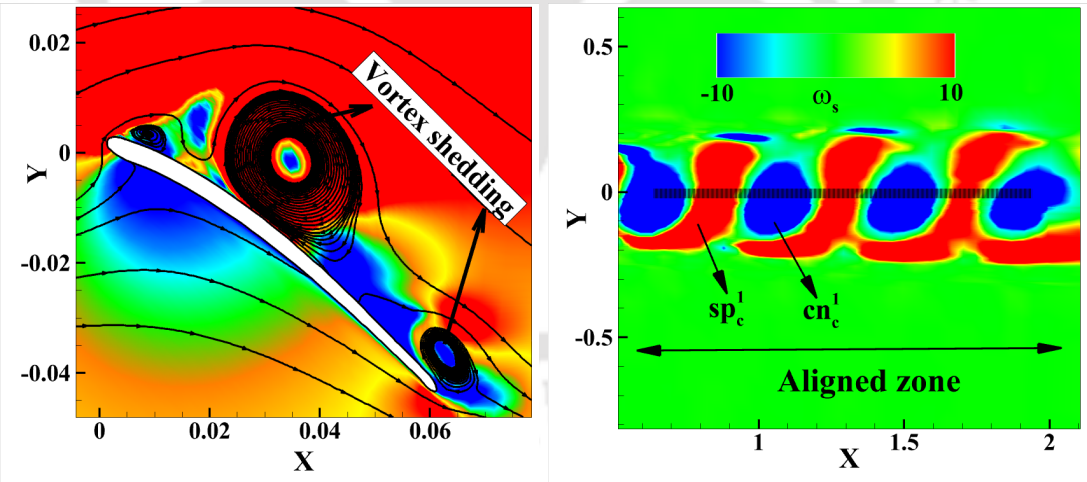

(a) Upstroke (b) Wake pattern

Figure 5.29: Flow field around the wing pitching at $k_f = 2.5$, $\theta_m = 8°$, $\alpha_p = 30°$

The rise in lift and thrust coefficients of the wing can be seen once these vortices shed into wake. The shedding of the alternating vortices in the wake region is shown in Fig 5.28(b). It is observed that the irregular positive and negative vortices from the previous cycle (ip_c^1 and in_c^1) aligned almost in a straight line and forms aligned wake for certain number of cycles. As the number of cycles increases, the irregular alternating vortices

slowly transform into circular shape and forms the RKV wake which is why the positive values of C_t and η_p are observed at $\theta_m = 4°$ when $k_f \geq 1.5$ (shown in Fig. 5.27). In order to understand the peculiar behavior of the wing at $\theta_m = 8°$, the flow field around the wing are analysed at $\theta_m = 8°$ with $k_f = 2.5$ and $\alpha_p = 30°$. The obtained findings are presented in Fig. 5.29. From the stream line plot (flooded with contours of velocity magnitude) which is presented in Fig. 5.29(a), the formation and convection of multiple vortices over the suction side of the wing are observed. Due to the development of these vortical structures, the flow is no longer attached to the wing's surface. This complex nature of the flow not only affects C_d curve with a large deviation in sinusoidal pattern (shown in Fig. 5.24(b)) but also the C_t and η_p of the wing with negative values (shown in Fig. 5.27). Since the wing is no longer in a position to overcome the drag offered by the surrounding fluid, this stalls the overall performance of the wing indicating the presence of dynamic stall. The shedding of alternating vortices is presented in Fig. 5.29(b). It is observed that the wake region at $\theta_m = 8°$ consist of strip shaped positive vortex (sp_c^1) and the circular shaped negative vortex (cn_c^1). The dipoles of these alternating vortices are almost aligned in a straight line which indicates that the alternating vortices fail to form RKV wake. This further confirms that the wing is unable to generate positive thrust under these conditions.

5.4 Summary and conclusions

The present work focuses on investigating the propulsive performance of the wing pitching at Re = $5{\times}10^4$. The effect of pitching amplitude (α_p), mean angle of attack (θ_m), location of pitching axis and reduced frequency (k_f) on thrust force generation and propulsion efficiency are thoroughly investigated. Further, the flow over the wing is also analysed to understand the reasons behind the positive thrust force generation. The obtained results were compared with the findings reported in the literature. A reasonable explanation to the current findings is obtained. At $\alpha_p \leq 20°$ in combination with $k_f \leq 1.5$, unsteady vortex shedding on the pressure side of the wing is identified. At $\alpha_p \geq 30°$ with $k_f \geq 1$ a thrust producing reverse Karman street is observed. Therefore, in order to achieve positive thrust, one can opt for either $k_f \leq 3$ in combination with $\alpha_p \geq 30°$ or $k_f \geq 3$ in combination with $\alpha_p \leq 30°$ depending upon the operating conditions and design constrains while designing wing cross sections for MAVs. Since a large flow separation happens when $\theta_m \geq 8°$, by maintaining $\theta_m \leq 4°$ in combination with $\alpha_p \geq 30°$, enhancement in the propulsive performance can be observed. Also it is observed that shifting of pitching axis away from the leading edge decreases the wing's performance. Therefore, by fixing the pitching axis nearer to the leading edge, positive

thrust generation can be achieved. We hope that the findings reported in this chapter might be helpful to enhance the thrust force generation of the aerial vehicles.

भारतीय प्रौद्योगिकी संस्थान गुवाहाटी
Indian Institute of Technology Guwahati

Chapter 6

Unsteady Flow Characteristics of the Biomimetic Wing Performing Plunging Motion

This chapter presents the aerodynamic performance of the biomimetic wing subjected to plunging motion. An extensive numerical study is carried out to systematically understand the influence of the non-dimensional plunge amplitude (h_a), reduced frequency (k_f) and Reynolds number (Re) regime on the drag-thrust transition of biomimetic wing. It is observed that the investigated parameters remarkably influences the instantaneous force coefficients. It is also observed that these parameters significantly affect the topology of the leading edge vortex which dramatically changes the aerodynamic performance of the biomimetic wing. The details of the generated vortical patterns and the effect of investigated parameters on the flow field are also discussed throughout the chapter.

6.1 Introduction

To understand the complex flow physics behind the nature inspired flights, extensive studies are carried out on different types of airfoils and thin plates undergoing different motion. Out of which the plunging motion of two dimensional airfoils and three dimensional wings grabs substantial interest in recent years.

Chiereghin et al [132] investigated the unsteady lift and pitching moment of harmonically plunging NACA 0012 airfoil at $Re = 2 \times 10^4$ with different mean angles of attack. It was reported that, the unsteady lift generation depends on the presence of Leading Edge Vortex (LEV). It was also reported that the flow over the airfoil varies from fully attached to vortex dominant at higher values of k_f and h_a depending on the

mean angle of attack (θ_m). Cleaver et al [133] carried out experimental investigation of aerodynamic performance over harmonically plunging NACA 0012 airfoil at $Re = 1 \times 10^4$, observed increase in lift coefficient and decrease in drag coefficient with increase in frequency of oscillation. Young and Lai [134] numerically analysed the flow over pure plunging NACA 0012 airfoil at $Re = 2 \times 10^4$ with low plunging amplitudes ($h_a \leq 0.1$) with the frequency range of $1 \leq k_f \leq 10$. They had observed multiple vortex shedding per cycle at higher plunging frequencies. Visbal [135] carried out numerical simulations over plunging SD7003 airfoil at $Re = 6 \times 10^4$. It was reported that flow is fully attached and an approximate 40% reduction in drag is observed at $k_f = 3.93$, $h_a = 0.05$ with 4° mean angle of attack. Cleaver et al [136] compared the forces and flow fields of a plunging NACA 0012 airfoil and flat plate at $Re = 1 \times 10^4$ at 0° and 15° mean angles of attack with small plunging amplitudes. It was observed that, NACA 0012 airfoil experiences high lift coefficient with stable vortex street at $\theta_m = 0°$ with high Strouhal numbers (St) whereas the flat plate at the same conditions experiences fluctuations in lift coefficient. At $\theta_m = 15°$ large flow separation is observed and the flat plate is unable to produce thrust even at high Strouhal numbers. Likewise, a lot of numerical and experimental investigations were carried out to assess the aerodynamic performance of the different airfoils at different conditions [137, 138, 139]. It is observed that, most of the above mentioned studies had shown less attention towards the propulsive performance of the harmonically plunging wing with the conditions prior to that of a MAV. Calderon et al [140, 141] performed Particle Image Velocimetry (PIV) studies on low aspect ratio wings undergoing pure plunging motion. They have reported that the thinner profiles encourage an early flow separation and strong vortex formation. It was also reported that the formation of vortices at high Strouhal number results in loss of lift force generation. The numerical investigations performed by Gross et al [142] on plunging rectangular wing, reported that intermittent flow reattachment increases the mean lift coefficient. But they had shown less attention towards the analysis of propulsive performance of the wing.

The critical insights on flow structure of low aspect ratio wings during plunging motion provided by most of the studies are either at very low Re ($Re \leq 1 \times 10^3$) or at high Re ($Re \geq 1 \times 10^5$). It is observed that the most of the studies used commercial wing planforms like rectangular and elliptical planforms, to investigate the unsteady flow characteristics at low Re. The Re regime of the present study is from 2.5×10^4 to 7.5×10^4 which is the regime of interest to the most of the MAV designers where the flow is turbulent in nature. The numerical analysis of present chapter attempts to investigate the unsteady aerodynamics of biomimetic wing inspired from Passer Domesticus. The influence of the non-dimensional plunge amplitude (h_a), reduced frequency (k_f) and Re regime on the drag-thrust transition of biomimetic wing are systematically analysed.

Additionally the initial stage development of LEV and its influence over the propulsive performance of the wing undergoing plunging motion are also investigated.

6.2 Method

6.2.1 Problem definition

The modelling of the biomimetic wing is discussed in section 4.2.1. The discussions regarding the inertial coordinate system OXYZ and the local coordinate system $OX^1Y^1Z^1$ are already presented in section 5.2.1 of Chapter-5. A schematic view of the biomimetic wing performing plunging motion is presented in Fig. 6.1. The biomimetic wing is subjected to a plunging motion $\Omega(t)$ in an incompressible viscous flow which has a constant free stream velocity of U_∞. The plunging motion of the wing is given by Eq. (6.1)

$$\Omega(t) = \Omega_0 \sin(2\pi f t) \tag{6.1}$$

where Ω_0 is the initial plunge amplitude from the mean position and f is the frequency of oscillation.

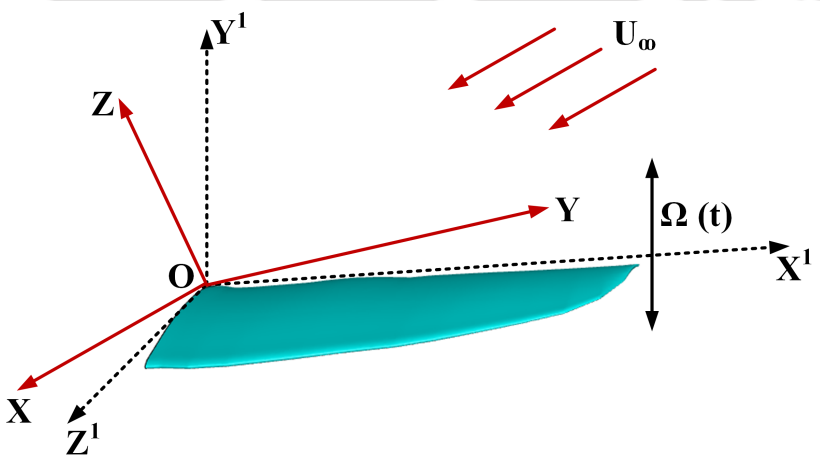

Figure 6.1: Schematic view of the biomimetic wing subjected to plunging motion

The change in effective angle of attack of the wing undergoing plunging motion with respect to the incoming flow is given by:

$$\phi_f(t) = \phi_0 + \tan^{-1}\left(\frac{\dot{\Omega}(t)}{U_\infty}\right) \tag{6.2}$$

where, ϕ_0 is the initial mean angle of attack which is 0^0 for the current study. From

Eq. (6.2), the instantaneous non-dimensional positon of the wing is given as:

$$\bar{\Omega(t)} = h_0 \sin(k_f \delta t) \tag{6.3}$$

where h_0 is the initial dimensionless plunge amplitude ($h_0 = \frac{\Omega_0}{C}$), δt is the non-dimensional time ($\delta t = \frac{tU_\infty}{L}$) and $\bar{\Omega(t)} = \frac{\Omega(t)}{L}$ From Eq. (6.3), the instantaneous dimensionless plunge velocity of the wing is given as:

$$\bar{\vartheta(t)} = k_f h_0 \cos(k_f \delta t) \tag{6.4}$$

where $k_f h_0$ is the maximum dimensionless plunge velocity at $\delta t = 0$. From the definition of Strouhal number (St) provided in Eq. (3.15), the dimensionless plunge velocity can be defined as:

$$k_f h_a = \pi St \tag{6.5}$$

where h_a is the non-dimensional plunge amplitude at any given time t ($h_a = h_0$ for $t = 0$). From Eq. (6.5) it can be observed that the non-dimensional plunge velocity is related by a factor of π to the Strouhal number (St). In the present study, all the results were categorised in terms of non-dimensional plunge velocity ($k_f h_a$) since thrust and propulsion efficiency are strong functions of $k_f h_a$ when plunging motion is considered [82]. However, conversations in terms of St are also made wherever necessary.

6.2.2 Computational details

6.2.2.1 Domain independence

The details of the wing modelling and meshing of the computational domain are presented in sections 4.2.1 and 4.2.2.1 of Chapter - 4 respectively. The plunging motion is provided to the wing by using a compiled User Defined Function (UDF) developed based on Eq. (6.1) to Eq. (6.5). From the initial time refinement study (carried out from t^* = 1×10^{-3} s to 1×10^{-4} s), it is observed that there is no variation in the instantaneous force coefficients from time step t^* = 5×10^{-4} s to 1×10^{-4} s. Therefore, t^* = 5×10^{-4} s is considered with 35 iterations for each time step in all the simulations of the current chapter. To verify the variation in the results with respect to the size of the computational domain, an initial domain independence test was carried out with different domain dimensions (see Table 6.1). The obtained findings are presented in Table 6.1 and Fig. 6.2 respectively. The error percentage is calculated based on the findings obtained between two consecutive domains. It is observed that the instantaneous force coefficients are almost invariant with respect to the dimensions of the fluid domain at $h_a = 0.1$ in

combination with $k_f = 1.5$. However, the dimensions of Domain 2 are considered for further studies in order to avoid the influence of outer boundaries at higher values of h_a and k_f.

Table 6.1: Comparison of mean lift and drag coefficients of biomimetic wing for different domains plunging at $Re = 5 \times 10^4$, $h_a = 0.1$, $k_f = 1.5$ and $\theta_m = 0°$

Domain type	Radius (r_1)	Distance (x_1)	Mean C_l	Error(%)	Mean C_d	Error(%)
Domain 1	25C	50C	4.8071	—	-1.0278	—
Domain 2	50C	100C	4.7981	0.187	-1.0249	0.28
Domain 3	75C	150C	4.7905	0.158	-1.0226	0.22

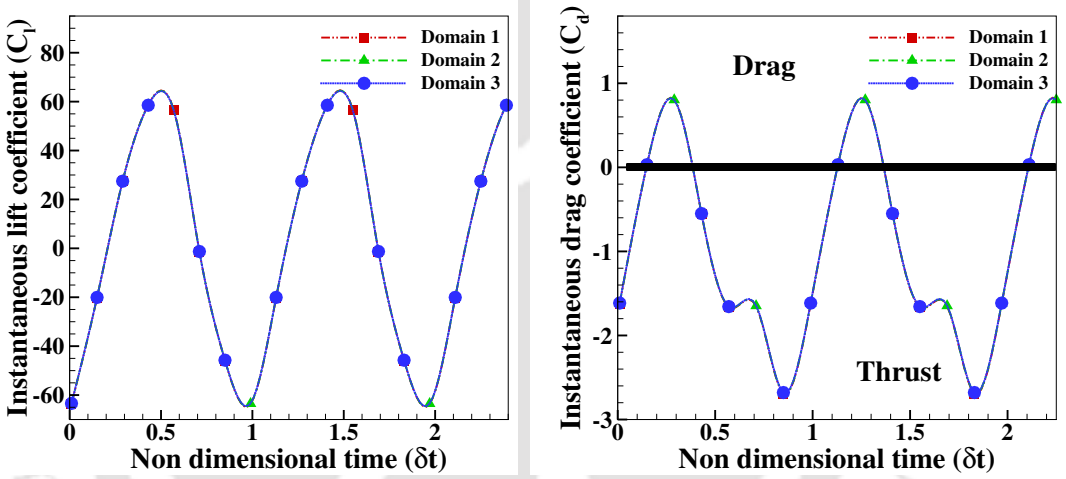

(a) Lift coefficient (b) Drag coefficient

Figure 6.2: Comparison of instantaneous lift and drag coefficients of biomimetic wing using three different domains plunging at $Re = 5 \times 10^4$, $\theta_m = 0°$, $h_a = 0.1$ and $k_f = 1.5$

6.2.2.2 Grid independence

To investigate the sensitivity of the results with respect to the grid size, the grid independence test was carried out with grids of three different sizes (shown in Table 6.2). The obtained findings of lift and drag coefficients of biomimetic wing with respect to three different grids are presented in Table 6.2 and Fig. 6.3. The percentage of error (shown in Table 6.2) is calculated using the findings obtained between two consecutive grids. It is noticed that the findings obtained using Grid 1 are slightly higher than that of Grid 2 and Grid 3. It is also observed that the variation between the findings obtained using Grid 2 and Grid 3 is almost negligible. In overall a good agreement is obtained between the findings of both Grid 2 and Grid 3. Since Grid 2 offers less computational time than that of Grid 3, further investigations are carried out by using Grid 2 configurations.

Table 6.2: Comparison of average lift and drag coefficients of biomimetic wing for different grids plunging at $Re = 5 \times 10^4$, $h_a = 0.1$, $k_f = 2.5$ and $\theta_m = 0°$ (Min. OQ refers to the minimum orthogonal quality)

Mesh type	Size	Min. OQ	Avg. C_l	Error(%)	Avg. C_d	Error(%)
Grid 1	18.7×10^5	0.182	7.2401	—	-2.9552	—
Grid 2	41.3×10^5	0.237	7.0176	3.073	-2.7835	6.17
Grid 3	87.4×10^5	0.323	6.9312	1.23	-2.7256	2.12

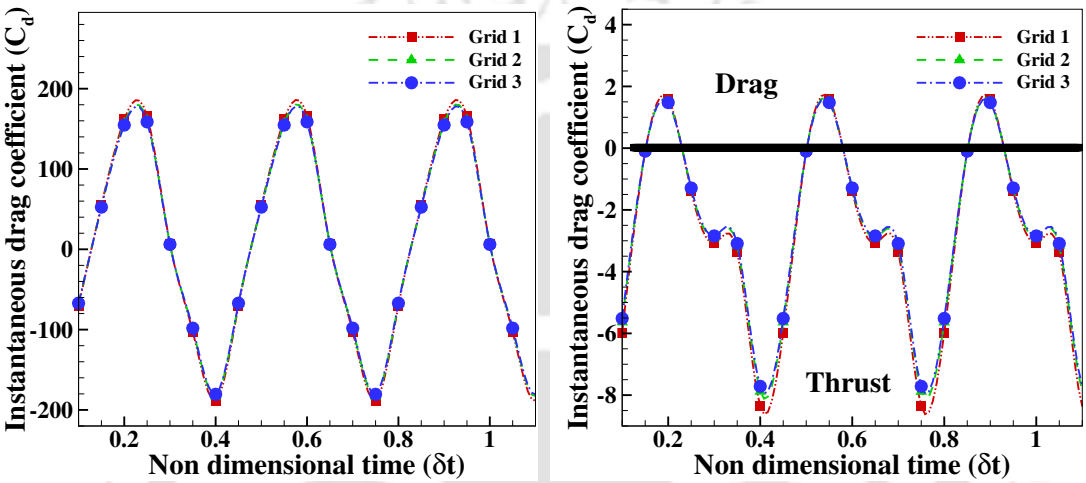

(a) Lift coefficient (b) Drag coefficient

Figure 6.3: Comparison of instantaneous lift and drag coefficients of biomimetic wing using three different grids plunging at $Re = 5 \times 10^4$, $h_a = 0.1$, $k_f = 2.5$ and $\theta_m = 0°$

6.2.2.3 Validation

To validate the current numerical approach, the experimental findings reported by Heathcote et al [5] on rectangular wing with NACA 0012 airfoil cross section at $Re = 2 \times 10^4$ and 3×10^4 are considered. Heathcote et al [5] conducted the experiments by varying k_f from 0 to 3 at constant plunge amplitude of 0.175. The chord length is maintained as 100 mm. The numerical simulations were carried out by considering aforementioned conditions as a reference. The mean thrust coefficient (C_t) and propulsion efficiency (η_p) in the range of $0 \leq k_f \leq 3$ is computed at $Re = 2 \times 10^4$ and 3×10^4. The obtained results were compared with the findings reported by Heathcote et al [5] and presented in Fig.6.4. A maximum error of 9.46% and 9.82% is observed between current findings and the findings reported by Heathcote et al [5] while calculating C_t and η_p respectively. It is observed that, the findings obtained using present numerical approach has an encouraging agreement with the experimental findings reported in the literature.

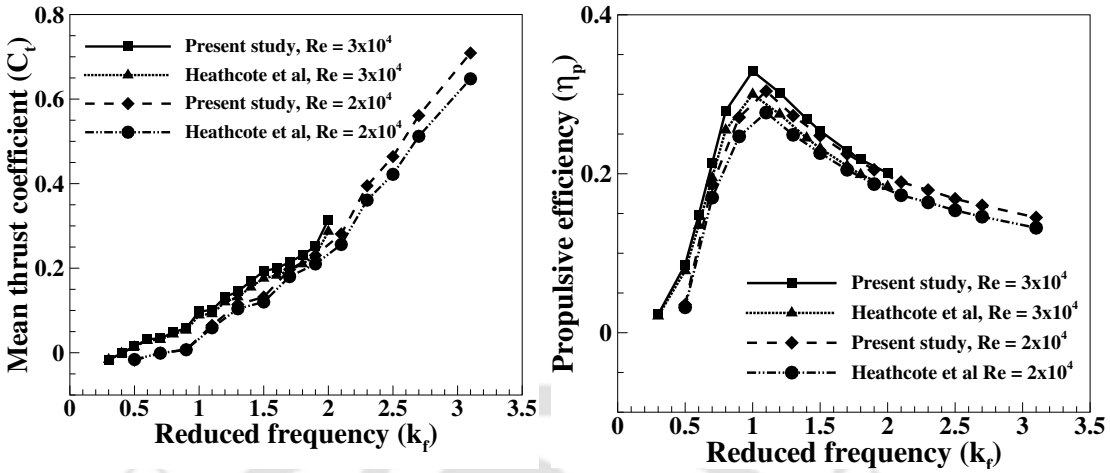

(a) Thrust coefficient (b) Propulsion efficiency

Figure 6.4: Comparison between the findings obtained using present numerical approach and experimental results of Heathcote et al [5]

6.3 Results

6.3.1 Effect of dimensionless plunge amplitude

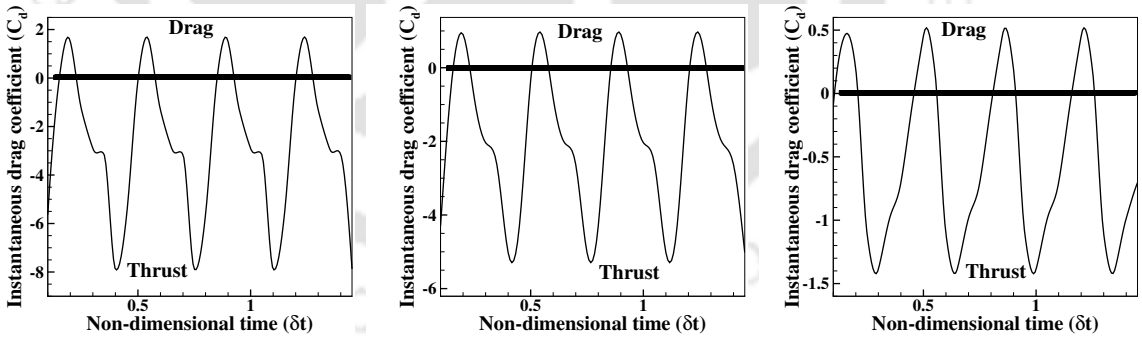

(a) $h_a = 0.1$ (b) $h_a = 0.3$ (c) $h_a = 0.5$

Figure 6.5: Variation of C_d of the biomimetic wing plunging at different h_a at $Re = 5 \times 10^4$ and $\theta_m = 0°$

To analyse the influence of dimensionless plunge amplitude (h_a), the numerical study is carried out at $h_a = 0.1$, 0.3 and 0.5 (which indicates the variation in corresponding Ω_0 as 10%C, 30%C and 50%C respectively) at Reynolds number (Re) 5×10^4. The instantaneous drag coefficient (C_d) of the wing at different h_a is presented in Fig. 6.5. It is observed that the variation in C_d is periodic but not pure sinusoidal and the deviation

from the sinusoidal nature of C_d varies with respect to h_a. This is due to the change in the nature of the flow around the wing with respect to change in h_a which can be observed from Fig. 6.7. It is also noticed that the convection of vortices over the wing surface have a remarkable influence on the cycle to cycle variation of C_d curve with respect to h_a. The negative value of C_d in Fig. 6.5 indicates the thrust force generation of the wing during plunging motion.

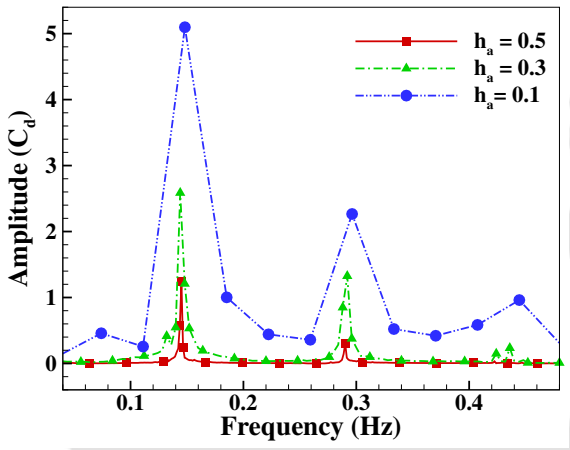

Figure 6.6: Amplitude spectrum of C_d of the biomimetic wing plunging at different h_a at $Re = 5 \times 10^4$ and $\theta_m = 0°$

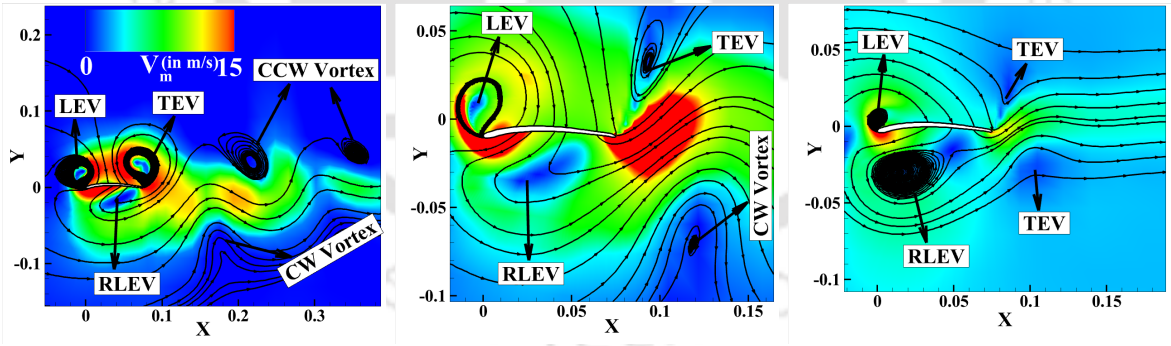

(a) $h_a = 0.1$ (b) $h_a = 0.3$ (c) $h_a = 0.5$

Figure 6.7: Comparison of streamline flow along with contours of velocity magnitude of the biomimetic wing plunging at different (h_a) with $Re = 5 \times 10^4$ and $\theta_m = 0°$

From this preliminary analysis, it is observed that the increase in h_a decreases the thrust force generation of the wing. The investigations are further carried out by calculating the amplitude spectrum of C_d of the wing using the Fourier transformation algorithm. The findings obtained at different h_a are shown in Fig. 6.6. Multiple peaks with different amplitudes are observed in the spectrum of C_d. This is due to the forma-

tion and shedding of the Karman vortices over the suction side and the pressure side of wing as shown in Fig. 6.7.

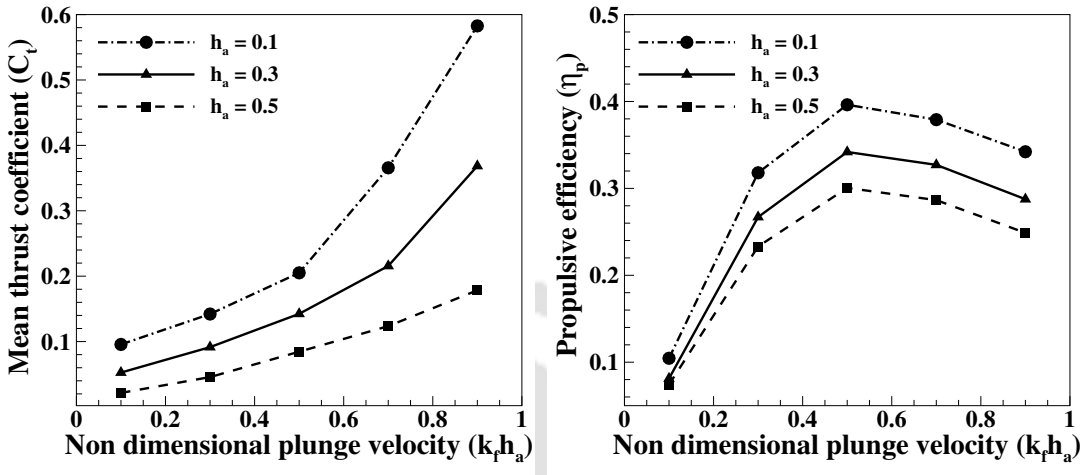

(a) Variation of thrust coefficient (b) Variation of propulsion efficiency

Figure 6.8: Aerodynamic performance of biomimetic wing plunging at different h_a with $Re = 5 \times 10^4$ and $\theta_m = 0°$

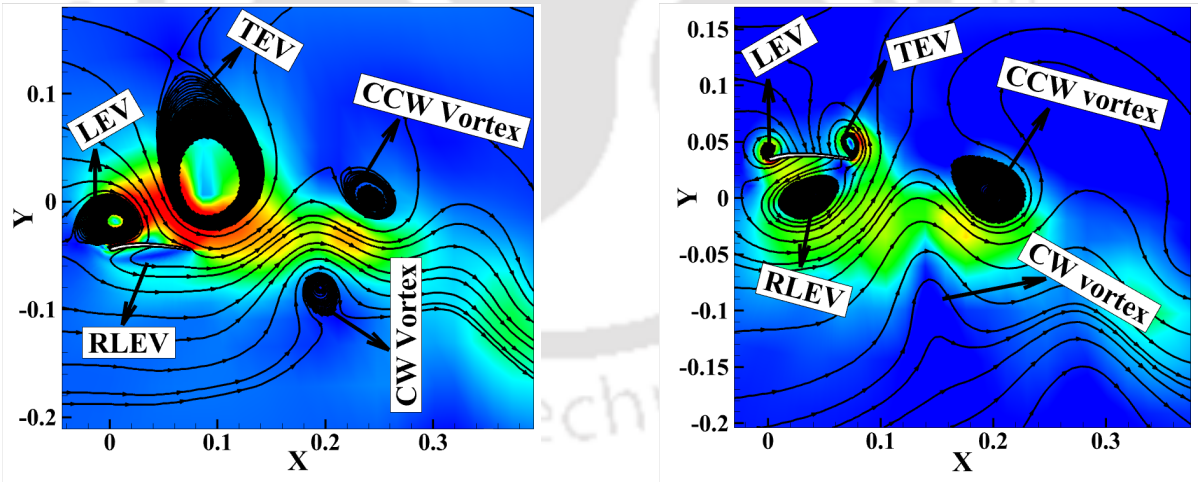

(a) Down stroke (b) Upstroke

Figure 6.9: Contours of velocity magnitude (in m/s) and streamline flow of the biomimetic wing plunging at $Re = 5 \times 10^4$ with $h_a = 0.1$ and $\theta_m = 0°$

It is observed that the higher amplitude peak indicates that the shedding period of the Karman vortices is longer at a given frequency. This increases the strength of the vortices in the wake region and contributes towards thrust force generation of the wing. The lower peak in the spectrum indicates that the shedding period of the Karman

vortices happens only for a very short duration at the corresponding frequency. As it can be seen from Fig. 6.7, the vortices shed into the wake at $h_a = 0.3$ and 0.5 are not strong as that of at $h_a = 0.1$ which is why the thrust force at $h_a = 0.1$ is higher than that of at $h_a = 0.3$ and 0.5.

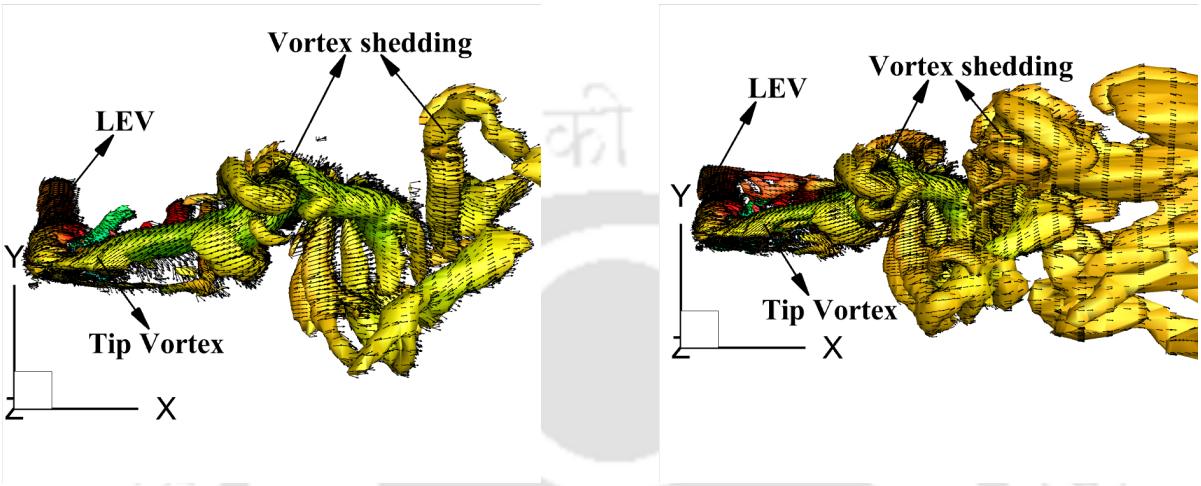

(a) $k_f h_a = 0.3$ (b) $k_f h_a = 0.7$

Figure 6.10: Flow around the wing in the form of iso surface of Q-criterion (at Q = 100) plunging at $Re = 5 \times 10^4$ with $h_a = 0.1$ and $\theta_m = 0°$

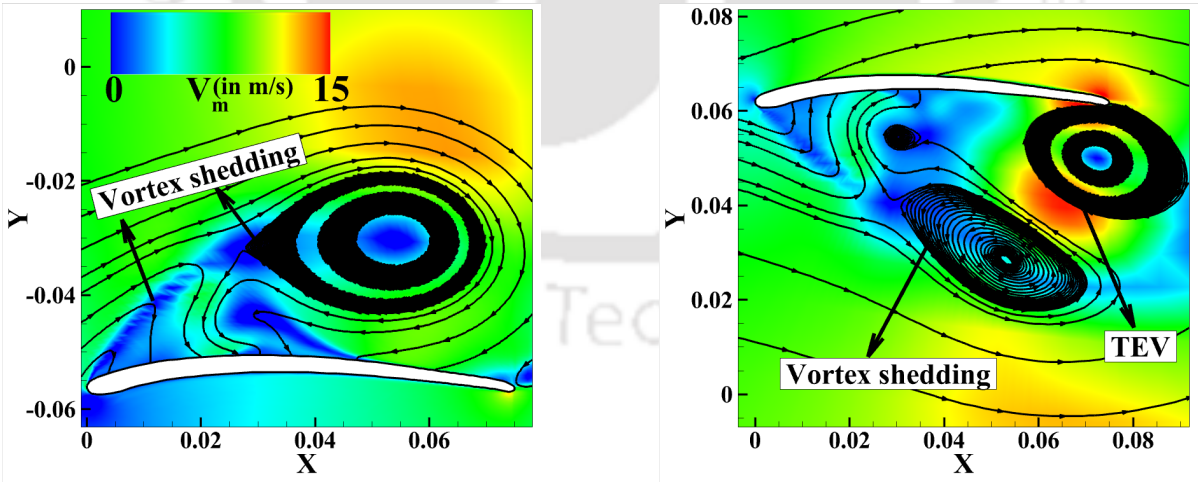

(a) Down stroke (b) Upstroke

Figure 6.11: Plots of streamline flow and velocity magnitude around the biomimetic wing plunging at $Re = 5 \times 10^4$ with $h_a = 0.3$ and $\theta_m = 0°$

The investigations are further carried out to estimate the mean thrust coefficient (C_t) and propulsion efficiency (η_p) of the wing using Eq. 5.2 to Eq. 5.5 presented in section

5.2.2. The obtained findings of C_t and η_p of the wing with respect to non-dimensional plunge velocity ($k_f h_a$) at different values of h_a are presented in Fig. 6.8.

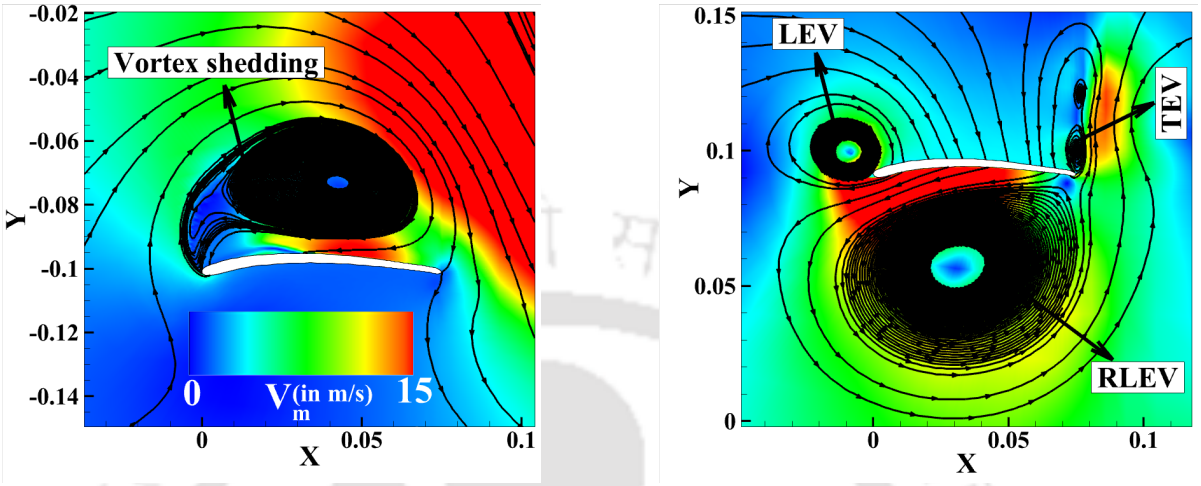

(a) Down stroke (b) Upstroke

Figure 6.12: Streamline flow and velocity magnitude of the biomimetic wing plunging at $Re = 5 \times 10^4$ with $h_a = 0.5$ and $\theta_m = 0°$

It is observed that the positive values of C_t and η_p are due to the formation of thrust producing reverse Karman street (shown in Fig. 6.7). The smaller values of C_t and η_p at lower non-dimensional plunge velocities ($k_f h_a$) are due to presence of viscous drag in those regimes. It is also noticed that, the C_t and η_p increases with increase in $k_f h_a$ for a given h_a. From the flow investigations presented in Fig. 6.10, it is observed that the increase in $k_f h_a$ increases the influence of the wing over the surrounding fluid. This allows the flow to remain attached during the major portion of plunging cycle and decreases the interference between the Leading Edge Vortex (LEV) and tip vortex. From Fig. 6.10, it is also noticed that the increase in $k_f h_a$ increases the strength of the alternating vortcies which shed in the wake region. Due to these reasons, a rise in C_t and η_p is observed with respect $k_f h_a$ for a given value of h_a. It is also observed that, C_t and η_p decreases with increase in h_a for a given value of $k_f h_a$. From the flow field investigations, it is observed that the major portion of the plunging cycle suffers with a large flow separation at higher values of h_a due to massive vortex shedding which can be observed from Fig. 6.9 to 6.12. Also, the increase in h_a decreases the strength of the vortex in the wake region as shown in Fig. 6.7. Due to these reasons, the C_t and η_p decreases with increase in h_a. From Fig. 6.8(b), a drop in propulsion efficiency is observed after a certain value of $k_f h_a$ is reached which is a critical value for a given h_a. By analysing the flow field around the wing, it is observed that, once a critical value of $k_f h_a$ is reached, the alternating vortices which shed in previous cycle interact with the vortices of the next cycle and the wake structure

becomes flat after a critical value of $k_f h_a$ due to which the drop in η_p is observed. The numerical simulations carried out by Young and Lai [134] on NACA 0012 airfoil from $2\times10^4 \leq Re \leq 4\times10^4$ had also observed drop in propulsion efficiency at higher Strouhal numbers (St) and reported the drop is due to flat and finite width of the wake which also supports the findings reported in the present study.

The flow over the wing plunging at $h_a = 0.1$ and $Re = 5 \times 10^4$ is analysed and presented in the form of stream line flow along with contour plots of velocity magnitude as shown in Fig. 6.9. During down stroke, the flow over the suction surface of the wing separates at the leading edge and forms a Leading Edge Vortex (LEV); it reattaches approximately at the quarter chord length. At the same time a LEV is also formed due to the flow separation over the pressure side of the wing which flows towards the trailing edge. For better explanation, the LEV over pressure side of the wing is named as Residual Leading Edge Vortex (RLEV). This RLEV creates opposite suction over the pressure side which opposes the suction created over suction side as long as it attached to the wing's surface. From Fig. 6.9, it is observed that, the strength of the RLEV during upstroke is greater than that of the down stroke. Due to this, the lift and thrust coefficients has the lowest values during the upstroke, a rise in these force coefficients can only be seen during down stroke. As the cycle continues, the flow past the trailing edge forming a trailing edge vortex (TEV) over the suction side of the wing. This TEV sheds into the wake above the mean line as a counter clockwise (CCW) rotating vortex. At the same time, the TEV which was formed over the pressure side shed below the mean line as a clockwise (CW) rotating vortex. This forms a thrust producing reverse Karman street in the wake region. From the Fig. 6.9, it is observed that the strength of the TEV clearly outweights that of LEV. This nullifies the adverse effects of LEV and the thrust coefficient has the maximum values at $h_a = 0.1$ which can also be observed from Fig. 6.8.

The stream line flow along with velocity magnitude plots of the wing plunging at $h_a = 0.3$ and $Re = 5 \times 10^4$ is presented in Fig. 6.11. The vortex formation and shedding at different positions of the wing for $h_a = 0.5$ with $Re = 5 \times 10^4$ is presented in Fig. 6.12. In both the cases, the formation of LEV is observed due to flow separation at the leading edge over the suction side of the wing and the flow reattaches to the surface before leaving the trailing edge satisfying the kutta condition. During upstroke of the cycle, the formation and shedding of the vortices over the pressure side of the wing is observed. By comparing Figs. 6.9, 6.11 and 6.12, an increase in the strength of the LEV is observed with respect to h_a. This increase in the strength of the LEV has detrimental effects on the aerodynamic performance of the wing as it makes hard for the flow to reattach with increase in h_a. Also, the increase in strength of RLEV with respect to h_a

increases the negative suction on pressure side. Due to these reasons, the aerodynamic characteristics of the wing decreases with increase in h_a which can also be observed from Fig. 6.8.

6.3.2 Effect of reduced frequency

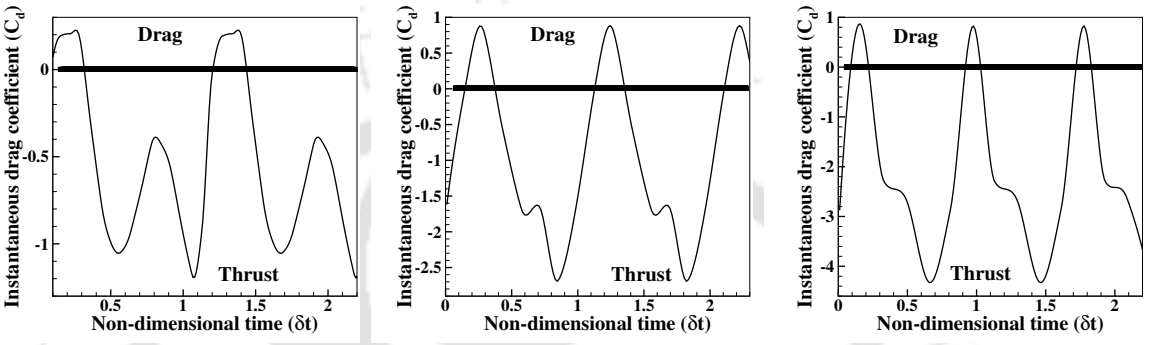

(a) $k_f = 0.5$ (b) $k_f = 1.5$ (c) $k_f = 2.5$

Figure 6.13: Variation in C_d of the biomimetic wing plunging different k_f with $Re = 5 \times 10^4$ and $\theta_m = 0°$

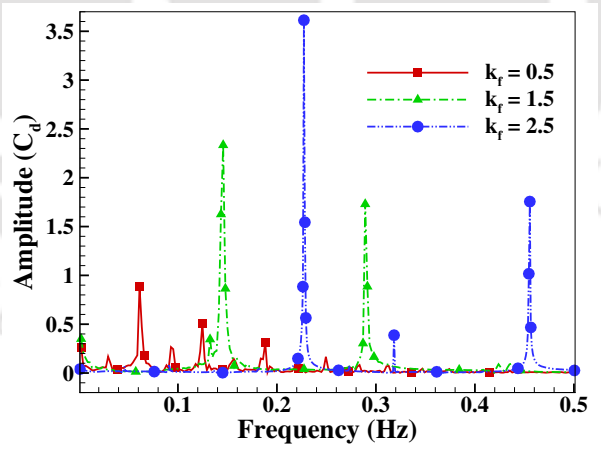

Figure 6.14: Amplitude spectrum of C_d of the biomimetic wing plunging different k_f with $Re = 5 \times 10^4$ and $\theta_m = 0°$

The numerical investigations are further carried out to analyse the influence of reduced frequency (k_f) on the aerodynamic performance of the biomimetic wing subjected to plunging motion. From the preliminary investigations, it is observed that the wing experience only drag when $k_f \leq 0.4$. Therefore, the study is carried out by maintaining $k_f \geq 0.5$ with an increment of 0.5 upto 2.5 at $Re = 5 \times 10^4$.

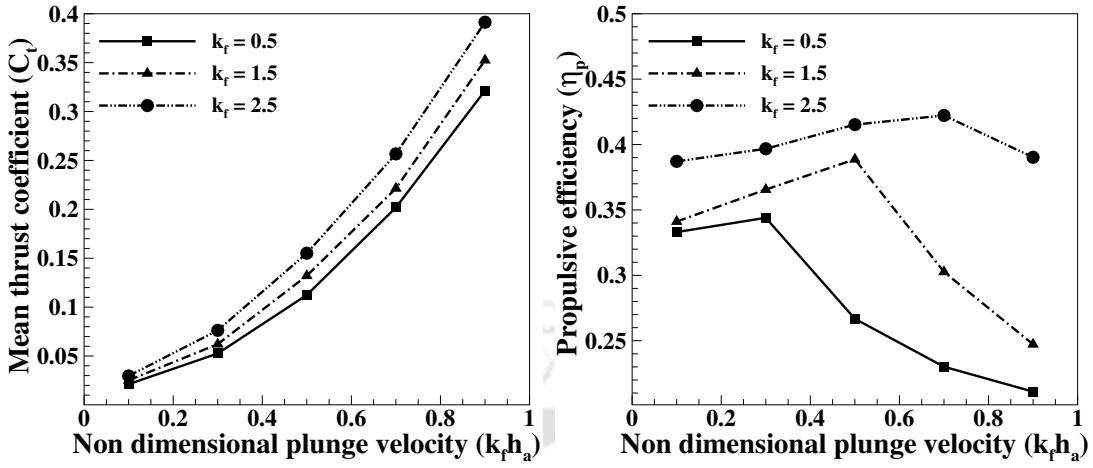

(a) Variation of thrust coefficient (b) Variation of propulsion efficiency

Figure 6.15: Aerodynamic performance of the biomimetic wing plunging at different k_f with $Re = 5 \times 10^4$ and $\theta_m = 0°$

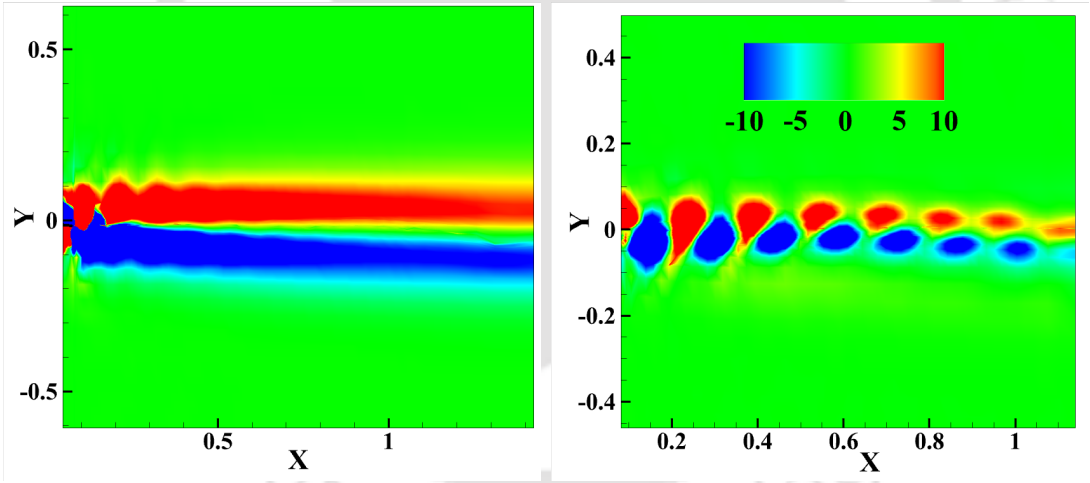

(a) $k_f = 0.5$ (b) $k_f = 2.5$

Figure 6.16: Wake pattern of the biomimetic wing plunging at different k_f with $Re = 5 \times 10^4$ and $\theta_m = 0°$

The variation in instantaneous drag coefficient (C_d) of the wing plunging at different values of k_f is presented in Fig. 6.13. A non-sinusoidal periodic motion is observed in C_d with respect to k_f. The deviation from the sinusoidal nature of C_d is different at different k_f. The higher negative values of C_d in Fig. 6.13 indicates high thrust force generation. This can also be seen from the amplitude spectrum of C_d presented in Fig. 6.14 by observing the peaks at different values of k_f. It is observed that the increase in k_f accelerates the plunging motion of the wing with respect to incoming fluid. Due to

this, the number of vortices shed per cycle increases and contribute towards the thrust force generation of the wing. The study is further carried out by estimating the mean thrust coefficient (C_t) and propulsion efficiency (η_p) of the wing plunging at different k_f.

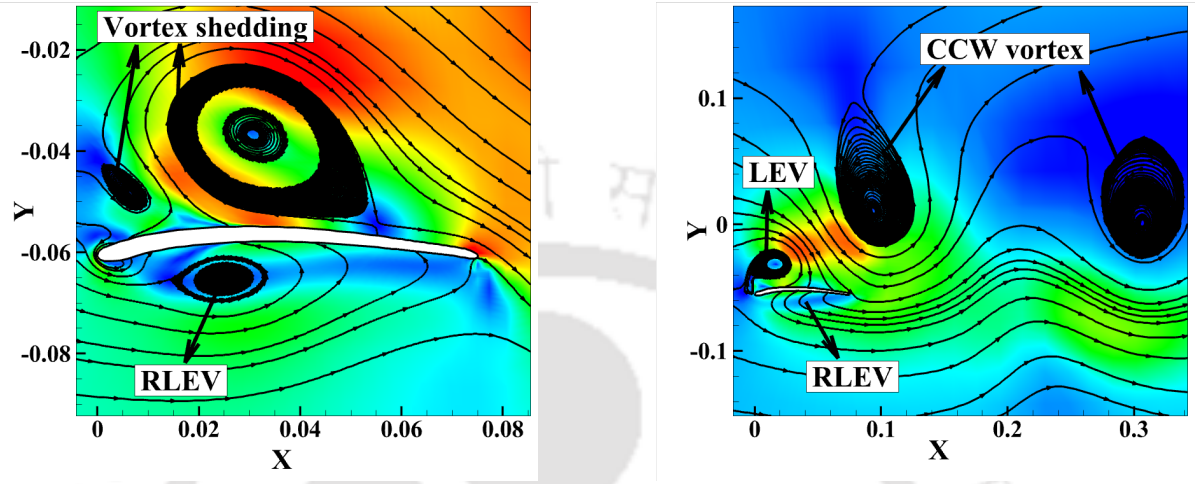

(a) $k_f = 0.5$ (b) $k_f = 2.5$

Figure 6.17: Streamline flow along with contours of velocity magnitude over the biomimetic wing plunging at different k_f at $Re = 5 \times 10^4$ and $\theta_m = 0^\circ$

The variation of C_t and η_p of the wing plunging at $Re = 5 \times 10^4$ with respect to non-dimensional plunge velocity ($k_f h_a$) at different k_f are presented in Fig. 6.15. It is observed that the C_t and η_p increases with respect to k_f for a given value of $k_f h_a$. From the flow field investigations presented in Fig. 6.17, it is observed that, when $k_f \leq 0.5$, the LEV which was formed over the suction side of the wing seems to have detrimental effect on the aerodynamic performance of the wing as it makes hard for the flow to reattach (see Fig. 6.17(a)). As k_f increases to 2.5, the wing plunges faster than that of at $k_f = 0.5$ which increases the interaction between the wing and the surrounding fluid. This allows the flow to reattach as shown in Fig. 6.17(b) and the LEV (after the formation) immediately sheds in the wake region as it doesn't have enough time to fully grow. This minimises the adverse effects of the LEV on the thrust force generation of the wing with respect to increase in k_f. From Fig. 6.17(a) and Fig. 6.17(b), it is also observed that RLEV at $k_f = 2.5$ is not strong as at $k_f = 0.5$. Therefore the negative suction created by RLEV at $k_f = 2.5$ is less than that of at $k_f = 0.5$. Further, from the iso surface of Q-criterion (estimated at Q = 50) of the biomimetic wing plunging at different k_f presented in Fig. 6.18, it is observed that the flow seems to be more attached at higher values of k_f. It is also noticed that the strength of the alternating vortices in the wake at $k_f = 2.5$ is higher than that of at $k_f = 0.5$ which further increases the lift and thrust force coefficients. Due to all these reasons, the C_t and η_p of the wing rises

towards higher values with respect to increase in k_f as shown in Fig. 6.15. The drop in propulsion efficiency after a certain value of $k_f h_a$ as shown in Fig. 6.15(b) is due to the increase in the interference between the vortices shed in the previous cycle and the next cycle. This forms a flat wake structure and affects the η_p of plunging wing after a critical value of $k_f h_a$.

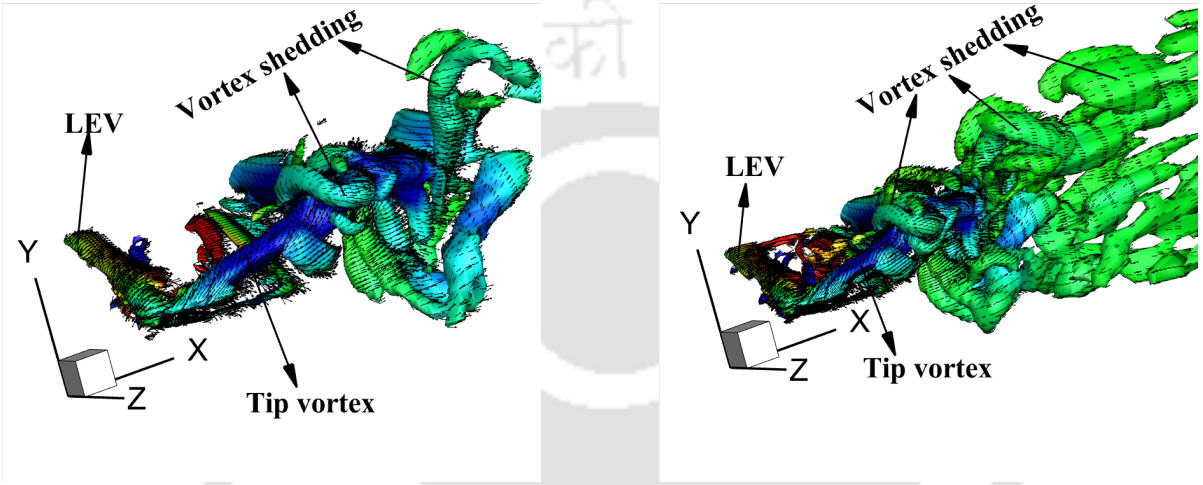

(a) $k_f = 0.5$ (b) $k_f = 2.5$

Figure 6.18: Iso-surface of Q-criterion (Q = 50) of the biomimetic wing plunging at different k_f at $Re = 5 \times 10^4$ and $\theta_m = 0°$

6.3.3 Effect of Reynolds number

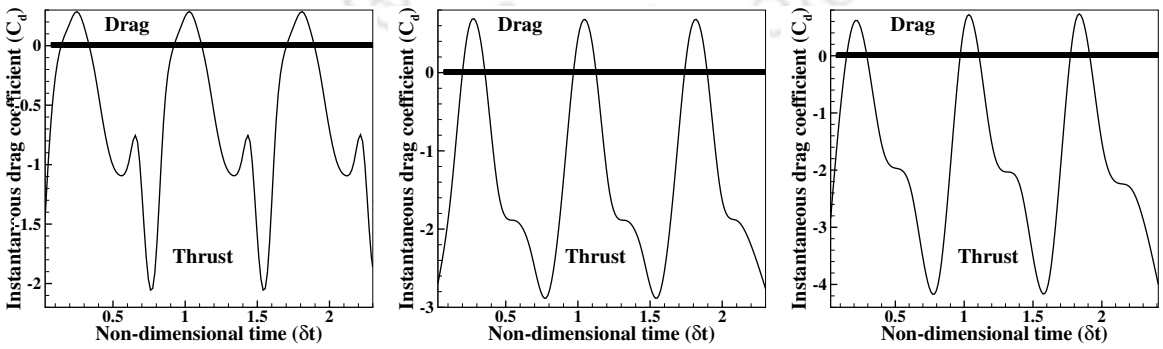

(a) $Re = 2.5 \times 10^4$ (b) $Re = 5 \times 10^4$ (c) $Re = 7.5 \times 10^4$

Figure 6.19: Variation in C_d of the biomimetic wing plunging at different Re with $h_a = 0.1$ and $\theta_m = 0°$

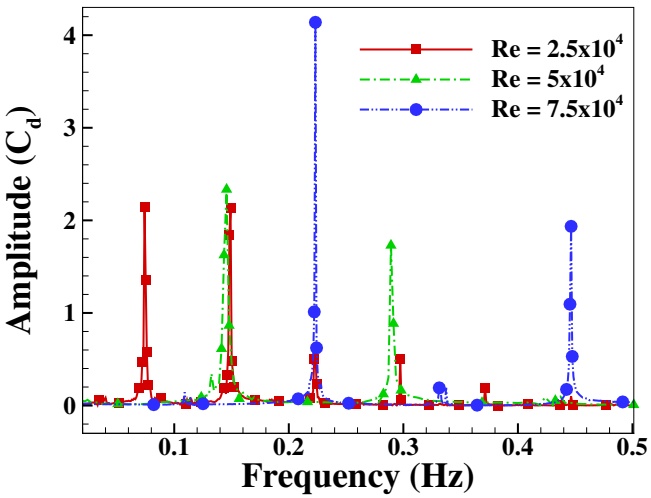

Figure 6.20: Amplitude spectrum of C_d of the biomimetic wing plunging at different Re with $h_a = 0.1$ and $\theta_m = 0°$

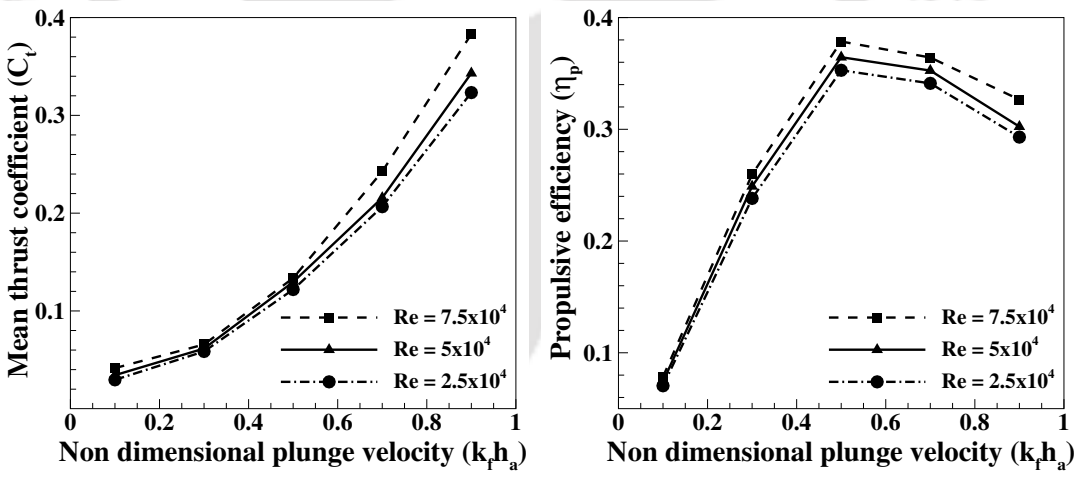

(a) Variation of thrust coefficient (b) Variation of propulsion efficiency

Figure 6.21: Aerodynamic performance of the biomimetic wing plunging at different Re with $h_a = 0.1$ and $\theta_m = 0°$

To analyse the influence of the Reynolds number (Re) on the aerodynamic performance of biomimetic wing subjected to plunging motion, the numerical study is further carried out at three different Re ranging from 2.5×10^4 to 7.5×10^4 in steps of 2.5×10^4 at constant values of $h_a = 0.1$ and $\theta_m = 0°$. The variation in instantaneous drag coefficient (C_d) of the wing plunging at different Re is presented in Fig. 6.19. The variation of C_d curve is periodic and non-sinusoidal. The deviation from the sinusoidal nature of C_d curve is different at different Re. It is observed that the negative values of drag increases with increase in Re. This indicates an increase in thrust force generation with respect to Re

which can also be observed from amplitude spectrum of C_d as shown in Fig. 6.20. From Fig. 6.20, multiple frequency peaks are observed at $Re = 2.5\times10^4$ which indicates the formation of the number of vortices over the wing surface are higher than that of at $Re = 5\times10^4$ and 7.5×10^4.

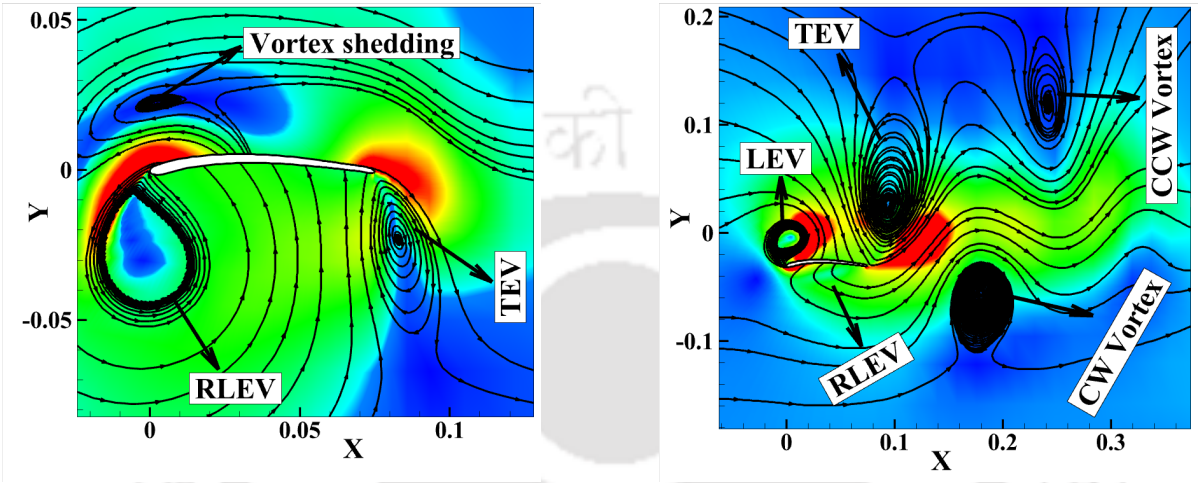

(a) $Re = 2.5 \times 10^4$ (b) $Re = 7.5 \times 10^4$

Figure 6.22: Streamline flow field along with velocity magnitude plot around the biomimetic wing plunging at different Re with $h_a = 0.1$ and $\theta_m = 0°$

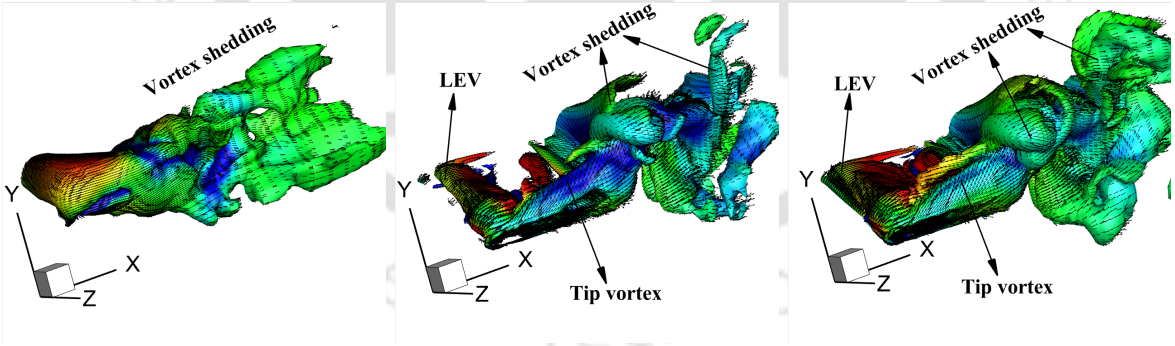

(a) Re $= 2.5 \times 10^4$ (b) Re $= 5 \times 10^4$ (c) Re $= 7.5 \times 10^4$

Figure 6.23: Iso surface of Q-criterion (Q = 50) of the biomimetic wing plunging at different Re with $h_a = 0.1$ and $\theta_m = 0°$

The variation in mean thrust coefficient (C_t) and propulsion efficiency (η_p) at different Re is presented in Fig. 6.21. It is observed that the C_t curve rises towards positive values with respect to increase in $k_f h_a$ for a given Re. It is also noticed that η_p also shows similar trend as that of C_t upto a certain value of $k_f h_a$ and drops with further increase in $k_f h_a$. To understand the reasons behind such behavior, the flow around the wing at different

Re is analysed and presented in Fig. 6.22 and Fig. 6.23 respectively. From the flow field investigations as shown in Fig. 6.22, it is observed that, the increase in C_t and η_p with increase in $k_f h_a$ is due to both LEV and TEV shedding at a given Re. From Fig. 6.21, it is also observed that the C_t and η_p increases with increase in Re for a given $k_f h_a$. This is due to the decrease in flow separation with increase in Re which can be observed by comparing Fig. 6.22(a) and Fig. 6.22(b). Also, it is observed that the strength of the TEV increases with increase in Re which overcomes the adverse effects of LEV (see Fig. 6.22(b)). From the iso surface of Q-criterion (calculated at Q = 50), presented in Fig. 6.23, a more prominent shedding of alternating vortices into the wake region is observed with respect to Re. It is also noticed that the strength of the vortices in the wake region increases with increase in Re. Due to these reasons, a rise in C_t and η_p are observed with respect to Re as shown in Fig. 6.21. The drop in η_p after a critical value of $k_f h_a$ as shown in Fig. 6.21(b) is due to the formation of flat and finite width of the wake due to the interaction between the alternating vortices.

6.4 Summary and conclusions

The unsteady flow characteristics of biomimetic wing subjected to the plunging motion are investigated with the dimensions and conditions corresponding to that of a Micro air Vehicle (MAV). The effect of dimensionless plunge amplitude (h_a), reduced frequency (k_f) and the influence of Re regime with respect to non-dimensional plunge velocity ($k_f h_a$) on the coefficient of thrust force generation (C_t) and propulsion efficiency (η_p) of the wing are thoroughly investigated. To understand the reasons behind the positive thrust force generation, the flow over the wing is further analysed. A reasonable explanation to the current findings is obtained by comparing with the findings reported in the literature. From the current findings, when $h_a \geq 0.3$ in combination with $k_f h_a \leq 0.5$, lower values of C_t and η_p are observed since the major portion of the plunging cycle suffers with flow separation. However, at $h_a \leq 0.1$ in combination with $0.1 \leq k_f h_a \leq 1$, the separated flow reattaches approximately at quarter chord location due which a rise in the C_t and η_p is observed. Therefore, an enhancement in the C_t and η_p of the wing can be observed by maintaining these conditions. It is also noticed that, when $k_f \leq 0.5$, the LEV which was formed due to flow separation at the leading edge has detrimental effects over the aerodynamic performance of the wing. By maintaining $k_f \geq 1.5$ in the range of $0.5 \leq k_f h_a \leq$, the LEV on the pressure side doesn't have enough time to grow and unable to convect farther downstream. Under these conditions, the LEV which was formed over the suction side provides extra suction which can improve the aerodynamic performance of the wing. By analysing the influence of Re ranging from 2.5×10^4 to

7.5×10^4, it is observed that vortex shedding from both leading edge and trailing edge is responsible for the thrust force generation. When $Re \leq 2.5 \times 10^4$, the increase in adverse interaction between LEV and TEV causes multiple peaks in the amplitude spectrum of C_d than that of other Re regimes. By maintaining $Re \geq 5 \times 10^4$ combined with $0.3 \leq k_f h_a \leq 1$, rise in instantaneous force coefficients is observed.

Chapter 7

Aerodynamic Investigation of the Biomimetic Wing Subjected to Flapping Motion

This chapter presents the investigation of aerodynamic performance of the biomimetic wing subjected to flapping motion. The flapping motion in the present study is defined as the combination of rotation about the axis (ξ(t)) along the wing's chord and the rotation about the axis (α(t)) along the semi span of the wing with a phase difference (ϕ(t)).The influence of the dimensionless flapping amplitude, non-dimensional flapping frequency and mean angle of attack on the propulsive performance of the biomimetic wing performing flapping motion are investigated. In order to systematically understand the influence of these parameters over the aerodynamic performance of the biomimetic wing, the flow field around the wing is also further investigated. An asymmetric variation of instantaneous force coefficients is observed despite of having symmetrical flapping kinematics. It is observed that the investigated parameters affect the instantaneous force coefficients both quantitatively and qualitatively. From the flow field investigations, a thrust producing reverse Karman street is observed under certain conditions. It is observed that the formation and the convection of the Leading edge vortex (LEV) not only influences the drag-thrust transition but also the wake pattern. It is also observed that the adverse effects of the LEV can be controlled by controlling aforementioned flow parameters which can improve the mean thrust coefficient and propulsion efficiency of the wing.

7.1 Introduction

In general, the flapping wings are energy efficient and provide high manoeuvrability than that of fixed or rotary wings at low speeds [143]. A number of numerical and experimental studies are reported on investigation of the thrust force generation of the wing undergoing different motions such as: pitching, plunging and a combination of rotation about the axes along the wing chord and span [144, 131, 145, 146, 147, 148, 149]. Hover et al [150] carried out experimental investigations on two dimensional oscillating NACA 0012 airfoil at $Re = 3 \times 10^4$ with $0.2 \leq St \leq 0.8$. Their investigations revealed that, by modifying the flapping kinematics in a way that the resultant angle of attack leads to the path of a square wave form or cosine wave form would enhance the thrust force generation. It was also reported that the change in the resultant angle of attack would influence the wake structures from drag producing to thrust generating. However, the flow field investigations around the airfoil is not provided and in depth analysis on thrust force enhancement is required. Also, the square wave form of resultant angle of attack profile studied by Hover et al [150] has a limitation of presence of sharp corners which may rapidly vary the acceleration of the airfoil during flapping motion. Dash et al [151] carried out numerical and experimental investigations on two dimensional elliptical airfoil undergoing flapping motion at $Re = 5000$ with $0.1 \leq St \leq 0.9$ and the amplitude of effect angle of attack varied from 10° to 20°. They have reported that, at lower frequencies, the variation in thrust force generation is almost negligible with respect to the resultant angle of attack. But observed a considerable amount of enhancement in the thrust force generation with respect to the angle of attack at higher flapping frequencies. However, they had shown less attention towards the flow field investigations. Ramamurthi and Sandberg [3] carried out numerical studies on NACA 0012 airfoil undergoing flapping motion to investigate the unsteady flow past the airfoil at $Re = 1.1 \times 10^3$. They have reported that the maximum values of thrust coefficient and propulsion efficiency can be obtained if the phase angle between pitching and plunging is 120° and 90° respectively. Their investigations are limited only to study the effect of phase angle on the aerodynamic performance of flapping NACA 0012 airfoil. Karbasian and Esfahani [152] investigated on aerodynamic performance of NACA 0012 airfoil during flapping motion at $Re = 4 \times 10^4$ and reported about 20% improvement in the propulsion efficiency at $St = 0.3$.

Most of the studies considered the two dimensional scale models instead of actual three dimensional models to investigate the complexity of the flow field at different types of flapping conditions. This approach saves lot of computational time however, the only drawback is that, the two dimensional approximations consider only the cross-flow component of the vorticity. This leads to the overestimation of the mean propulsion

efficiency of actual three dimensional model due to the underestimation of energy losses in the wake region. From the literature, it is observed that very little attention is devoted towards the actual three dimensional models and most of the models are commercially opted wing planforms such as: Rectangular, trapezoidal and elliptical. The numerical approach and the findings of this chapter is an attempt to address these shortcomings of the literature. In the present numerical investigations, the biomimetic wing is considered (the modelling of the wing is presented in the section 4.2.1) undergoing flapping motion at low Reynolds number (Re) regime ($Re = 5 \times 10^4$). The flapping motion of this study is defined as the combination of rotation about the axis along the wing's chord (ξ(t)) and the rotation about the axis along the semi span of the wing (α(t)) with a phase difference (ϕ(t)). The influence of the parameters like flapping amplitude, non-dimensional flapping frequency and mean angle of attack on the propulsive performance of the biomimetic wing during flapping motion are investigated. The flow field characteristics of the wing at low Re regime are also discussed in order to analyse the viscous phenomenon of the fluid on the propulsive performance of the flapping wing at low Re.

7.2 Method

7.2.1 Problem definition

The discussions regarding the inertial coordinate system OXYZ and the local coordinate system $OX^1Y^1Z^1$ are already presented in section 5.2.1 of Chapter-5. While hovering, the bird's wing has three degree of freedom in which the motion normal to the direction of the flapping plane is relatively small and can be neglected. Therefore, the overall flapping motion of the wing can be approximately discretised into the combination of rotation about the axis along the wing's chord and span. In the present study, the rotation about the axis along the wing span is given by $\alpha(t)$ which can also be described as local pitching along OX^1 axis, defined in Eq. (5.1) of section 5.2.1. In this chapter a constant value of pitching amplitude ($\alpha_p = 5°$) is provided. The rotation about the axis along the wing chord (OZ^1 axis) is shown in Fig. 7.1 and expressed in terms of $\xi(t)$, presented in Eq. (7.1). The direction of the fluid flow is along OX axis.

$$\xi(t) = \theta_m + \alpha_f \sin\left((2\pi f t) + \phi_d\right) \tag{7.1}$$

where θ_m is the mean angle of attack, α_f is the flapping amplitude, f is the flapping frequency and ϕ_d is the phase difference between rotations about the axis along the wing chord and span.

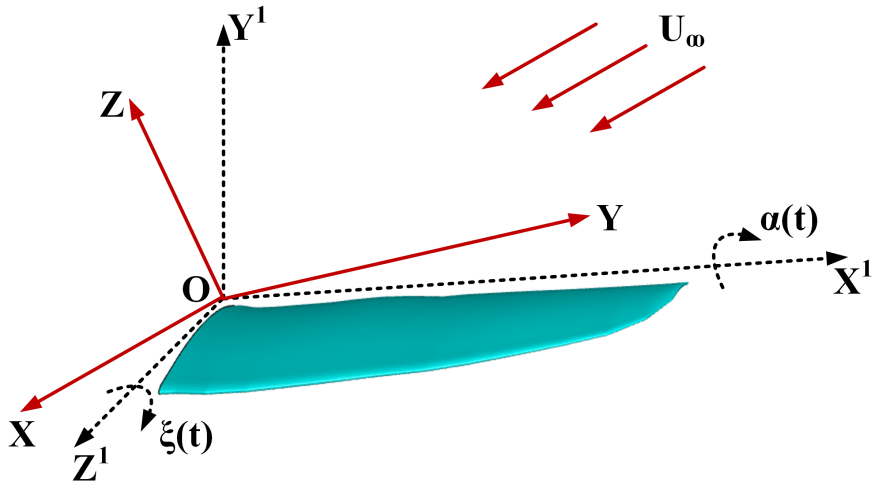

Figure 7.1: Schematic view of the biomimetic wing subjected to flapping motion

7.2.2 Computational details

7.2.2.1 Domain independence test

Table 7.1: Comparison of lift and drag coefficients of biomimetic wing with respect to different domains flapping at $k_f = 3.5$ with $Re = 5 \times 10^4$, $\alpha_f = 5°$, $\theta_m = 0°$ and $\phi_d = 45°$

Domain	Radius(r_1)	Distance (x_1)	Avg.C_l	Error(%)	Avg.C_d	Error(%)
Type 1	25C	50C	0.4459	–	-0.0542	–
Type 2	50C	100C	0.4447	0.27	-0.0538	0.73
Type 3	75C	150C	0.4441	0.13	-0.0536	0.37

The details of the computational domain and generation of the structured mesh are already discussed in the section 4.2.2.1. A compiled User Defined Function (UDF) is developed using Eq. (7.1) and Eq. (5.1) to perform the flapping motion with respect to the incoming viscous flow. The smoothing and remeshing methods are opted to update the mesh during each time step. An initial time refinement study is performed at time steps ($t^* = 5{\times}10^{-3}$ s, $1{\times}10^{-3}$ s, $5{\times}10^{-4}$ s and $1{\times}10^{-4}$ s) with 35 iterations in each time-step, in order to fix the size of the time step (t^*) of each simulation. It is observed that the instantaneous force coefficients doesn't show any variation for $t^* = 5{\times}10^{-4}$ s and $1{\times}10^{-4}$ s. Therefore, the time step size is fixed at $t^* = 5{\times}10^{-4}$ s for all the simulations. In order to verify the variation in the results with respect to dimensions of the fluid domain, an initial domain independence test is carried out on three different domains. The details of the domain dimensions along with the obtained findings of average lift and drag coefficients are presented in Table 7.1. The error percentage in Table 7.1 is obtained from the findings of two consecutive domains. The variation in the instantaneous lift

(C_l) and drag coefficients (C_d) of biomimetic wing flapping at $k_f = 3.5$, $\alpha_f = 5°$, $\theta_m = 0°$ and $\phi_d = 45°$ is presented in Fig. 7.2. It is observed that, the variation in C_l and C_d is almost negligible with respect to the dimensions of the domain. However, at higher flapping frequencies (when $k_f \geq 5$), the reversed flow is observed at the pressure outlet for certain number of time steps during the simulation for Type 1 domain. Therefore, to avoid the influence of outer boundaries, the Type 2 domain dimensions (as shown in Table 5.1) are opted for the current numerical study and the reversed flow doesn't appear in any of the simulations.

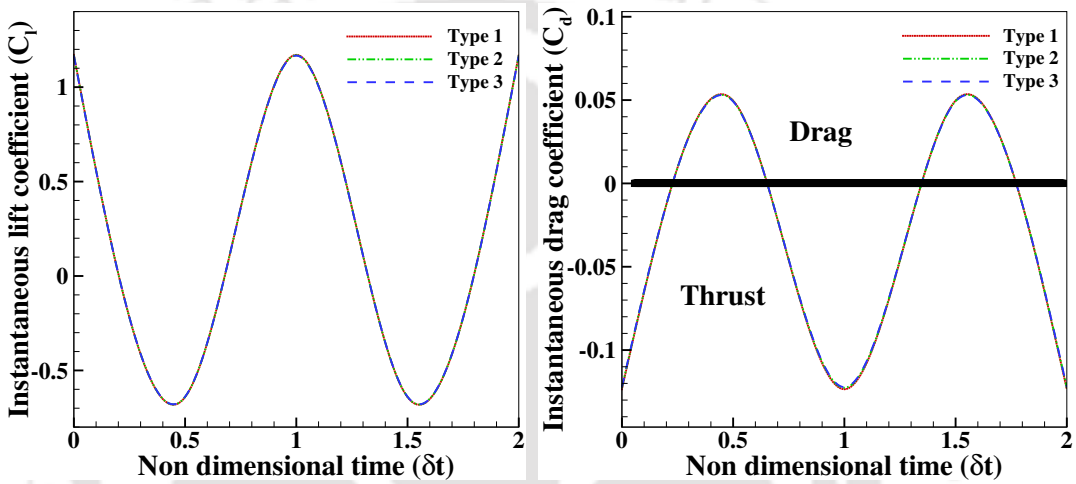

(a) Lift coefficient (b) Drag coefficient

Figure 7.2: Variation of instantaneous force coefficients of biomimetic wing flapping at $k_f = 3.5$ with $Re = 5 \times 10^4$, $\alpha_f = 5°$, $\theta_m = 0°$ and $\phi_d = 45°$

7.2.2.2 Grid independence

In order to investigate the sensitivity of the results with respect to grid size and quality, three grids of different sizes and different qualities are considered. (as shown in Table 7.2). The numerical investigations are carried out to analyse the instantaneous force coefficients of the biomimetic wing flapping at $Re = 5 \times 10^4$ with $k_f = 3.5$, $\alpha_f = 10°$, $\theta_m = 0°$ and $\phi_d = 45°$. The findings obtained using above mentioned conditions with respect to mesh size and quality are presented in Table 7.2. The error percentage is calculated using the findings obtained between two consecutive grids. The variation of the instantaneous lift and drag coefficients of biomimetic wing undergoing flapping motion with respect to the three different grids are presented in Fig. 7.3. It is observed that the Grid 1 predicts slightly higher values than that of Grid 2 and Grid 3. It is also observed that the variation of findings between Grid 2 and Grid 3 is also negligible. Therefore, the Grid 2 configuration is opted for further numerical studies, since the total

number of elements in Grid 2 are somewhat lesser than that of Grid 3. This gives a slight edge in total computational time during each simulation.

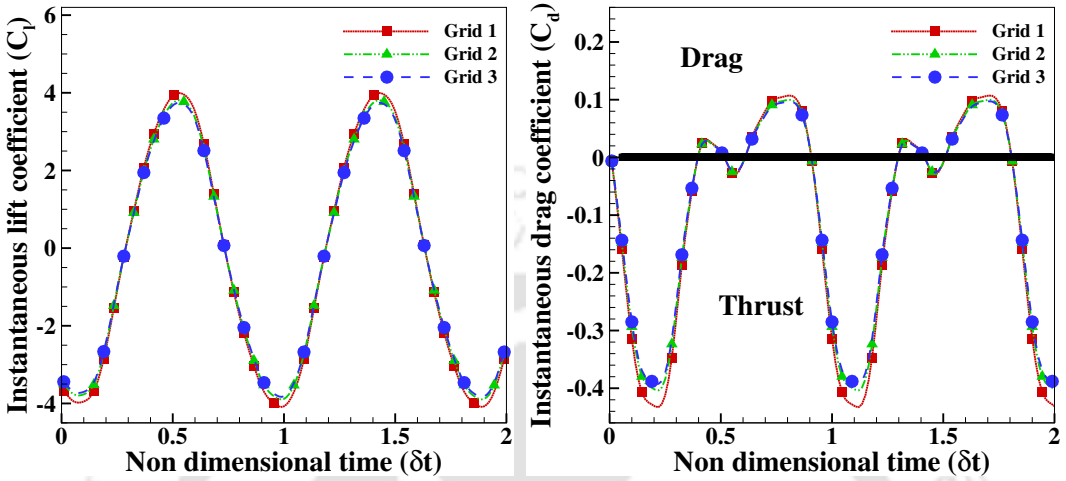

(a) Comparison of instantaneous lift coefficients

(b) Comparison of instantaneous drag coefficients

Figure 7.3: Variation of instantaneous lift and drag coefficients of biomimetic wing with respect to different grids flapping at $Re = 5 \times 10^4$ with $k_f = 3.5$, $\alpha_f = 10^0$, $\theta_m = 0^\circ$ and $\phi_d = 45^\circ$

Table 7.2: Comparison of average lift and drag coefficients of biomimetic wing flapping at $Re = 5 \times 10^4$ with $k_f = 3.5$, $\alpha_f = 10^\circ$, $\theta_m = 0^\circ$ and $\phi_d = 45^\circ$ using three different grids (Min. OQ refers to the minimum orthogonal quality)

Mesh type	Size	Min. OQ	Avg. C_l	Error(%)	Avg. C_d	Error(%)
Grid 1	18.7×10^5	0.182	0.7978	—	-0.1219	—
Grid 2	41.3×10^5	0.237	0.7605	4.90	-0.1137	7.21
Grid 3	87.4×10^5	0.323	0.7475	1.74	-0.1105	2.8

7.2.2.3 Validation

In order to validate the current numerical approach, three validation studies are carried out. In the first validation study, the instantaneous values of thrust coefficient (C_t^*) and propulsion efficiency (η_p^*) reported by Ashraf et al [6] on NACA 0015 airfoil are considered as a reference. The numerical investigations are performed at $k_f = 2$, $h_a = 0.5$, $\phi_d = 90^\circ$ and $\alpha_f = 15^\circ$ with a free stream velocity of $U_\infty = 0.292$ m/s. The obtained findings are presented in Fig. 7.4. It is observed that the findings of the present study has similar trend as that of the findings reported by Ashraf et al [6].

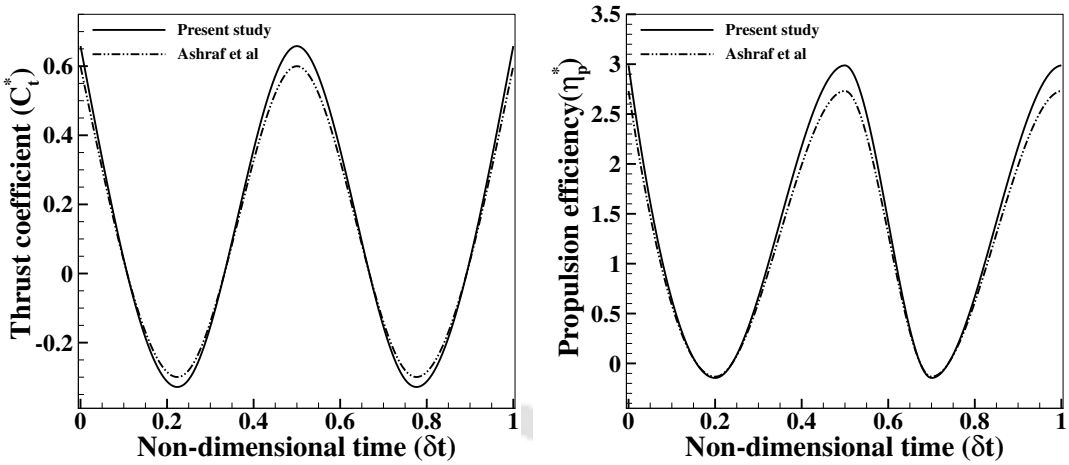

(a) Instantaneous thrust coefficient (b) Instantaneous propulsion efficiency

Figure 7.4: Comparison of aerodynamic performance of NACA0015 airfoil undergoing flapping motion obtained using current numerical approach and findings of Ashraf et al [6] at $k_f = 2$, $\phi_d = 90°$, $\alpha_f = 15°$

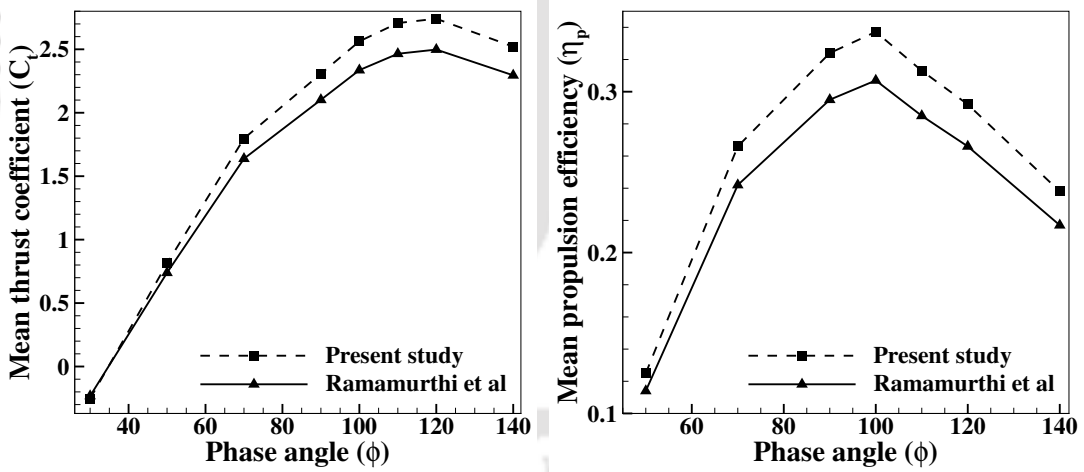

(a) Thrust coefficient (b) Propulsion efficiency

Figure 7.5: Comparision of aerodynamic performance of NACA0012 airfoil undergoing flapping motion obtained using current numerical approach and findings of Ramamurthi et al [3] at $Re = 1.1 \times 10^3$ with $k_f = 0.45$ and $\alpha_f = 30°$

An average error of 9.66% and 9.53%is observed in C_t^* and η_p^* values respectively corresponding to the findings reported by Ashraf et al [6]. In the second validation study, the findings reported by Ramamurthi et al [3] over a range of phase angle ranging from 30° to 140° on NACA 0012 airfoil are considered as a reference. The numerical investigations are carried out on the NACA 0012 airfoil at $Re = 1.1 \times 10^3$ with a flapping frequency of

(k_f) of 0.45 and a flapping amplitude (α_f) of 30°. The mean thrust coefficient (C_t) and mean propulsion efficiency (η_p) of NACA 0012 undergoing flapping motion are obtained and presented along with the findings reported by Ramamurthi et al [3] as shown in Fig.7.5. It is observed that the solver effectively captures the rise and drop in the mean thrust (C_t) and propulsion efficiency (η_p). An average error of 9.75% and 9.79% is observed respectively with respect to the findings reported by Ramamurthi et al [3].

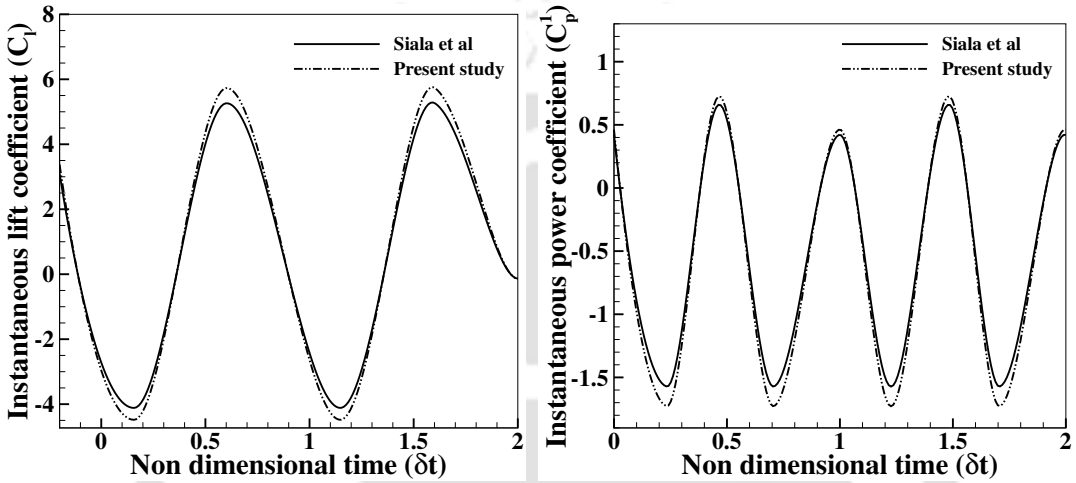

(a) Lift coefficient (b) Power coefficient

Figure 7.6: Comparison of aerodynamic performance of flat plate undergoing flapping motion obtained using current numerical approach and findings of Siala et al [7] at $Re = 4 \times 10^3$ and $St = 0.033$

In the third validation study, the experimental work carried by Siala and Liburdy [7] on a flapping flat plate at $Re = 4 \times 10^3$, $St = 0.033$ with $C = 20$ cm are considered as a reference. The instantaneous values of lift coefficient (C_l) and power coefficient (C_p^1) are estimated using current numerical approach and presented in Fig. 7.6. The obtained findings are compared with the findings reported by Siala and Liburdy [7]. It is observed that a maximum error of 8.87% and 9.89% are observed while calculating C_l and (C_p^1).

In overall, it is observed that the present numerical approach is reliable enough to investigate the aerodynamic performance of the wing subjected to flapping motion.

7.3 Results

7.3.1 Effect of flapping amplitude

The numerical investigations are carried out to analyse the influence of flapping amplitude (α_f) on the aerodynamic performance of the biomimetic wing subjected to flapping

motion.

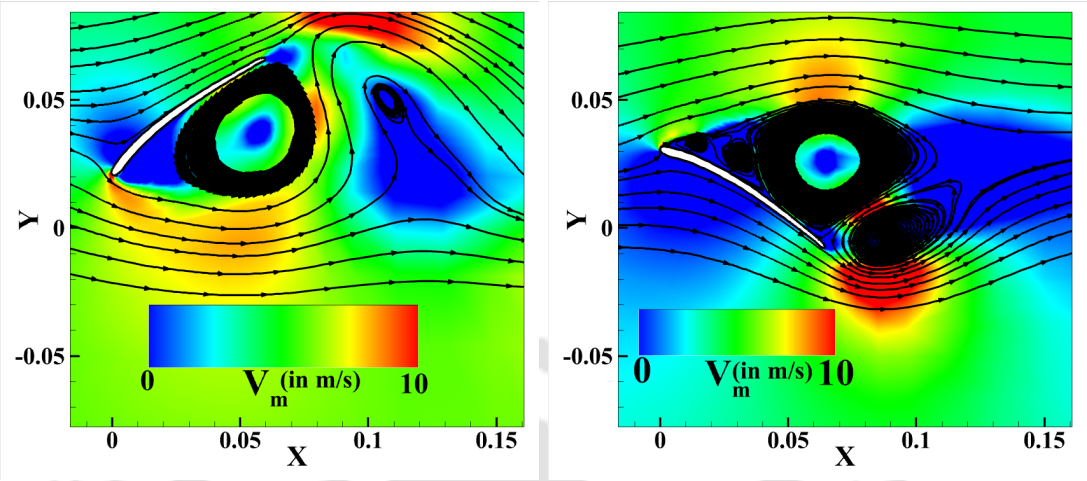

(a) Down stroke (b) Upstroke

Figure 7.7: Contours of velocity magnitude along with stream lines over the biomimetic wing flapping at $Re = 5 \times 10^4$, $k_f = 3.5$, $\alpha_f = 2°$, $\theta_m = 0°$ and $\phi_d = 45°$

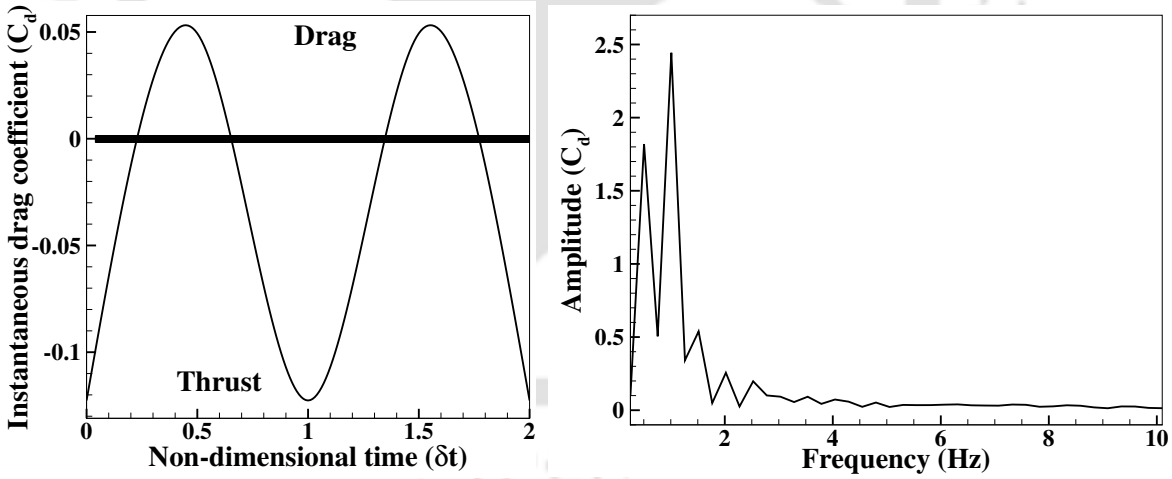

(a) Time domain (b) Frequency domain

Figure 7.8: Variation in C_d of the biomimetic wing flapping at $Re = 5 \times 10^4$, $k_f = 3.5$, $\alpha_f = 5°$, $\theta_m = 0°$ and $\phi_d = 45°$

From the preliminary investigations, at $1° \leq \alpha_f \leq 4°$, it is observed that the major portion of the flapping cycle suffers with large flow separation due to vortex shedding as shown in Fig. 7.7. Therefore, to investigate the effect of flapping amplitude (α_f), the numerical study is carried out by varying α_f from 5° to 15° in steps of 5° by maintaining a constant value of dimensionless flapping frequency (k_f) which is $k_f = 3.5$.

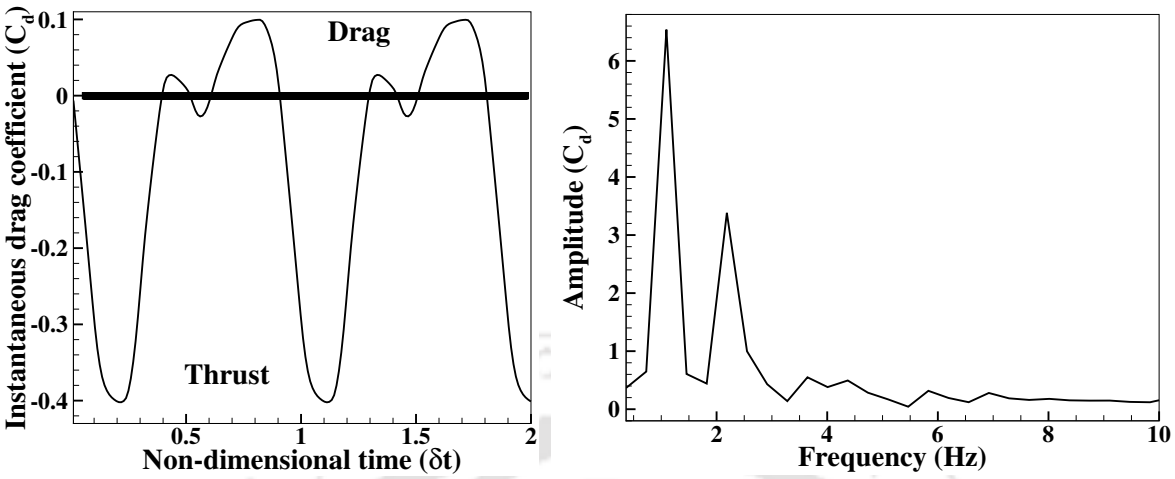

(a) Time domain (b) Frequency domain

Figure 7.9: Variation in C_d of the biomimetic wing flapping at $Re = 5 \times 10^4$, $k_f = 3.5$, $\alpha_f = 10°$, $\theta_m = 0°$ and $\phi_d = 45°$

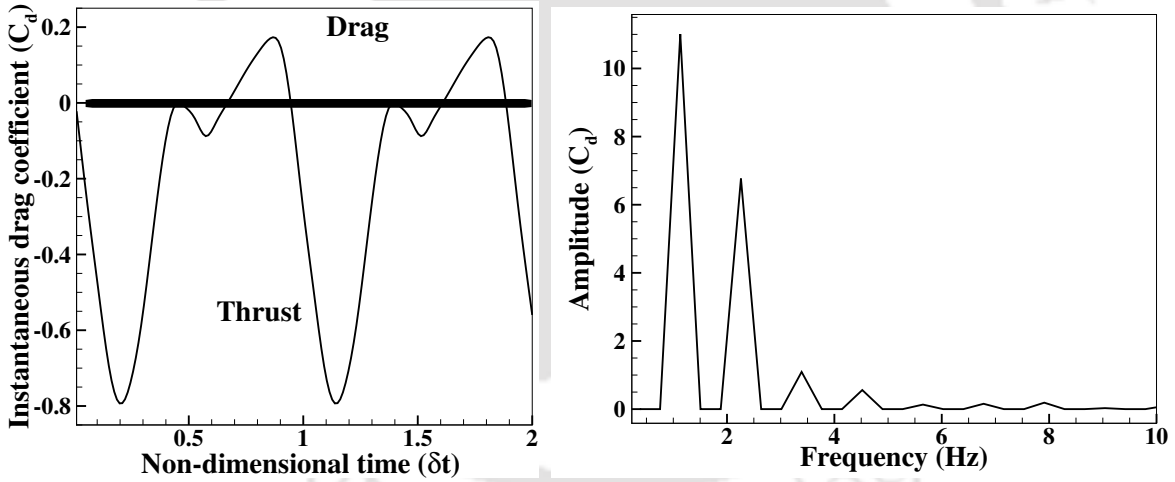

(a) Time domain (b) Frequency domain

Figure 7.10: Variation in C_d of the biomimetic wing flapping at $Re = 5 \times 10^4$, $k_f = 3.5$, $\alpha_f = 15°$, $\theta_m = 0°$ and $\phi_d = 45°$

The variation of instantaneous drag coefficient (C_d) of the biomimetic wing undergoing flapping motion is presented in Fig. 7.8 to Fig. 7.10. It is observed that the C_d curve is sinusoidal and periodic for $\alpha_f = 5°$. As α_f increases beyond 5°, the C_d curve loses its sinusoidal nature (still periodic as shown in Fig. 7.9(a) and Fig. 7.10(a)) due to the formation and convection of the vortices over the wing surface. The negative values of C_d indicates the thrust force generation of the wing which increases with respect to increase in α_f.

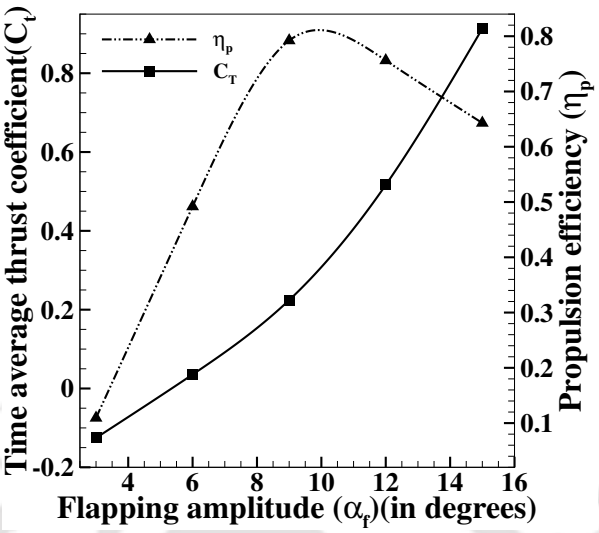

Figure 7.11: Aerodynamic performance of biomimetic wing with respect to α_f flapping at $Re = 5 \times 10^4$, $k_f = 3.5$, $\theta_m = 0°$ and $\phi_d = 45°$

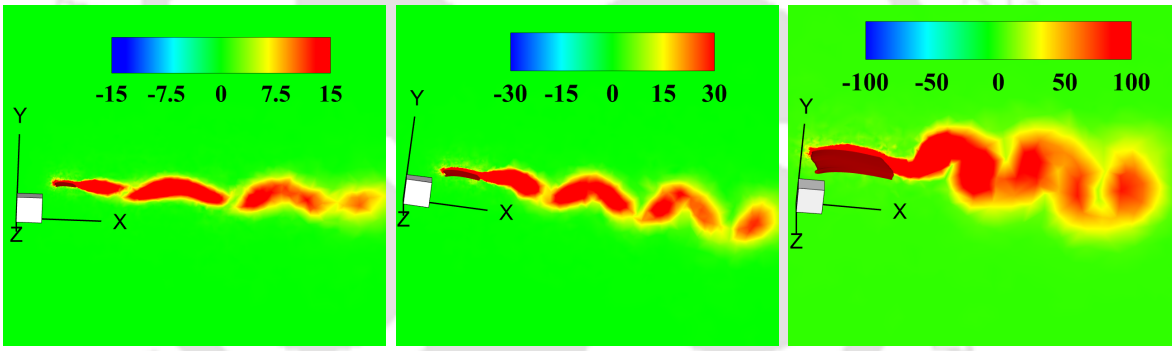

(a) $\alpha_f = 5°$ (b) $\alpha_f = 10°$ (c) $\alpha_f = 15°$

Figure 7.12: Contours of vorticity magnitude (V_z) of biomimetic wing with respect to α_f, flapping at $Re = 5 \times 10^4$, $k_f = 3.5$, $\theta_m = 0°$ and $\phi_d = 45°$

The investigations are further carried out by calculating the amplitude spectrum of the C_d using Fourier transformation algorithm, presented in Fig. 7.8(b), 7.9(b) and 7.10(b) for $\alpha_f = 5°, 10°$ and $15°$ respectively. The spectrum of C_d consists of frequency peaks with different amplitudes. From the flow field investigations, it is observed that the increase in α_f increases the vortex strength in the wake region (see Fig. 7.12). Therefore, the higher and denser harmonics at $\alpha_f = 15°$ indicate that the thrust force generation of the wing in this case is higher than that of when $\alpha_f \leq 10°$. To further analyse the influence of α_f on the aerodynamic performance of the wing, the mean thrust force coefficient (C_t) and the propulsion efficiency (η_p) are calculated using Eq. 5.2 to Eq. 5.5 which are defined in section 5.2.2. The obtained findings are presented in Fig. 7.11.

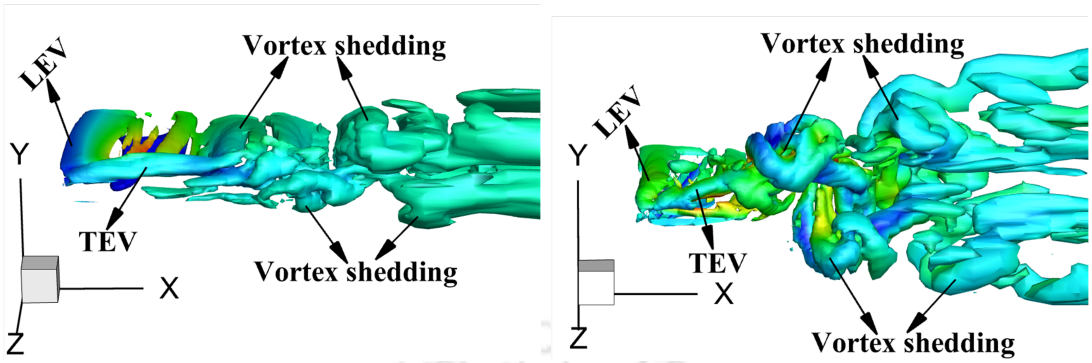

(a) $\alpha_f = 5°$ (b) $\alpha_f = 15°$

Figure 7.13: Iso-surface of Q-criterion at (Q = 250) of biomimetic wing with respect to α_f, flapping at $Re = 5 \times 10^4$, $k_f = 3.5$, $\theta_m = 0°$ and $\phi_d = 45°$

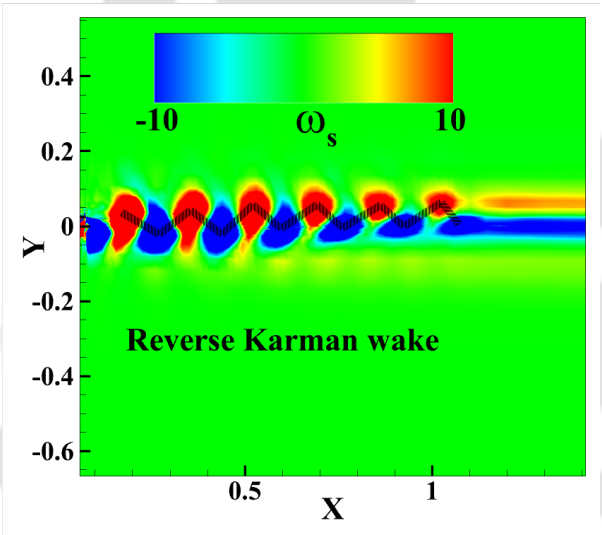

Figure 7.14: Wake pattern of biomimetic wing flapping at $Re = 5 \times 10^4$, $k_f = 3.5$, $\alpha_f = 10°$, $\theta_m = 0°$ and $\phi_d = 45°$

It is observed that C_t increases with respect to increase in α_f. It is also noticed that η_p has shown similar trend as that of C_t upto a certain value of α_f and drops with further increase in α_f. To understand the reasons behind such behaviour, the flow around the wing at different α_f is analysed and presented in Fig. 7.12 and 7.13. From the contours of vorticity magnitude (V_z) presented in Fig. 7.12, it is observed that, increase in α_f increases the strength of the alternating vortices shed into the wake region. This can be noticed from the ranges of V_z provided from Fig. 7.12(a) to 7.12(c). From the iso-surface of Q-criterion (calculated at Q = 250) presented in Fig. 7.13, a more prominent vortex shedding is observed at $\alpha_f = 15°$ compared to that of at $\alpha_f \leq 10°$. From Fig. 7.13, it is also noticed that, increasing α_f increases the wing's influence over

its surrounding fluid and vortex formation happens closer to the wing's surface. This enhances the positive suction and remarkably influences the thrust force generation and the propulsion efficiency of the wing. From the contours of Z-vorticity (ω_z) shown in Fig.7.14, it can be observed that, the dipoles of the positive vortices are slightly above the mean line and the dipoles of the negative vortices fall below the mean line. This indicates the alternating vortices form the thrust producing reverse Karman street in the wake region. However, it is observed that, increasing α_f beyond a certain value increases the interference between the vortices shed in the previous cycle and the next cycle. This forms a flat wake in the wake region with respect to increase in number of flapping cycles, which can be observed from Fig. 7.14 (where the vortices in the wake region loses the alternating pattern and forms a flat wake).

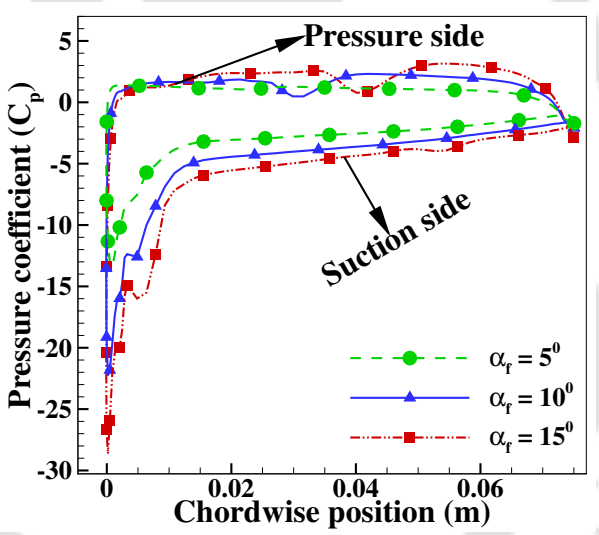

Figure 7.15: Variation of pressure coefficients of biomimetic wing with respect to α_f flapping at $Re = 5 \times 10^4$, $k_f = 3.5$, $\theta_m = 0°$ and $\phi_d = 45°$

This abrupt change in the nature of wake pattern affects the propulsion efficiency of the wing due to which a drop in η_p curve is observed in Fig. 7.11 after a certain value of α_f. However, the C_t curve still rises towards higher values due to increase in the strength of the alternating vortices with respect to α_f. By analysing the pressure coefficients of the wing subjected to flapping motion presented in Fig. 7.15, It is observed that, the wing clearly lacks in extra suction with respect to decrease in α_f. As $\alpha_f \geq 5°$, the difference between the pressure over the suction side and the pressure side increases which is also one of the reasons for the rise in C_t and η_p with respect to α_f as shown in Fig. 7.11.

7.3.2 Effect of mean angle of attack

To investigate the influence of mean angle of attack (θ_m), the study is carried out by varying θ_m from 0° to 12° in steps of 4° with a constant value of $k_f = 3.5$. The variation of instantaneous drag coefficient (C_d) of the wing subjected to flapping motion at θ_m = 4° and 8° is presented in Fig.7.16 and 7.17 respectively. It is observed that the variation of C_d curve is periodic and sinusoidal (with a slight deviation at $\theta_m = 4°$). It is also noticed that the C_d curve rises towards positive values with respect to increase in θ_m. This indicates that the drag offered by the surrounding fluid dominates the thrust force generation of the wing.

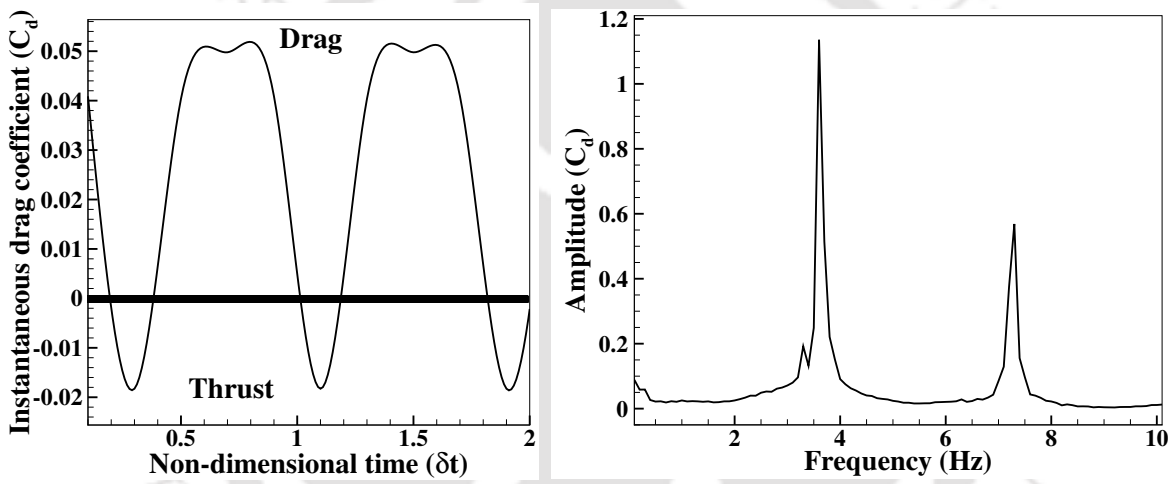

(a) Time domain (b) Frequency domain

Figure 7.16: Instantaneous drag coefficients of biomimetic wing flapping at $\theta_m = 4°$ Re $= 5 \times 10^4$, $\alpha_f = 5^0$, $k_f = 3.5$ and $\phi_d = 45°$

The investigations are further carried out by calculating the amplitude spectrum of C_d using Fourier transform algorithm. The obtained findings at θ_m = 4° and 8° are presented in Fig. 7.16(b) and Fig. 7.17(b) respectively. The frequency peaks at θ_m = 4° shown in Fig.7.16(b) indicates the thrust force generation of the wing. However, the denser and higher peaks in the Fig.7.17(b) indicates dominance of drag over thrust due to the formation of strong vortical structures over the suction side of the wing at $\theta_m = 8°$. To further understand the influence of θ_m over the aerodynamic performance of the wing subjected to flapping motion, the pressure coefficients (C_p) over the wing surface are numerically analysed. The obtained findings of C_p with respect to θ_m are presented in Fig.7.18. It is observed that the suction over the suction side of the wing decreases with increase in θ_m.

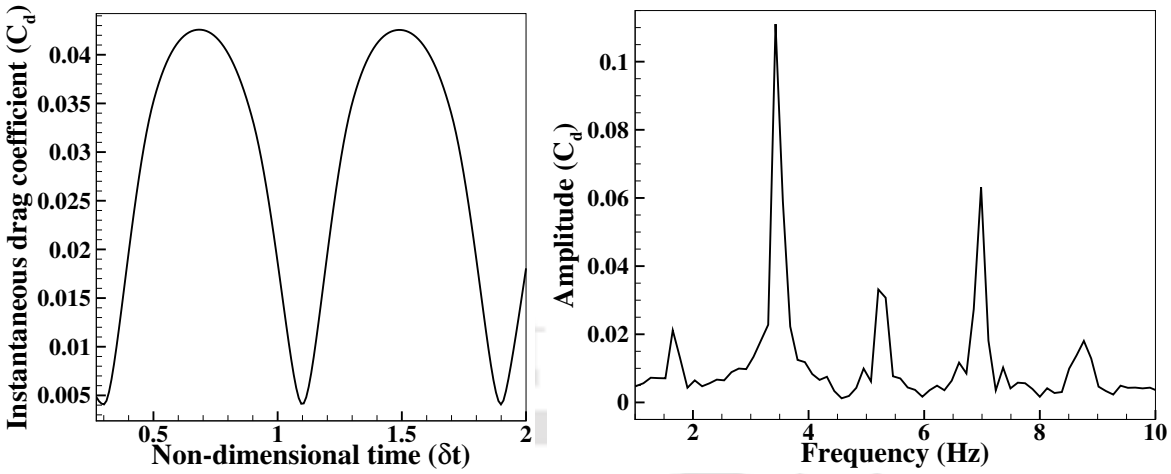

(a) Time domain (b) Frequency domain

Figure 7.17: Instantaneous drag coefficients of biomimetic wing flapping at $\theta_m = 8°$ $Re = 5 \times 10^4$, $\alpha_f = 5°$, $k_f = 3$ and $\phi_d = 45°$

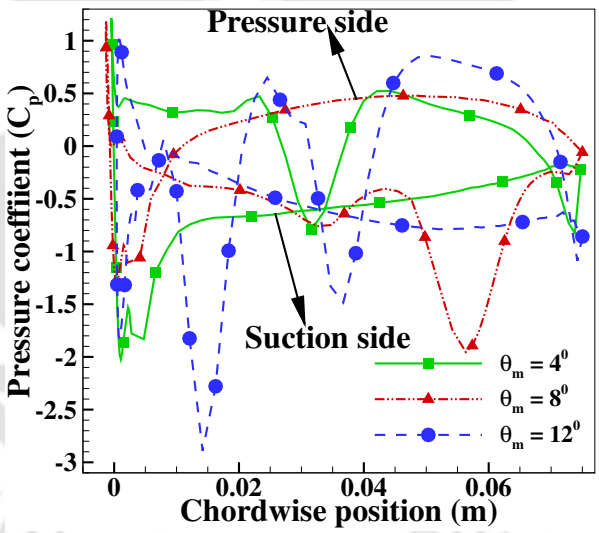

Figure 7.18: Variation in coefficient of pressure of biomimetic wing with respect to θ_m flapping at $Re = 5 \times 10^4$, $\alpha_f = 10°$ and $\phi_d = 45°$

It is also noticed that the fluctuations over the suction side of the C_p curve increases with respect to increase in θ_m. From the flow investigations, it is observed that the fluctuations in the C_p curve is due to the recirculation of the flow over the wing surface. At $\theta_m = 12°$, multiple fluctuations are observed over the pressure side of the C_p curve. This indicates the presence of opposite recirculation due to the formation of vortical structures over the pressure side of the wing. This opposite recirculation causes negative suction which opposes the positive suction created over the suction side of the wing and eventually affects the wing's performance. Further, the investigations are carried out

to estimate the mean thrust force coefficient (C_t) and the propulsion efficiency (η_p) of the wing at different θ_m. The variation of C_t and η_p with respect to θ_m are presented in Fig.7.19. It is observed that the C_t and η_p decreases with increase in θ_m. This is due to formation and convection of multiple vortices over the suction side of the wing (as discussed from Fig.7.18). The negative values of C_t indicates the presence of drag. It is observed that, when $\theta_m \geq 8°$, there is only drag possibly due to massive flow separation with respect to increase in θ_m and the wing doesn't have any influence over its surrounding fluid under these conditions.

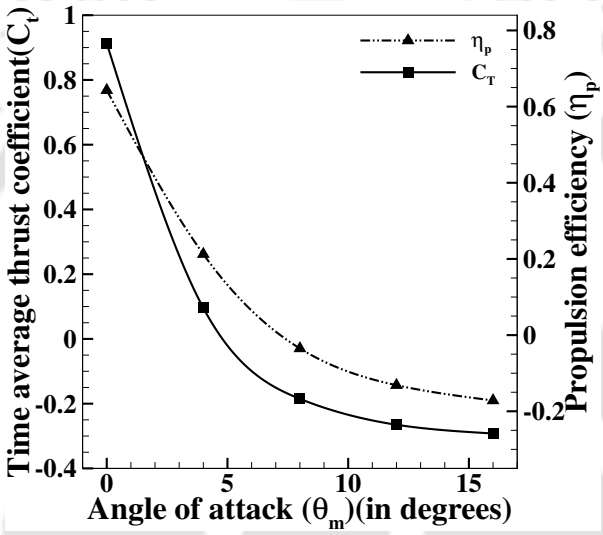

Figure 7.19: Aerodynamic performance of biomimetic wing with respect to θ_m flapping at $Re = 5 \times 10^4$, $\alpha_f = 5°$, $k_f = 3$ and $\phi_d = 45°$

From the flow field investigations, it is observed that the increase in θ_m alters the wake pattern and eventually affects the aerodynamic performance of the wing. Different types of wake patterns are noticed at different θ_m as shown in Fig.7.20. At $\theta_m = 4°$, a paired wake structure is observed in the wake region which consists of a strip shaped positive vortex (sp_2) and a circular shaped negative vortex (cn_2). As the number of flapping cycles increases, the strip shaped positive vortex transforms into a circular shaped positive vortex (cp_2^1) and flows with the circular shaped negative vortex of the previous stroke (cn_2^1) as shown in Fig.7.20(a). It is observed that the distance between the dipoles of the alternating vortices is approximately same ($\delta_1 \simeq \delta_2$) which indicates that the corresponding wake is stable. At $\theta_m = 8°$, the strip shaped positive vortex (sp_1^1) and the strip shaped negative vortex of the previous stroke (sn_1^1) exhibit pure sinusoidal wake. It is observed that the distance between the dipoles of the alternating vortices slightly varies ($\delta_1 \neq \delta_2$) from cycle to cycle. This indicates that the corresponding vortex street is unstable. As θ_m increases beyond 8°, the alternating vortices slowly loose their

sinusoidal nature and exhibit paired vortex structure (PV_1). As the number of flapping cycles increases, this paired vortex structure breaks into a single vortex wake which consists of circular shaped positive vortex (cp_0) and strip shaped negative vortex (sn_0). It is observed that the dipoles of the negative vortices falls above the mean line and the dipoles of the positive vortices are below the mean line. This indicates the formation of drag producing Karman street which is why the negative values are observed in C_t and η_p curves as shown in Fig.7.19 when $\theta_m \geq 8°$.

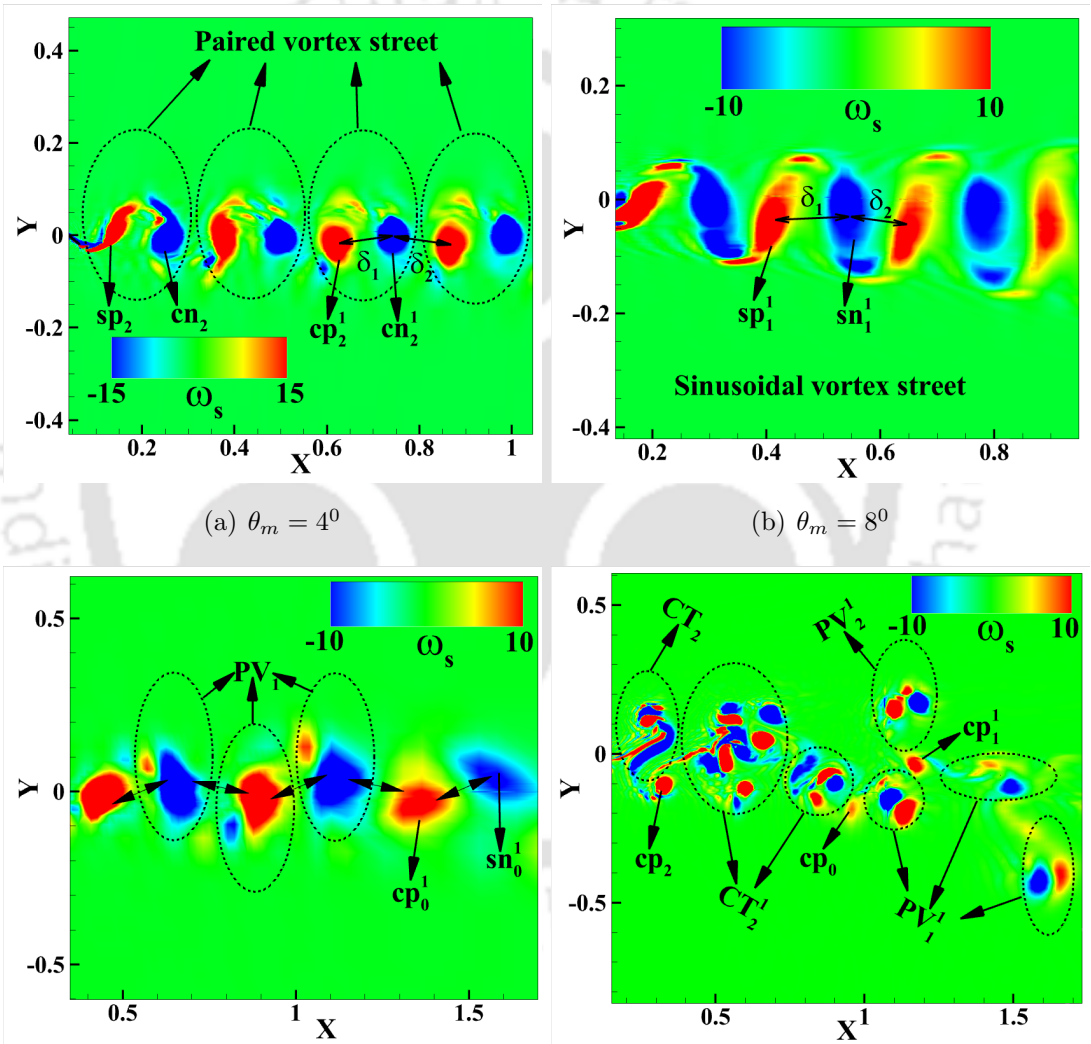

(a) $\theta_m = 4^0$ (b) $\theta_m = 8^0$

(c) $\theta_m = 12^0$ (d) $\theta_m = 16^0$

Figure 7.20: Wake pattern of biomimetic wing with respect to θ_m flapping at $Re = 5 \times 10^4$, $\alpha_f = 5°$, $k_f = 3$ and $\phi_d = 45°$

With further increase in angle of attack, at $\theta_m = 16°$, the alternating vortices of the previous cycle interacts with the vortices of the next cycle (cp_2 and cp_0 are the circular shaped positive vortices of present and previous cycles). As number of flapping

cycles increases, these vortices form clusters (where CT_2 and CT_2^1 refers to the cluster of alternating vortices during current and previous cycle respectively) above and below the mean line in the wake region which further affects the aerodynamic performance of the wing.

7.3.3 Effect of non dimensional flapping frequency

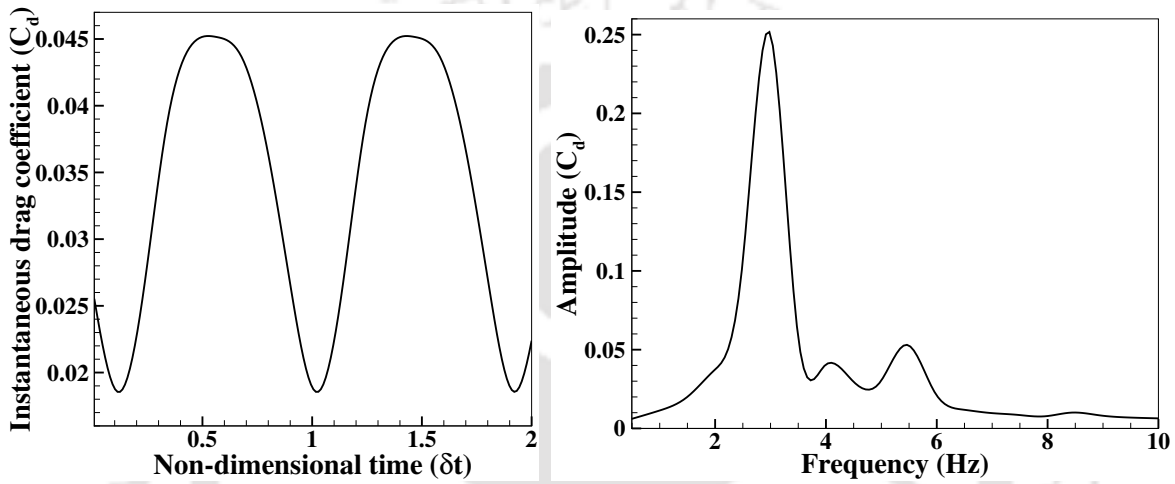

(a) Time domain (b) Frequency domain

Figure 7.21: Instantaneous drag coefficients of biomimetic wing flapping $k_f = 3$ with $Re = 5 \times 10^4$, $\alpha_f = 5°$, $\theta_m = 0°$ and $\phi_d = 45°$

The investigations are further extended to analyse the influence of non dimensional flapping frequency (k_f) on the aerodynamic performance of the biomimetic wing subjected to flapping motion. The preliminary investigations of k_f varying from 1 to 3 reveals that the wing is unable to overcome the viscous drag offered by the surrounding fluid. Therefore the conditions when $k_f \geq 3$ are investigated by varying k_f from 3 to 7 in steps of 2. The variation in instantaneous drag coefficient (C_d) with respect to non-dimensional time at $k_f = 3$ and 7 is presented in Fig.7.21 and 7.22 respectively. It is observed that the variation of C_d is periodic and sinusoidal. At $k_f = 3$, it is noticed that the C_d curve doesn't contain any negative values which indicate that the wing cannot generate positive thrust under these conditions. As k_f increases to 7, it is observed that the wing overcomes the resistance from the surrounding fluid and generates positive thrust. The amplitude spectrum of C_d (obtained using Fourier transform algorithm) at $k_f = 3$ and 7 is presented in Fig. 7.21(b) and 7.22(b) respectively. Multiple frequency peaks are observed at $k_f = 3$ due to vortex shedding indicating the presence of drag during most of the flapping cycle.

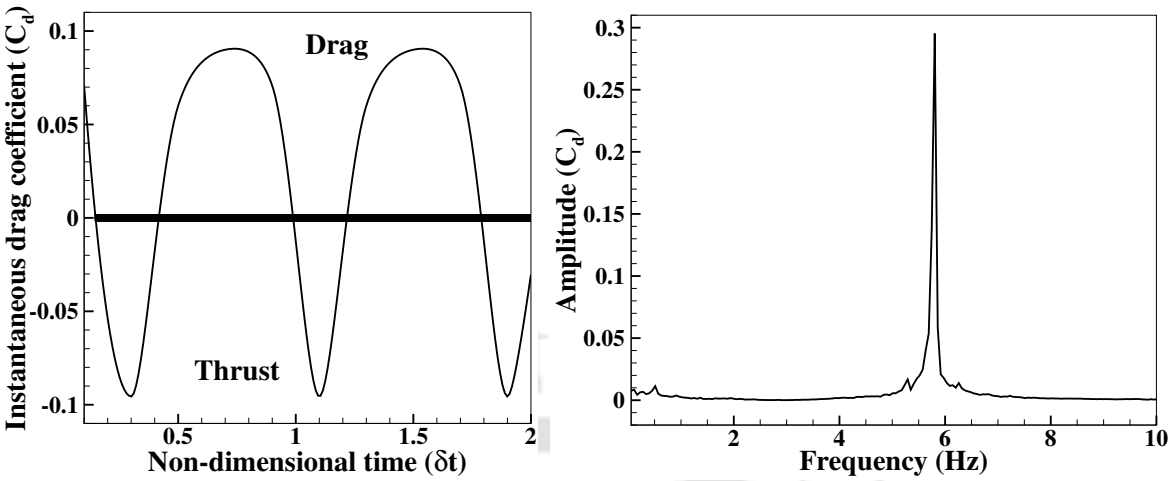

(a) Time domain (b) Frequency domain

Figure 7.22: Instantaneous drag coefficients of biomimetic wing flapping $k_f = 7$ with Re $= 5 \times 10^4$, $\alpha_f = 5°$, $\theta_m = 0°$ and $\phi_d = 45°$

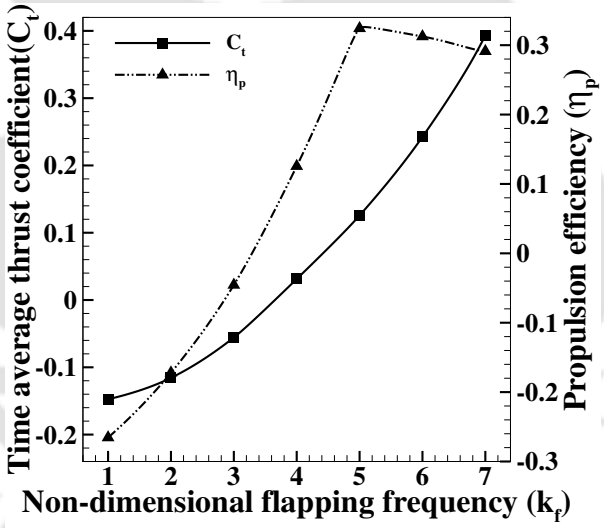

Figure 7.23: Aerodynamic performance of biomimetic wing with respect to k_f flapping at $Re = 5 \times 10^4$, $\theta_m = 0°$, $\alpha_f = 5°$ and $\phi_d = 45°$

However, at $k_f = 7$, the higher and denser peak in the spectrum indicates the thrust force generation of the wing. To further analyse the influence of non dimensional flapping frequency (k_f), the mean thrust coefficient (C_t) and propulsion efficiency (η_p) of the wing are numerically estimated. The obtained findings of C_t and η_p with respect to k_f are presented in Fig. 7.23. The negative values in the C_t curve when $k_f \leq 3$ indicates that the wing is unable to overcome the viscous drag from the surrounding fluid under these conditions. However, further increase in k_f beyond 3, the C_t curve rises towards positive values which indicates the positive thrust force generation of the wing. It is also noticed

that η_p also follows similar trend as that of C_t up to a certain value of k_f and gradually drops with further increase in k_f. To analyse the reasons behind such behavior, the flow around the wing at $k_f = 3$ and 7 are analysed and the obtained findings are presented in Fig.7.24 and Fig.7.25 respectively.

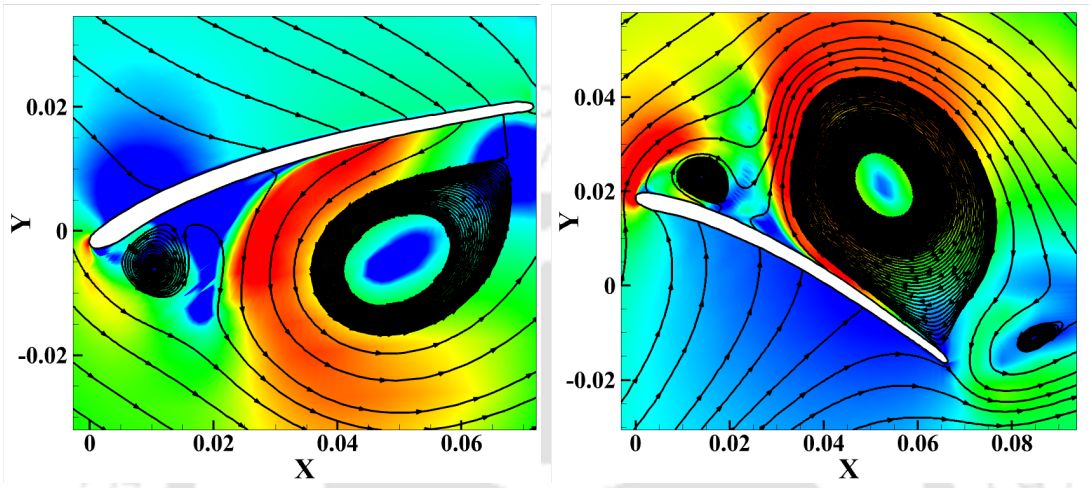

(a) Down stroke (b) Upstroke

Figure 7.24: Contours of velocity magnitude (V_m) ranging from 1 m/s to 10 m/s along with the stream line plots around the biomimetic wing flapping at $k_f = 3$, $Re = 5 \times 10^4$, $\alpha_f = 5°$, $\theta_m = 0°$ and $\phi_d = 45°$

From the flow field investigations at $k_f = 3$ presented in Fig. 7.24, it is observed that the flow is fully attached over the suction side of the wing during down stroke as shown in Fig. 7.24(a). However, the flow separation over the pressure side of the wing forms strong vortices with oppositely rotating nature which oppose the suction created over the suction side. The rise in the instantaneous force coefficients can be observed once these vortices shed into the wake region. During upstroke as shown in Fig. 7.24(b), massive recirculation of the flow over the suction side of the wing is observed which makes it hard for the separated flow to reattach. Due to this the instantaneous force coefficients drops during this period of the flapping cycle. In overall, it is noticed that the whole flapping cycle suffers with large flow separation due to the formation and convection of the aforementioned vortical structures. Because of these reasons, the wing is unable to generate positive thrust at $k_f = 3$ in combination with $\alpha_f = 5°$ which is why the negative values of C_t and η_p are observed in Fig. 7.23 when $k_f \leq 3$. The flow over the wing surface at $k_f = 7$ is presented in Fig. 7.25. From Fig. 7.25(a), it is observed that the flow is fully attached over the wing surface. The suction created due to the formation of Leading Edge Vortex (LEV) can be observed along the semi span of the wing. It must be noted that, as k_f increases, the time period of the cycle decreases. Due

to this, the LEV doesn't have enough time to travel farther downstream. This limits the detrimental effects of the LEV on the aerodynamic performance of the wing.

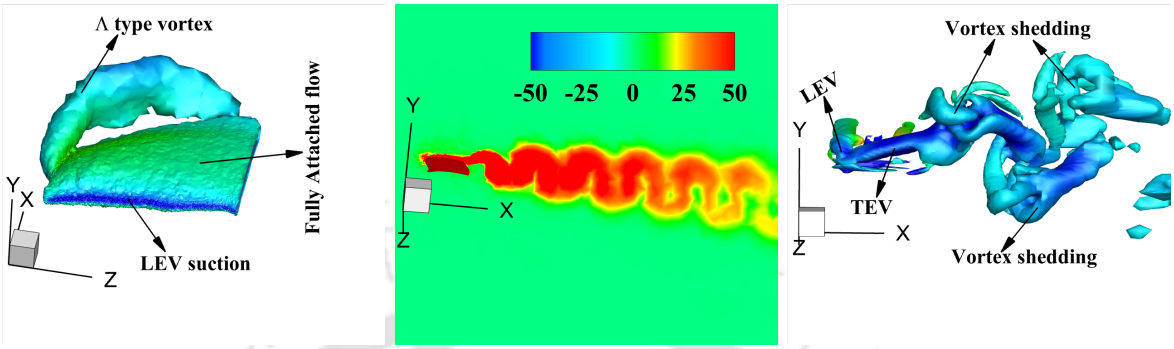

(a) Iso surface of vorticity magnitude (at $V_z = 50$)

(b) Contours of vorticity magnitude

(c) Iso surface of Q-criterion (at Q = 100)

Figure 7.25: flow field investigation of biomimetic wing flapping at $k_f = 7$, $Re = 5 \times 10^4$, $\alpha_f = 5°$, $\theta_m = 0°$ and $\phi_d = 30°$

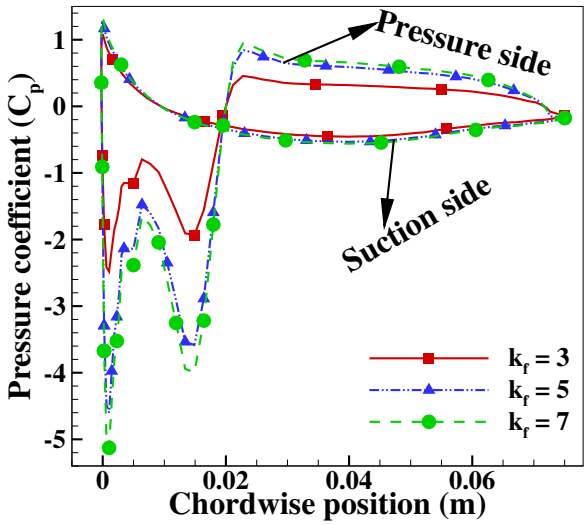

Figure 7.26: Pressure coefficient variation of biomimetic wing with respect to different flapping frequencies (k_f) with $Re = 5 \times 10^4$, $\alpha_f = 5°$, $\theta_m = 0°$ and $\phi_d = 45°$

From the overall investigations, it is observed that when $k_f \leq 3$, the dissipation of the induced vortices in the fluid is gradual and the intensity of these vortices is weak. As k_f increases beyond 3, the number of vortices shed per given flapping cycle increases and interact with the vortices shed with the previous flapping cycle. This local interaction of the induced vortices not only increase the velocity of the fluid but also change the diffusion angle of the vortices in the downstream. This affects the arrangement of the vortices in the wake region and alters the vortex street from the drag inducing Karman

Vortex to thrust producing Reverse Karman Vortex. It is observed that the further increase in non-dimensional flapping frequency gradually increase the intensity of the vortices however the interference between the leading and trailing edge vortices also increases. This leads to the formation of more complex and irregular vortices in the wake region. This inevitably affects the propulsion efficiency (η_p) of the wing which drops with further increase in k_f. From the findings, it is observed that the $k_f = 5$ is the critical value of the non-dimensional flapping frequency after which η_p drops with further increase in k_f.

From Fig. 7.25(a), it is observed that the flow leaves the trailing edge of the wing by forming arch ($\wedge$) type vortex. As the number of flapping cycles increases, these vortices shed into the wake region exhibiting alternating pattern as shown in Fig. 7.25(b) and Fig. 7.25(c). However, when k_f increases beyond a certain value (greater than 5 in this case), it is observed that the interaction between alternating vortices of previous and present cycle increases. This forms a flat pattern in the wake with respect to increase in the number of cycles (as shown in Fig.7.14). Due to this, a drop in η_p curve is noticed in Fig. 7.23 when k_f greater than 5. The investigations are further extended to numerically analyse the variation in the pressure coefficient (C_p) of the wing at different k_f. The obtained findings of C_p with respect to k_f are presented in Fig.7.26. It is observed that the fluctuations in the C_p curve over the suction side is due to the LEV formation at the leading edge and its convection towards the trailing edge. It is also noticed that the suction over the suction side of the wing increases with respect to increase in k_f. This is due to the increase in the number of vortices shed per cycle which increases the velocity in the direction of flow and decreases the pressure on the wing surface which is also one of the reason for the rise of C_t curve with respect to k_f as shown in Fig. 7.23.

7.4 Summary and conclusions

In this chapter, the aerodynamic performance of the biomimetic wing (wing modelling details are presented in the section 4.2.1) subjected to flapping motion is investigated at $Re = 5 \times 10^4$. The flapping motion of this study is defined as the combination of rotation about the axis (ξ(t)) along the wing's chord and the rotation about the axis (α(t)) along the semi span of the wing with a phase difference ((ϕ(t))). In order to systematically study the propulsive performance of the biomimetic wing performing flapping motion, the effect of mean angle of attack (θ_m), dimensionless flapping amplitude (α_f) and non dimensional flapping frequency (k_f) are investigated. Additionally, the flow field around the wing is also analysed to understand the viscous phenomenon of the fluid on the propulsive performance wing. It is observed that the proposed motion has a remarkable

influence on the flow structure and improves the propulsive performance of the wing under certain conditions.

At lower flapping amplitudes ($1^\circ \leq \alpha_f \leq 4^\circ$), there is not much improvement in the aerodynamic performance of the biomimetic wing undergoing flapping motion. When $\alpha_f \leq 5^\circ$, a large flow separation over the suction side of the wing is observed which affects the aerodynamic performance of the wing. Under the conditions when $\alpha_f \geq 5^\circ$ with $k_f \geq 3.5$, the Leading Edge Vortex (LEV) which was formed due to the flow separation contributes towards increase in the suction over the suction side of the wing. Due to this, the rise in mean thrust and propulsion efficiency is observed under these conditions. It is observed that, at $k_f \leq 3$, the formation and the convection of the LEV affects the thrust force generation of the wing. When $k_f \geq 5$ with $\theta_m = 0^\circ$, the adverse effects of the LEV are minimized due to the increase in the influence of the wing on the surrounding fluid. By analysing the flow field at different θ_m, it is observed that the wing generates positive thrust when $\theta_m \leq 4^\circ$. Further increase in θ_m encourages the alternating vortices to exhibit irregular patterns in the wake region. This eventually leads to the formation of cluster of vortices in the wake region (especially at $\theta_m = 16^\circ$) due to the increase in the interaction between the alternating vortices which gradually affects the aerodynamic performance of the wing. By maintaining $\theta_m \leq 8^\circ$ with $k_f \geq 3.5$, better aerodynamic performance is witnessed as the alternating vortices exhibiting thrust producing reverse Karman street.

भारतीय प्रौद्योगिकी संस्थान गुवाहाटी
Indian Institute of Technology Guwahati

Chapter 8

Concluding Remarks

8.1 Conclusions

A biomimetic wing is modelled using the Passer Domesticus wing planform as a reference. A thin and highly cambered airfoil, Bergey BW-3 airfoil is introduced at different sections of the planform to model the wing cross-section. In order to compare the aerodynamic performance of the biomimetic wing, the conventionally opted wing planforms namely rectangular and elliptical planforms are modelled with same dimensions and cross-section. The investigations reveals that the elliptical wing planform may be suitable for studies where the drag reduction is primary objective since the average drag coefficient of the elliptical wing is less than that of the other wings. On the other hand, the rectangular wing encourages the early flow separation due to the presence of the sharp edges in the wing planform. This led to a substantial increase in the drag coefficient and affects the overall lift to drag ratio (L/D) of the wing with respect to increase in the mean angle of attack. In the case of the biomimetic wing, the change in the shape along the span allows the wing to have a variable angle of attack with respect to the incoming flow. This encourages the flow to stay attached longer which delays the flow separation and improves the overall performance of the wing. This increases lift coefficient of the biomimetic wing by 57.9% compared to that of the elliptical wing and increases the L/D ratio by 22.4% compared to that of rectangular wing under same conditions.

The flow investigations when the biomimetic wing is subjected to pitching motion reveals that the unsteady vortex shedding over the pressure side of the wing is responsible for the negative suction. At lower pitch amplitudes (when $\alpha_p \leq 20^0$), this oppositely signed circulation can have significant impact on the positive suction which was created over the suction side of the wing and eventually affect the thrust force generation of the wing. Further, the investigations reveals that the increasing the reduced frequency

beyond 1.5 in combination with $\alpha_p \leq 20^0$ can reduce the vortex growth over pressure side and improves the wing's performance. The findings from the influence of mean angle of attack (θ_m) reveals that the separated flow is unable to reattach to the wing surface due to large flow separation when $\theta_m \geq 8^0$. Also shifting the pitch axis towards the trailing edge disrupts the vortex coherence and can adversely affect the instantaneous force coefficients of the wing.

Further investigations are carried out to analyse the unsteady flow characteristics of the biomimetic wing when subjected to plunging motion. The findings reveals that, a remarkable improvement in the instantaneous force coefficients can be achieved at smaller plunge amplitudes ($h_a \leq 0.1$) due to superior convection of the vortices along the vortex core. However, increasing the plunge amplitude increases the adverse interaction between the leading and trailing edge vortices and eventually affects the variation of force coefficients. The findings from the influence of the reduced frequency reveals that the increase in the frequency increases the vortex strength and encourages the vortex to form closer to the wing surface which eventually roll-up over the suction side of the wing. This remarkably influences the instantaneous force coefficients and improves the wing's performance.

Investigations are further carried out to analyse the aerodynamic performance of the biomimetic wing and associated flow structure when the wing is subjected to flapping motion. The flapping motion in the present study is defined as the combination of the rotations about wing chord and the span with a phase difference. By performing extensive parametric study, it is observed that there is an asymmetric variation in the instantaneous force coefficients dispite of having symmetrical flapping kinematics. This indicates that the optimal performance of the biomimetic wing can be achieved by proper selection of the operating parameters. At lower flapping amplitudes (when $\alpha_f \leq 5^0$), the wing doesn't have much influence over the surrounding fluid due to which the LEV forms farther away from the surface and won't have much contribution in providing extra suction. Therefore, by maintaining $\alpha_p \geq 5^0$ in combination with $k_f \geq 3.5$ not only increases the wing's influence over the surrounding fluid but also the LEV which was formed under these conditions contributes in thrust force generation. By analysing the influence of the mean angles of attack, different types of wake patterns are observed which affect the drag-thrust transition. The findings reveals that the increase in θ_m beyond 8^0 has detrimental effects on wing's performance as the wing is no longer in a position to overcome the drag offered by the surrounding fluid. It is observed that the alternating vortices form clusters when $\theta_m = 16^0$. This indicates that there is an adverse interference between the alternating vortices which can eventually stalls the wing's aerodynamic performance.

We hope the findings reported in this thesis might be helpful for practical implementation of innovative wing designs of MAVs to enhance their aerodynamic performance.

8.2 Future work

There are a number of possible ways, the work presented in this dissertation could be naturally extended:

- Fluid-structure interaction is one of the most important extension to this work. In the present study the wing is treated as a rigid body. However, a more realistic approach on the wing's performance can be explored by incorporating the flexible nature. This allows a local deformation with respect to the incoming flow and can lead to a wide variety of investigations.
- Although experimental investigations are extremely expensive but much needed for practical MAV wing design applications as there is scarce for the three dimensional investigations in the literature. Further analysis in this direction would be interesting.
- By considering the advancement in the artificial intelligence from the past few years, one such extension could be the development of tools using Artificial Neural Networks (ANNs) and Adaptive Neuro-Fuzzy Inference System (ANFIS). This can help in rapid prediction of the fluid forces when the wing is subjected to different unsteady conditions.
- Three dimensional numerical and experimental studies can be conducted by considering multi wing configuration as the works reported in this direction are very limited in the literature.
- One interesting extension could be training a neural network to achieve robustness in the wing motion where the wing can automatically change its kinematics with respect to the surrounding conditions. This can minimize the user interaction. Further investigations need to be carried out in that direction.

भारतीय प्रौद्योगिकी संस्थान गुवाहाटी
Indian Institute of Technology Guwahati

Publications

1. **Shaik, Masuruddin** and Hazarika, Shymanta Moni,"Numerical Investigation of Flow Over Oscillating ambered Foil At Low Reynolds Number", Journal of Fluids Engineering, ASME (https://doi.org/10.1115/1.4053556).

2. **Shaik, Masuruddin** and Hazarika, Shymanta Moni, "Aerodynamic Investigation of Passer Domesticus Inspired Biomimetic Wing at Low Reynolds number", Journal of Mechanical Engineering Science, SAGE (https://doi.org/10.1177/09544062221079509).

3. **Shaik, Masuruddin** and Hazarika, Shymanta Moni, "Unsteady Aerodynamics of Plunging Cambered Foil at Low Reynolds Number", Journal of Aerospace Engineering, SAGE (https://doi.org/10.1177/09544100221101724).

Under Review

1. **Shaik, Masuruddin** and Hazarika, Shymanta Moni, "Unsteady Aerodynamic Investigation of Passer Domesticus Inspired Biomimetic Wing Subjected to Flapping Motion", Journal of Mechanical Engineering Science, SAGE (Under review).

References

[1] A. Pelletier and T. J. Mueller, "Low reynolds number aerodynamics of low-aspect-ratio, thin/flat/cambered-plate wings," *Journal of Aircraft*, vol. 37, no. 5, pp. 825–832, 2000.

[2] D. F. Kurtulus, "Unsteady aerodynamics of a pitching naca 0012 airfoil at low reynolds number," *International Journal of Micro Air Vehicles*, vol. 11, p. 1756829319890609, 2019.

[3] R. Ramamurti and W. Sandberg, "Simulation of flow about flapping airfoils using finite element incompressible flow solver," *AIAA Journal*, vol. 39, no. 2, pp. 253–260, 2001.

[4] R. T. Jantzen, K. Taira, K. O. Granlund, and M. V. Ol, "Vortex dynamics around pitching plates," *Physics of Fluids*, vol. 26, no. 5, p. 053606, 2014.

[5] S. Heathcote, Z. Wang, and I. Gursul, "Effect of spanwise flexibility on flapping wing propulsion," *Journal of Fluids and Structures*, vol. 24, no. 2, pp. 183–199, 2008.

[6] M. Ashraf, J. Young, and J. Lai, "Reynolds number, thickness and camber effects on flapping airfoil propulsion," *Journal of Fluids and Structures*, vol. 27, no. 2, pp. 145–160, 2011.

[7] F. Siala and J. A. Liburdy, "Energy harvesting of a heaving and forward pitching wing with a passively actuated trailing edge," *Journal of Fluids and Structures*, vol. 57, pp. 1–14, 2015.

[8] W. R. Davis, B. B. Kosicki, D. M. Boroson, and D. Kostishack, "Micro air vehicles for optical surveillance," *Lincoln Laboratory Journal*, vol. 9, no. 2, pp. 197–214, 1996.

[9] W. Null and S. Shkarayev, "Effect of camber on the aerodynamics of adaptive-wing micro air vehicles," *Journal of Aircraft*, vol. 42, no. 6, pp. 1537–1542, 2005.

[10] T. Mueller and B. Jansen, JR, "Aerodynamic measurements at low reynolds numbers," *AIAA Journal*, pp. 82–598, 1982.

[11] M. Chopra, "Hydromechanics of lunate-tail swimming propulsion," *Journal of Fluid Mechanics*, vol. 64, no. 2, pp. 375–392, 1974.

[12] M. Chopra, "Lunate-tail swimming propulsion," in *Swimming and flying in nature*, pp. 635–650, Springer, 1975.

[13] C. P. Ellington, C. Van Den Berg, A. P. Willmott, and A. L. Thomas, "Leading-edge vortices in insect flight," *Nature*, vol. 384, no. 6610, pp. 626–630, 1996.

[14] H. Liu and K. Kawachi, "A numerical study of insect flight," *Journal of Computational Physics*, vol. 146, no. 1, pp. 124–156, 1998.

[15] M. H. Dickinson, F.-O. Lehmann, and S. P. Sane, "Wing rotation and the aerodynamic basis of insect flight," *Science*, vol. 284, no. 5422, pp. 1954–1960, 1999.

[16] M. Dickinson, "Solving the mystery of insect flight," *Scientific American*, vol. 284, no. 6, pp. 48–57, 2001.

[17] T. Weis-Fogh, "Flapping flight and power in birds and insects, conventional and novel mechanisms," in *Swimming and Flying in Nature*, pp. 729–762, Springer, 1975.

[18] T. J. Mueller and J. D. DeLaurier, "Aerodynamics of small vehicles," *Annual Review of Fluid Mechanics*, vol. 35, no. 1, pp. 89–111, 2003.

[19] J. Katz and A. Plotkin, *Low-speed aerodynamics*, vol. 13. Cambridge University Press, 2001.

[20] J. Katz and D. Weihs, "Behavior of vortex wakes from oscillating airfoils," *Journal of Aircraft*, vol. 15, no. 12, pp. 861–863, 1978.

[21] F. Archibald, "Unsteady kutta condition at high values of the reduced frequency parameter," *Journal of Aircraft*, vol. 12, no. 6, pp. 545–550, 1975.

[22] Z. J. Wang, "Vortex shedding and frequency selection in flapping flight," *Journal of Fluid Mechanics*, vol. 410, pp. 323–341, 2000.

[23] R. Krasny, "Computation of vortex sheet roll-up in the trefftz plane," *Journal of Fluid Mechanics*, vol. 184, pp. 123–155, 1987.

[24] T. Kármán and J. Burgers, *General aerodynamic theory: perfect fluids*. Springer, 1935.

[25] T. Theodorsen, "General theory of aerodynamic instability and the mechanism of flutter," *National Aeronautics and Space Administration: Washington, DC, USA*, pp. 291–311, 1979.

[26] I. Garrick *et al.*, "Propulsion of a flapping and oscillating airfoil," *NACA report*, vol. 567, pp. 419–427, 1937.

[27] R. Katzmayr, "Effect of periodic changes of angle of attack on behavior of airfoils," NACA Tech. Report-214, 1922.

[28] M. M. Koochesfahani, "Vortical patterns in the wake of an oscillating airfoil," *AIAA Journal*, vol. 27, no. 9, pp. 1200–1205, 1989.

[29] C. Dohring, M. Platzer, K. Jones, and I. Tuncer, "Computational and experimental investigation of the wakes shed from flapping airfoils and their wake interference/impingement characteristics," in *Agard Conference Proceedings Agard Cp*, pp. 33–33, 1996.

[30] P. Freymuth, "Propulsive vortical signature of plunging and pitching airfoils," *AIAA Journal*, vol. 26, no. 7, pp. 881–883, 1988.

[31] K. Jones, C. Dohring, and M. Platzer, "Experimental and computational investigation of the knoller-betz effect," *AIAA Journal*, vol. 36, no. 7, pp. 1240–1246, 1998.

[32] J. Lai and M. Platzer, "Jet characteristics of a plunging airfoil," *AIAA Journal*, vol. 37, no. 12, pp. 1529–1537, 1999.

[33] Z. J. Wang, "Dissecting insect flight," *Annu. Rev. Fluid Mech.*, vol. 37, pp. 183–210, 2005.

[34] M. H. Dickinson and K. G. Gotz, "Unsteady aerodynamic performance of model wings at low reynolds numbers," *Journal of Experimental Biology*, vol. 174, no. 1, pp. 45–64, 1993.

[35] G. J. Leishman, *Principles of helicopter aerodynamics with CD extra*. Cambridge University Press, 2006.

[36] W. J. McCroskey, "The phenomenon of dynamic stall.," tech. rep., National Aeronuatics and Space Administration Moffett Field Ca Ames Research, 1981.

[37] C. P. Ellington, "The aerodynamics of hovering insect flight. i. the quasi-steady analysis," *Philosophical Transactions of the Royal Society of London. B, Biological Sciences*, vol. 305, no. 1122, pp. 1–15, 1984.

[38] C. P. Ellington, "The novel aerodynamics of insect flight: applications to micro-air vehicles," *Journal of Experimental Biology*, vol. 202, no. 23, pp. 3439–3448, 1999.

[39] S. P. Sane and M. H. Dickinson, "The aerodynamic effects of wing rotation and a revised quasi-steady model of flapping flight," *Journal of Experimental Biology*, vol. 205, no. 8, pp. 1087–1096, 2002.

[40] T. Weis-Fogh, "Quick estimates of flight fitness in hovering animals, including novel mechanisms for lift production," *Journal of Experimental Biology*, vol. 59, no. 1, pp. 169–230, 1973.

[41] F.-O. Lehmann and M. H. Dickinson, "The control of wing kinematics and flight forces in fruit flies (drosophila spp.).," *Journal of Experimental Biology*, vol. 201, no. 3, pp. 385–401, 1998.

[42] M. S. Vest and J. Katz, "Unsteady aerodynamic model of flapping wings," *AIAA Journal*, vol. 34, no. 7, pp. 1435–1440, 1996.

[43] M. J. Smith, "Simulating moth wing aerodynamics-towards the development of flapping-wing technology," *AIAA Journal*, vol. 34, no. 7, pp. 1348–1355, 1996.

[44] T. H. von Karman and W. R. Sears, "Airfoil theory for non-uniform motion," *Journal of the Aeronautical Sciences*, vol. 5, no. 10, pp. 379–390, 1938.

[45] J. G. Leishman, "Challenges in modelling the unsteady aerodynamics of wind turbines," *Wind Energy: An International Journal for Progress and Applications in Wind Power Conversion Technology*, vol. 5, no. 2-3, pp. 85–132, 2002.

[46] I. Garrick *et al.*, "Propulsion of a flapping and oscillating airfoil," *Report National Advisory Committee for Aeronautics, NACA Report*, no. 567, pp. 419–427, 1936.

[47] I. E. Garrick, "On some reciprocal relations in the theory of nonstationary flows," US Government Printing Office, 1938.

[48] Y. Jung and S. O. Park, "Vortex-shedding characteristics in the wake of an oscillating airfoil at low reynolds number," *Journal of Fluids and Structures*, vol. 20, no. 3, pp. 451–464, 2005.

[49] M. Fuchiwaki, K. Tanaka, H. Tanaka, K. Kamemoto, and O. Baysal, "Flow patterns behind pitching airfoil and unsteady fluid forces," *ASME, FEDSM99-7286*, 1999.

[50] M. Fuchiwaki and K. Tanaka, "Vortex structure and scale on an unsteady airfoil," *JSME International Journal Series B Fluids and Thermal Engineering*, vol. 49, no. 4, pp. 1056–1063, 2006.

[51] S. Ōtomo, S. Henne, K. Mulleners, K. Ramesh, and I. M. Viola, "Unsteady lift on a high-amplitude pitching aerofoil," *Experiments in Fluids*, vol. 62, no. 1, pp. 1–18, 2021.

[52] C. Shih, L. Lourenco, and A. Krothapalli, "Investigation of flow at leading and trailing edges of pitching-up airfoil," *AIAA Journal*, vol. 33, no. 8, pp. 1369–1376, 1995.

[53] A.-J. Buchner, N. Buchmann, K. Kilany, C. Atkinson, and J. Soria, "Stereoscopic and tomographic piv of a pitching plate," *Experiments in Fluids*, vol. 52, no. 2, pp. 299–314, 2012.

[54] A.-J. Buchner, D. Honnery, and J. Soria, "Stability and three-dimensional evolution of a transitional dynamic stall vortex," *Journal of Fluid Mechanics*, vol. 823, pp. 166–197, 2017.

[55] A. Widmann and C. Tropea, "Reynolds number influence on the formation of vortical structures on a pitching flat plate," *Interface Focus*, vol. 7, no. 1, p. 20160079, 2017.

[56] H.-T. Yu and L. P. Bernal, "Effects of pivot location and reduced pitch rate on pitching rectangular flat plates," *AIAA Journal*, vol. 55, no. 3, pp. 702–718, 2017.

[57] A. Mackowski and C. Williamson, "Direct measurement of thrust and efficiency of an airfoil undergoing pure pitching," *Journal of Fluid Mechanics*, vol. 765, pp. 524–543, 2015.

[58] R. E. D. Bishop and A. Hassan, "The lift and drag forces on a circular cylinder oscillating in a flowing fluid," *Proceedings of the Royal Society of London. Series A. Mathematical and Physical Sciences*, vol. 277, no. 1368, pp. 51–75, 1964.

[59] C. H. Williamson and A. Roshko, "Vortex formation in the wake of an oscillating cylinder," *Journal of Fluids and Structures*, vol. 2, no. 4, pp. 355–381, 1988.

[60] K. M. Lam, J. Hu, and P. Liu, "Vortex formation processes from an oscillating circular cylinder at high keulegan–carpenter numbers," *Physics of Fluids*, vol. 22, no. 1, p. 015105, 2010.

[61] A. Techet, F. Hover, and M. Triantafyllou, "Vortical patterns behind a tapered cylinder oscillating transversely to a uniform flow," *Journal of Fluid Mechanics*, vol. 363, pp. 79–96, 1998.

[62] K. B. Lua, T. Lim, K. Yeo, and G. Oo, "Wake-structure formation of a heaving two-dimensional elliptic airfoil," *AIAA Journal*, vol. 45, no. 7, pp. 1571–1583, 2007.

[63] S. Heathcote and I. Gursul, "Jet switching phenomenon for a periodically plunging airfoil," *Physics of Fluids*, vol. 19, no. 2, p. 027104, 2007.

[64] S.-H. Chen and C.-M. Ho, "Near wake of an unsteady symmetric airfoil," *Journal of Fluids and Structures*, vol. 1, no. 2, pp. 151–164, 1987.

[65] M. Triantafyllou, G. Triantafyllou, and R. Gopalkrishnan, "Wake mechanics for thrust generation in oscillating foils," *Physics of Fluids A: Fluid Dynamics*, vol. 3, no. 12, pp. 2835–2837, 1991.

[66] P. Freymuth, "Thrust generation by an airfoil in hover modes," *Experiments in Fluids*, vol. 9, no. 1, pp. 17–24, 1990.

[67] H. Nagai, K. Isogai, T. Fujimoto, and T. Hayase, "Experimental and numerical study of forward flight aerodynamics of insect flapping wing," *AIAA Journal*, vol. 47, no. 3, pp. 730–742, 2009.

[68] Z. J. Wang, J. M. Birch, and M. H. Dickinson, "Unsteady forces and flows in low reynolds number hovering flight: two-dimensional computations vs robotic wing experiments," *Journal of Experimental Biology*, vol. 207, no. 3, pp. 449–460, 2004.

[69] B. Singh and I. Chopra, "Insect-based hover-capable flapping wings for micro air vehicles: experiments and analysis," *AIAA Journal*, vol. 46, no. 9, pp. 2115–2135, 2008.

[70] A. Jameson, "Time dependent calculations using multigrid, with applications to unsteady flows past airfoils and wings," in *10th Computational Fluid Dynamics Conference*, p. 1596, 1991.

[71] S. Yang, S. Luo, F. Liu, and H.-M. Tsai, "Subsonic flow over unstalled pitching airfoil computed by euler method," in *36th AIAA Fluid Dynamics Conference and Exhibit*, p. 3914, 2006.

[72] M. Akbari and S. Price, "Simulation of dynamic stall for a naca 0012 airfoil using a vortex method," *Journal of Fluids and Structures*, vol. 17, no. 6, pp. 855–874, 2003.

[73] N. Okong'o and D. D. Knight, "Implicit unstructured navier-stokes simulation of leading edge separation over a pitching airfoil," *Applied Numerical Mathematics*, vol. 27, no. 3, pp. 269–308, 1998.

[74] H. Hamdani and M. Sun, "Aerodynamic forces and flow structures of an airfoil in some unsteady motions at small reynolds number," *Acta Mechanica*, vol. 145, no. 1, pp. 173–187, 2000.

[75] M. R. Visbal and J. Shang, "Investigation of the flow structure around a rapidly pitching airfoil," *AIAA Journal*, vol. 27, no. 8, pp. 1044–1051, 1989.

[76] J. S. Leontini, B. E. Stewart, M. C. Thompson, and K. Hourigan, "Wake state and energy transitions of an oscillating cylinder at low reynolds number," *Physics of Fluids*, vol. 18, no. 6, p. 067101, 2006.

[77] O. A. Marzouk, "Direct numerical simulations of the flow past a cylinder moving with sinusoidal and nonsinusoidal profiles," *Journal of Fluids Engineering*, vol. 131, no. 12, 2009.

[78] X. Yang and Z. C. Zheng, "Nonlinear spacing and frequency effects of an oscillating cylinder in the wake of a stationary cylinder," *Physics of Fluids*, vol. 22, no. 4, p. 043601, 2010.

[79] J.-Y. Andro and L. Jacquin, "Frequency effects on the aerodynamic mechanisms of a heaving airfoil in a forward flight configuration," *Aerospace Science and Technology*, vol. 13, no. 1, pp. 71–80, 2009.

[80] S. An, J. Maeng, and C. Han, "Thickness effect on the thrust generation of heaving elliptic airfoils," *Journal of Aircraft*, vol. 46, no. 1, pp. 216–222, 2009.

[81] M. Amiralaei, H. Alighanbari, and M. Hashemi, "Unsteady cfd of a plunging airfoil in low-reynolds-number flow regime," in *40th Fluid Dynamics Conference and Exhibit*, p. 4460, 2010.

[82] G. C. Lewin and H. Haj-Hariri, "Modelling thrust generation of a two-dimensional heaving airfoil in a viscous flow," *Journal of Fluid Mechanics*, vol. 492, pp. 339–362, 2003.

[83] J. Young and J. C. Lai, "Oscillation frequency and amplitude effects on the wake of a plunging airfoil," *AIAA Journal*, vol. 42, no. 10, pp. 2042–2052, 2004.

[84] J.-S. Lee, C. Kim, and K. H. Kim, "Design of flapping airfoil for optimal aerodynamic performance in low-reynolds number flows," *AIAA Journal*, vol. 44, no. 9, pp. 1960–1972, 2006.

[85] R. Mittal, Y. Utturkar, and H. Udaykumar, "Computational modeling and analysis of biomimetic flight mechanisms," in *40th AIAA Aerospace Sciences Meeting & Exhibit*, p. 865, 2002.

[86] J. Tang, D. Viieru, and W. Shyy, "Effects of reynolds number and flapping kinematics on hovering aerodynamics," *AIAA Journal*, vol. 46, no. 4, pp. 967–976, 2008.

[87] F. M. Bos, D. Lentink, B. Van Oudheusden, and H. Bijl, "Influence of wing kinematics on aerodynamic performance in hovering insect flight," *Journal of Fluid Mechanics*, vol. 594, pp. 341–368, 2008.

[88] M. Kaya and I. H. Tuncer, "Nonsinusoidal path optimization of a flapping airfoil," *AIAA Journal*, vol. 45, no. 8, pp. 2075–2082, 2007.

[89] M. Sun and J. Tang, "Lift and power requirements of hovering flight in drosophila virilis," *Journal of Experimental Biology*, vol. 205, no. 16, pp. 2413–2427, 2002.

[90] J. Young, J. C. Lai, and C. Germain, "Simulation and parameter variation of flapping-wing motion based on dragonfly hovering," *AIAA Journal*, vol. 46, no. 4, pp. 918–924, 2008.

[91] C. Li and H. Dong, "Wake structure and aerodynamic performance of low aspect-ratio revolving plates at low reynolds number," *AIAA Paper*, vol. 1453, p. 2014, 2014.

[92] R. Ramamurti and W. C. Sandberg, "A three-dimensional computational study of the aerodynamic mechanisms of insect flight," *Journal of Experimental Biology*, vol. 205, no. 10, pp. 1507–1518, 2002.

[93] R. Ramamurti and W. Sandberg, "Computations of insect and fish locomotion with applications to unconventional unmanned vehicles," *AIAA Journal*, vol. 46, no. 9, pp. 2178–2190, 2008.

[94] P. Wesseling, *Principles of computational fluid dynamics*, vol. 29. Springer Science & Business Media, 2009.

[95] O. Reynolds, "Xxix. an experimental investigation of the circumstances which determine whether the motion of water shall be direct or sinuous, and of the law of resistance in parallel channels," *Philosophical Transactions of the Royal society of London*, no. 174, pp. 935–982, 1883.

[96] P. Moin and K. Mahesh, "Direct numerical simulation: a tool in turbulence research," *Annual Review of Fluid Mechanics*, vol. 30, no. 1, pp. 539–578, 1998.

[97] U. Piomelli, "Large-eddy and direct simulation of turbulent flows," *Lecture series-van Kareman Institute for fluid dynamics*, vol. 4, pp. G1–G70, 2000.

[98] F. Menter, "Zonal two equation kw turbulence models for aerodynamic flows," in *23rd Fluid Dynamics, Plasmadynamics, and Lasers Conference*, p. 2906, 1993.

[99] F. R. Menter, "Two-equation eddy-viscosity turbulence models for engineering applications," *AIAA Journal*, vol. 32, no. 8, pp. 1598–1605, 1994.

[100] Wilcox and D. C, *Turbulence modeling for CFD*, vol. 2. DCW industries La Canada, CA, 1998.

[101] F. R. Menter, M. Kuntz, and R. Langtry, "Ten years of industrial experience with the sst turbulence model," *Turbulence, Heat and Mass Transfer*, vol. 4, no. 1, pp. 625–632, 2003.

[102] D. Johnson and L. King, "A new turbulence closure model for boundary layer flows with strong adverse pressure gradients and separation," in *22nd Aerospace Sciences Meeting*, p. 175, 1984.

[103] G. Kalitzin, G. Medic, G. Iaccarino, and P. Durbin, "Near-wall behavior of rans turbulence models and implications for wall functions," *Journal of Computational Physics*, vol. 204, no. 1, pp. 265–291, 2005.

[104] A. FLUENT, "Solver theory guide, release 14.0: Ansys," 2011.

[105] A. Fluent, "Fluent 14.0 user's guide," *ANSYS FLUENT Inc*, 2011.

[106] M. S. Selig, *Summary of low speed airfoil data*. SOARTECH publications, Virginia, USA, 1995.

[107] E. Gabriel and T. Mueller, "low-aspect-ratio wing aerodynamics at low reynolds number," *AIAA Journal*, vol. 42, no. 5, pp. 865–873, 2004.

[108] E. Laitone, "Aerodynamic lift at reynolds numbers below 7 x 10 exp 4," *AIAA Journal*, vol. 34, no. 9, pp. 1941–1942, 1996.

[109] S. M. Kaplan, A. Altman, and M. Ol, "Wake vorticity measurements for low aspect ratio wings at low reynolds number," *Journal of Aircraft*, vol. 44, no. 1, pp. 241–251, 2007.

[110] M. Okamoto and A. Azuma, "Aerodynamic characteristics at low reynolds number for wings of various planforms," *AIAA Journal*, vol. 49, no. 6, pp. 1135–1150, 2011.

[111] D. Bilo, "Biophysics of flight of small birds. 1. kinematics and aerodynamics of downstroke of house sparrow (passer-domesticus l)," *Journal of Comparative Physiology*, vol. 71, no. 4, p. 382, 1971.

[112] D. BILO, "Biophysics of flight of small birds. 2. kinematics and aerodynamics of upstroke of house sparrow (passer-domesticus l)," *Journal of Comparative Physiology*, vol. 76, no. 4, p. 426, 1972.

[113] W. Nachtigall, "Comparative studies on function of bastard wing (alula spuria) in flight biology birds. 1. alula as a producer of high lift," *Journal of Comparative Physiology*, vol. 71, no. 3, pp. 326–+, 1971.

[114] H. Rahmani, M. Biglari, M. S. Valipour, and K. Lari, "Numerical investigation of the effects of immersion on the efficiency of a tidal helical turbine," *Proceedings of the Institution of Mechanical Engineers, Part C: Journal of Mechanical Engineering Science*, vol. 233, no. 12, pp. 4299–4310, 2019.

[115] Y. Cheng, X. Wang, W. Ur Rehman, T. Sun, H. Shahzad, and H. Chai, "Numerical simulation and experimental performance research of cylindrical vane pump," *Proceedings of the Institution of Mechanical Engineers, Part C: Journal of Mechanical Engineering Science*, p. 09544062211020037, 2021.

[116] A. Roy, R. Vinoth Kumar, and R. Mukherjee, "Experimental validation of numerical decambering approach for flow past a rectangular wing," *Proceedings of the Institution of Mechanical Engineers, Part G: Journal of Aerospace Engineering*, vol. 234, no. 9, pp. 1564–1582, 2020.

[117] A. Roy and R. Mukherjee, "Three dimensional rectangular wing morphed to prevent stall and operate at design local two dimensional lift coefficient," *Aerospace Science and Technology*, vol. 107, p. 106312, 2020.

[118] R. J. Moffat, "Describing the uncertainties in experimental results," *Experimental Thermal and Fluid Science*, vol. 1, no. 1, pp. 3–17, 1988.

[119] R. C. Pankhurst and D. W. Holder, *Wind-tunnel technique: an account of experimental methods in low-and high-speed wind tunnels*. Pitman, 1952.

[120] J. B. Barlow, W. H. Rae, and A. Pope, *Low-speed wind tunnel testing*. John wiley & sons, 1999.

[121] A. Aboelezz, Y. Elqudsi, M. Hassanalian, and A. Desoki, "Wind tunnel calibration, corrections and experimental validation for fixed-wing micro air vehicles measurements," *Aviation*, vol. 23, no. 4, pp. 104–113, 2019.

[122] U. Cella, P. Della Vecchia, C. Groth, S. Porziani, A. Chiappa, F. Giorgetti, F. Nicolosi, and M. E. Biancolini, "Wind tunnel model design and aeroelastic measurements of the ribes wing," *Journal of Aerospace Engineering*, vol. 34, no. 1, p. 04020109, 2021.

[123] W. G. Bastedo Jr and T. J. Mueller, "Spanwise variation of laminar separation bubbles on wings at low reynolds number," *Journal of Aircraft*, vol. 23, no. 9, pp. 687–694, 1986.

[124] M. Picard-Deland, M. Olivier, G. Dumas, and T. Kinsey, "Oscillating-foil turbine operating at large heaving amplitudes," *AIAA Journal*, vol. 57, no. 12, pp. 5104–5113, 2019.

[125] K. Taira and T. Colonius, "Three-dimensional flows around low-aspect-ratio flat-plate wings at low reynolds numbers," *Journal of Fluid Mechanics*, vol. 623, pp. 187–207, 2009.

[126] K. Granlund, M. Ol, K. Taira, and R. Jantzen, "Parameter studies on rotational and translational accelerations of flat plates," tech. rep., Air Force Research Lab Wright-Patterson AFB OH Aerospace Systems Dir, 2013.

[127] R. Jantzen, K. Taira, K. Granlund, and M. Ol, "On the influence of pitching and acceleration on vortex dynamics around low-aspect-ratio rectangular wing," in *51st AIAA Aerospace Sciences Meeting Including the New Horizons Forum and Aerospace Exposition*, p. 833, 2013.

[128] P. Wernert, W. Geissler, M. Raffel, and J. Kompenhans, "Experimental and numerical investigations of dynamic stall on a pitching airfoil," *AIAA Journal*, vol. 34, no. 5, pp. 982–989, 1996.

[129] A. Spentzos, G. Barakos, K. Badcock, B. Richards, P. Wernert, S. Schreck, and M. Raffel, "Investigation of three-dimensional dynamic stall using computational fluid dynamics," *AIAA Journal*, vol. 43, no. 5, pp. 1023–1033, 2005.

[130] S. Wang, D. B. Ingham, L. Ma, M. Pourkashanian, and Z. Tao, "Numerical investigations on dynamic stall of low reynolds number flow around oscillating airfoils," *Computers & Fluids*, vol. 39, no. 9, pp. 1529–1541, 2010.

[131] X. Li, D. Grecov, Z. Guo, and Z. Hou, "Influence of unsteady and kinematic parameters on aerodynamic characteristics of a pitching airfoil," *Journal of Aerospace Engineering*, vol. 32, no. 1, p. 04018120, 2019.

[132] N. Chiereghin, D. Cleaver, and I. Gursul, "Unsteady lift and moment of a periodically plunging airfoil," *AIAA Journal*, vol. 57, no. 1, pp. 208–222, 2019.

[133] D. J. Cleaver, Z. Wang, I. Gursul, and M. Visbal, "Lift enhancement by means of small-amplitude airfoil oscillations at low reynolds numbers," *AIAA Journal*, vol. 49, no. 9, pp. 2018–2033, 2011.

[134] J. Young and J. C. Lai, "Vortex lock-in phenomenon in the wake of a plunging airfoil," *AIAA Journal*, vol. 45, no. 2, pp. 485–490, 2007.

[135] M. R. Visbal, "High-fidelity simulation of transitional flows past a plunging airfoil," *AIAA Journal*, vol. 47, no. 11, pp. 2685–2697, 2009.

[136] D. Cleaver, Z. Wang, and I. Gursul, "Investigation of high-lift mechanisms for a flat-plate airfoil undergoing small-amplitude plunging oscillations," *AIAA Journal*, vol. 51, no. 4, pp. 968–980, 2013.

[137] M. S. U. Khalid, I. Akhtar, and N. I. Durrani, "Analysis of strouhal number based equivalence of pitching and plunging airfoils and wake deflection," *Proceedings of the Institution of Mechanical Engineers, Part G: Journal of Aerospace Engineering*, vol. 229, no. 8, pp. 1423–1434, 2015.

[138] M. E. Abd El-Latief, K. Elsayed, and M. Madbouli Abdelrahman, "Aerodynamic study of the corrugated airfoil at ultra-low reynolds number," *Advances in Mechanical Engineering*, vol. 11, no. 10, p. 1687814019884164, 2019.

[139] J. Mohrfeld Halterman and M. Uddin, "Systematic reduced order model development of a pitching naca0012 airfoil," *Proceedings of the Institution of Mechanical Engineers, Part G: Journal of Aerospace Engineering*, vol. 235, no. 4, pp. 427–438, 2021.

[140] D. Calderon, Z. Wang, and I. Gursul, "Effect of wing geometry on the lift of a plunging finite wing," in *40th Fluid Dynamics Conference and Exhibit*, p. 4459, 2010.

[141] D. Calderon, Z. Wang, and I. Gursul, "Lift enhancement of a rectangular wing undergoing a small amplitude plunging motion," in *48th AIAA Aerospace Sciences Meeting Including The New Horizons Forum and Aerospace Exposition*, p. 386, 2010.

[142] A. Gross, M. Agate, J. Little, and H. F. Fasel, "Numerical simulation of plunging wing section at high angles of attack," *AIAA Journal*, vol. 56, no. 7, pp. 2514–2527, 2018.

[143] M. F. Platzer, K. D. Jones, J. Young, and J. C. Lai, "Flapping wing aerodynamics: progress and challenges," *AIAA journal*, vol. 46, no. 9, pp. 2136–2149, 2008.

[144] G. Srikumar, V. A. Srikrishnan, R. K. Purushothaman, V. Thiagarajan, R. K. Velamati, and V. Laxman, "Numerical study on thrust generation in an airfoil undergoing nonsinusoidal plunging motion," *Journal of Aerospace Engineering*, vol. 31, no. 4, p. 04018037, 2018.

[145] S. K. Ghosh, C. L. Dora, and D. Das, "Unsteady wake characteristics of a flapping wing through 3d tr-piv," *Journal of Aerospace Engineering*, vol. 25, no. 4, pp. 547–558, 2012.

[146] Y. T. Lee, K. Ramesh, and A. Gopalarathnam, "Study of edge suction in airfoils with round trailing edges in unsteady flow," in *AIAA Aviation 2021 Forum*, p. 2617, 2021.

[147] Y. T. Lee, K. K. Ramesh, and A. Gopalarathnam, "Low-order modeling of unsteady flow around airfoils with rounded trailing edges," in *AIAA Scitech 2022 Forum*, p. 1668, 2022.

[148] H. J. Bird, K. K. Ramesh, S. Otomo, and I. M. Viola, "Leading edge vortex formation on finite wings using vortex particles," in *AIAA Scitech 2021 Forum*, p. 1196, 2021.

[149] H. J. Bird and K. Ramesh, "Unsteady lifting-line theory and the influence of wake vorticity on aerodynamic loads," *Theoretical and Computational Fluid Dynamics*, vol. 35, no. 5, pp. 609–631, 2021.

[150] F. Hover, Ø. Haugsdal, and M. Triantafyllou, "Effect of angle of attack profiles in flapping foil propulsion," *Journal of Fluids and Structures*, vol. 19, no. 1, pp. 37–47, 2004.

[151] S. Dash, K.-B. Lua, T. Lim, and K. Yeo, "Enhanced thrust performance of a two dimensional elliptic airfoil at high flapping frequency in a forward flight," *Journal of Fluids and Structures*, vol. 76, pp. 37–59, 2018.

[152] H. R. Karbasian and J. Esfahani, "Enhancement of propulsive performance of flapping foil by fish-like motion pattern," *Computers & Fluids*, vol. 156, pp. 305–316, 2017.